INCREMENTAL EQUAL CHANNEL ANGULAR PRESSING AT ELEVATED TEMPERATURES OF AL 5083 AND FOLLOW-UP BACKWARD MICRO-EXTRUSION OF COMPONENTS

MOHD NIZAM BIN KATIMON

This thesis is submitted in partial
fulfilment of the requirement for the award of the
Doctor of Philosophy

Department of Design, Manufacturing
and Engineering Management
Faculty of Engineering
University of Strathclyde

NOVEMBER 2025

‘This thesis is the result of the author’s original research. It has been composed by the author and has not been previously submitted for examination which has led to the award of a degree.’

Signed	:	Mohd Nizam Bin Katimon
Date	:	24 November 2025

First Supervisor	:	Professor Yi Qin
Second Supervisor	:	Dr. Wenkun Xie
Main Supervisor	:	Dr. Andrzej Rosochowski

‘In the name of Allah, the Most Gracious, the Most Merciful’

ACKNOWLEDGEMENT

Alhamdulillah, all praise be to Allah, the Lord of the Universe and the Master of the Day of Judgement, for His divine guidance throughout this remarkable journey.

First, I would like to extend my deepest gratitude to my main supervisor, Dr. Andrzej Rosochowski, for all his support, encouragement, and guidance. I am also sincerely thankful to my first supervisor, Professor Yi Qin, and my second supervisor, Dr. Wenkun Xie, for their assistance in ensuring the successful completion of my work, particularly related to the VIVA process.

Second, thanks to my PhD colleagues Dr. Muhammad Jawad Qarni, Dr. Michal Gzyl, Dr. Mohammad Reza Salamati, and Bo Chen for sharing knowledge and helping throughout this journey. I also wish to express my sincere appreciation to the staff at the Design, Manufacturing, and Engineering Management (Barrie Hunter, Duncan Lindsay, Stephen Ross) and the Advanced Forming Research Centre (Helge Jorgensen, Duncan Roger, Lisa Hall, Ryan O'Neill, Kornelia Kondziolka) for their assistance. Also, to James Gillespie (Mechanical and Aerospace Engineering) for his help in conducting the mechanical tests. Then, to Dr. Sonia Boczkal (Institute of Non-Ferrous Metals in Skawina, Poland) for her expert guidance and assistance with the microstructure studies. Prof. Lech Olejnik (Warsaw University of Technology, Poland) for providing the Al 5083 materials and conducting the conversion coating of Al 5083. Not to forget Dr. Muhammad Azfar Noordin for sharing knowledge and advice with the Abaqus simulation study.

Lastly, I would like to thank my beloved family - Haji Katimon Samin, Hajah Siti Ahasah Haji A. Kadir, Hajah Attanah Mohd Salleh, Rosnah Mohd Zin, Nurul Husna, Akmal Izham, Irfan Wafiq, siblings, and friends - for their prayers and continued support in the completion of this journey.

ABSTRACT

The demand for micro products has been continuously increasing over the years. Many industries, including telecommunications, automotive, and medical fields, need small and precise micro parts. However, the main challenge lies in manufacturing these microparts using the most suitable process. One promising option is backward micro-extrusion, which is characterised by low material consumption, low force requirements, and high production rates compared to forward micro-extrusion. Nevertheless, the formability and surface finish of the micro parts depend greatly on the condition of the material and the process parameters.

This study focuses on producing miniature conical pins, and two important research questions arise. The first concerns which types of materials produce better final conditions of microparts, while the second examines the effects of processing backward micro-extrusion at elevated temperatures on product quality. The answers to these questions involve addressing the key challenges, determining the suitable material condition, which is ultrafine-grained (UFG) materials, and identifying the optimal process temperature in microforming.

The Incremental Equal Channel Angular Pressing (I-ECAP) method was used to produce UFG Al 5083 material. It was processed at 200 °C using route B_C and a die with a 90° channel angle, using the as-received Al 5083. For backward micro-extrusion, the process parameters included temperatures (RT, 200 °C, and 250 °C), a punch displacement of 1.0 mm, and a process time of 200 s.

UFG structures were successfully produced with average grain sizes of 0.49 μm and 0.45 μm after four and eight passes of I-ECAP, respectively. The compression yield strength of UFG Al 5083 was reduced by about three times as the testing temperature increased from 200 °C to 250 °C. Consequently, the height of the conical pins achieved ranged from 80% to 100% of the cavity height for all specimens at 250 °C. The average height of conical pins at 250 °C was around 1.5 times higher compared to those at 200 °C. The results confirmed that backward micro-extrusion at elevated

temperatures using UFG materials produced better filling, improved surface finish, and a lower extrusion load compared to coarse-grained materials.

This study contributes new knowledge on the relationship between grain size and temperature in relation to the microforming behaviour of Al 5083. The combination of I-ECAP and backward micro-extrusion presents a novel approach to producing high-quality microparts.

TABLE OF CONTENTS

LIST OF TABLES

LIST OF FIGURES

CHAPTER 1
INTRODUCTION

1.1 Research Motivation

Micromanufacturing refers to the process of producing very small products in the micrometer range (Masuzawa, 2000). The size of micro manufactured products is defined as not exceeding the sub-millimeter range (Geiger et al., 2001). The most critical challenge in micromanufacturing is the process of converting materials to useful products, which is a complex task (Engel & Eckstein, 2002).

Microforming is one of several micromanufacturing processes, and there are several challenges that need to be addressed to achieve a successful process. These challenges are controlling the material microstructure, selecting appropriate process parameters, ensuring tool accuracy and surface quality, maintaining machine stiffness and precision, and consider size effect and friction behaviour. A combination of optimal material condition and process parameters is essential to overcome these challenges. The grain size of microstructure is crucial in determining of forming behaviour. While, conventional macroforming knowledge cannot be directly applied to microforming due to differences in tool accuracy, machine stiffness, and the punch force-displacement characteristics (Razali & Qin, 2013). Studies by Engel and Eckstein (2002) and Vollertsen et al. (2006) proved the existence of the size effect, resulting from the size of micro component becoming comparable to the grain size of the material. This effect often leads to reduced yield stress and increased friction during microforming. The friction factor increases as the specimen size decreases (Raja & Ramesh, 2021), and it also significantly affects the flow stress and deformation behaviour of materials (Xu et al., 2021).

One example of a microformed component is the miniature conical pin, inspired by microneedle arrays used for transdermal drug delivery. Typically, microneedles have a conical shape with sharp tips and lengths ranging from 0.15 mm to 0.77 mm (Henry et al., 1998). Shaping these geometries is hard because of friction, so the material must flow well. The material also needs to be strong and flexible enough to be inserted properly.

Ultrafine-grained (UFG) materials provide an option to overcome issues such as size effect and product quality. Ultrafine-grained (UFG) materials can make microformed products more uniform and give a better surface finish (Rosochowski et al., 2007; Presz & Rosochowski, 2006). Microforming UFG metals can be done at room temperature (RT) or at higher temperatures. Using higher temperatures helps control size effects, makes the material flow more easily, and reduces the force needed to form it, as seen in superplastic forming and hot embossing processes (Eichenhueller et al., 2007; Comley, 2004; Xu et al., 2015).

UFG materials can be produced using any of the severe plastic deformation (SPD) processes (Edalati et al., 2022; Valiev et al., 2022). Equal channel angular pressing (ECAP) is one of the most widely used techniques among SPD methods (Azushima et al., 2008). Conventional ECAP faces problems such as high force requirements, uneven deformation, and low production rate, making it difficult for industrial applications (Valiev et al., 2022; Edalati et al., 2022). Rosochowski and Olejnik (2007a) introduced the Incremental Equal Channel Angular Pressing (I-ECAP), a new concept based on ECAP, that can process long billets. However, I-ECAP also faces challenges, such as controlling the process steps, reducing friction between the tool and material, and minimising tool wear (Rosochowski, Olejnik, & Richert, 2008).

Rosochowski et al. (2007b) studied backward micro-extrusion of UFG Al 1070 at room temperature and found that it lowered the extrusion force and produced components with a more uniform shape, better mechanical properties, smoother surfaces, and higher dimensional accuracy. Chang and Wang (2010) and Chan et al. (2011) concluded in their studies that grain size plays a key role in microforming. They worked on copper using backward micro-extrusion at RT and reported that smaller

grains reduce the forming load and improve part accuracy, while larger grains cause unstable material flow.

Research on backward micro-extrusion using UFG materials at elevated temperatures remains limited. Saotome and Iwazaki (2001) showed that backward micro-extrusion of a fine-grained superplastic Al alloy at 500 °C successfully produce microgears with smooth surfaces and precise shapes. Meanwhile, Funazuka et al. (2022) showed that a nano-textured punch surface lowers the forming load in backward micro-extrusion by reducing friction, leading to a better surface finish.

Previous studies further suggest that the application of backward micro-extrusion using UFG materials under hot embossing and/or superplastic forming conditions is a promising approach for the present work. However, a key knowledge gap remains in understanding how UFG materials interact with process parameters during the backward micro-extrusion of miniature conical pins. Filling this gap will give useful insight into how materials deform and help improve the manufacturing of high-precision micro components.

1.2 Aim of the Research

Based on the previous subchapter on research motivation, it is important to explore the backward micro-extrusion using UFG materials under optimal process conditions to achieve better product quality.

Therefore, the aim of this research is to gain a better understanding of the material and process conditions to identify the optimal process parameters for backward micro-extrusion of a miniature conical pin.

In addition, the study seeks to verify the feasibility of selected manufacturing technologies, such as hot embossing and superplastic forming, by experimentally assessing their capability to produce accurate, defect-free, and high-precision micro-components. Furthermore, the research aims to evaluate design methodologies, including the geometry design of miniature pins, process parameter design, finite element simulation for predicting material flow and load, and the link between material, process, and product performance. These evaluations will help improve process optimisation and enable reliable fabrication of complex miniature geometries.

1.3 Objectives of the Research

The following objectives were set to achieve the stated aims:

1. To produce UFG aluminium alloy 5083 (Al 5083) using up to eight passes of the I-ECAP process.
2. To determine the microstructure of Al 5083 in the as-received (coarse-grained, CG) condition and in UFG materials subjected to four passes of I-ECAP (4P) and eight passes of I-ECAP (8P).
3. To design and develop an experimental rig for backward micro-extrusion of a miniature conical pin.
4. To simulate the backward micro-extrusion process parameters using a finite element method.
5. To study the backward micro-extrusion process parameters through experiment.
6. To compare the heights of conical pins produced using different backward micro-extrusion parameters.

1.4 Research Assumptions and Questions

This study was performed based on several assumptions related to the processing of UFG materials and microforming. It was assumed that uniform UFG microstructures were created after I-ECAP process. The friction value during the backward micro-extrusion was assumed to remain constant throughout the process, along with the ideal condition of the tool and no machine errors. The process temperature was assumed to be evenly distributed within the jig. It was also assumed that the finite element model accurately represents the real experimental conditions.

The research questions focus on determining the optimum number of I-ECAP passes and the resulting grain size, identifying the suitable process temperature ranges for both I-ECAP and backward micro-extrusion, and understanding the relationship between process temperature, pin height, and punch force-displacement. Other

questions include evaluating the percentage reduction in forming load at different process temperatures, analysing the percentage error between simulation and experimental results, and finally, identify the best parameters for backward micro-extrusion.

1.5 Research Methodology Overview

This study was structured into three main stages: material processing, material characterisation and properties, and microforming experiments, supported by numerical simulation.

This study focuses on producing products used in medical devices. Materials used in medical devices need to be corrosion-resistant and biocompatible, such as stainless steel, titanium, or cobalt-chromium alloys, to keep them safe and durable in the human body. In this study, aluminium was used instead because it is easier to machine and has good formability. The main goal is to understand the process parameters for backward micro-extrusion. The behaviour seen in aluminium is expected to be similar in medical metals. Once the process is fully understood, the jig materials can be changed to test new UFG medical metals.

In the first stage, UFG Al 5083 was produced using I-ECAP at an elevated temperature. The second stage involved characterising the processed materials, such as measuring grain size, and performing mechanical test including tensile, compression, and hardness tests. In the final stage, backward micro-extrusion was performed on both CG and UFG materials to produce the final product, called a miniature conical pin. Finite element simulations were conducted to validate the experimental findings, focusing on pin height and punch force-displacement curves.

This methodology aims to understand the effects of grain size and processing temperature in backward micro-extrusion on the final product.

1.6 Organisation of the Thesis

This section provides an overview of each chapter. The thesis consists of six chapters.

Chapter 1 introduces the research motivation, aims, objectives, research assumptions and questions, followed by an overview of the research methodology, the organisation of the thesis, and thesis-related publications.

Chapter 2 presents a literature review, discussing key topics related to this study, such as methods for strengthening metals, the ECAP process, grain growth, mechanical properties of UFG Al 5083, hot embossing and superplastic forming parameters, and the fundamentals of forward and backward micro-extrusion.

Chapter 3 describes the experimental procedures used to produce UFG Al 5083 through the double-billet I-ECAP processes that were conducted at elevated temperatures.

Chapter 4 focuses on the study of characterisation and material properties of both CG and UFG materials. Scanning Electron Microscopy (SEM) is used to examine the microstructure, while tensile, compression, and microhardness tests are conducted to determine the mechanical properties of both CG and UFG Al 5083.

Chapter 5 explains the design and setup of the backward micro-extrusion rig for producing a miniature conical pin. Experiments are carried out at RT and elevated temperatures. The images of the final products are analysed using an optical microscope, and finite element simulations are also conducted to validate the experimental results.

Chapter 6 presents the conclusions drawn from the results in Chapters 4 and 5. This chapter also highlights the main contributions of the study, suggests recommendations for future work, and discusses the limitations of the study.

1.7 Thesis-Related Publication

The research presented in this thesis has resulted in the following peer-reviewed publication:

Gzyl, M., Rosochowski, A., Boczkal, S., Olejnik, L., & Katimon, M. N. (2016). Producing High-Strength Metals by I-ECAP. *Advanced Engineering Materials*, 18(2), 219-223.

Author Contributions:

- Gzyl M. – Main author; performed the I-ECAP experiments on Mg, conducted tensile testing, analysed data, and contributed to manuscript preparation.
- Rosochowski A. – PhD supervisor; conceptualised and guided the research.
- Boczkal S. – Conducted microstructural characterisation and analysis.
- Olejnik L. – Supplied the raw material and provided technical support, specifically on the conversion coating process.
- Katimon M. N. – Performed the I-ECAP experiments on Al 5083, conducted tensile testing, and analysed data.

Key Findings:

The study demonstrated that I-ECAP significantly refines grain size, producing an ultrafine-grained structure. Multiple passes substantially increased yield strength, illustrating the potential of I-ECAP for producing high-strength metals.

Related Thesis Chapters:

- Chapter 3 – I-ECAP Processing Methodology for Al 5083
- Chapter 4 – Microstructure and Mechanical Properties Analysis

CHAPTER 2
LITERATURE REVIEW

2.1 Introduction

Products with improved quality are more likely to be preferred by consumers. However, the perception of quality varies among consumers and is subjective. The strength of a material is often associated with the perceived quality of a product. According to the Oxford Dictionary, strength is defined as 'the capacity of an object or substance to withstand great force or pressure'. The keyword is "withstand", which means to remain undamaged or unaffected by a certain level of stress. Metal strengthening can be defined as the process of increasing the strength of metals to withstand a certain level of force or pressure.

On the topic of strengthening metals, the available current techniques to enhance the strength of the materials are based either on thermomechanical processes (Uranga & María Rodríguez-Ibabe, 2020) or on grain refinement (Langdon, 2013).

There are many processes that can be used to enhance the strength of metals, thereby improving their safety and usability through thermomechanical processes. These processes are a combination of forming processes and thermal processes. The first step typically involves a hot metal forming method such as rolling, forging, or extrusion, which reshapes the cast billet as well as improves its mechanical properties by eliminating the cast structure. This process can be followed by other thermal processes to further increase metal strength.

This chapter also discusses the relationship between material strength and grain size. The smaller the grain size, down to the UFG level, the more durable the material becomes (Lasalmonie & Strudel, 1986). UFG materials can be produced through grain

refinement strategies, using either a 'bottom-up' or 'top-down' approach (Valiev & Langdon, 2006).

2.2 Strengthening Through Grain Refinement

Grain refinement is a method to reduce the size of crystallites (grains) in metals and consequently increase their strength. The Hall-Petch theory was proposed to explain this effect. In this theory, the grain boundary is assumed to act as an obstacle to dislocation motion. Dislocations are emitted from within a grain, move along a slip plane, and propagate towards the grain boundary. Once the grain boundary blocks the leading dislocation, the trailing dislocations stop behind it due to mutual repulsion. The formation of dislocation pile-ups caused stress concentrations at grain boundaries. Slip propagation from one grain to the next therefore requires a higher applied stress (Hansen, 2004). The Hall-Petch relationship, shown in Equation (2.1), describes the dependence of yield stress on grain size (Shanmugasundaram et al., 2010).

$$\sigma_y = \sigma_0 + \left(\frac{k_y}{\sqrt{d}}\right) \tag{2.1}$$

where σ_y is the yield stress, σ_0 is the material constant defining the initial stress required for dislocation movement, k_y is the strengthening coefficient (or Petch parameter), and d is the average grain diameter.

The Hall-Petch equation shows that the strength of metals is inversely proportional to the square root of grain size. However, there is a limit to the level of strength achieved because, at a certain grain size, the strength of the metal remains constant. Nieh and Wadsworth (1991) explained that, at this point, each grain no longer supports more than one dislocation, making the Hall-Petch theory inapplicable.

2.2.1 Bottom-Up Approach

The bottom-up approach means building the material from particles through powder metallurgy, electrodeposition, or rapid solidification. Powder metallurgy can produce parts with improved mechanical properties, provided that very fine-grained powders are used (Pickens, 1981). Powder metallurgy involves the processes of powder production, blending powders and compacting them into a desired shape known as a green compact, and finally sintering.

There are four main methods to produce powder materials, which are solid-state reduction, atomisation, electrolysis, and chemical processes. However, these powder production methods are generally incapable of producing nanocrystalline (NC) size or UFG grains. Therefore, CG powders are processed further by ball milling, which involves a cylinder rotating about its axis. This cylinder is filled with the powder metal that is to be ground and the grinding medium (balls). It normally takes a long time to produce powders with NC or UFG structures. Prolonged ball milling may produce a finer grain size, but this will lead to severe sticking of the powder to the milling tools. Severe sticking requires scraping off the powders at frequent intervals and contributes to a time-consuming process. Contamination is another major issue in the ball milling method. Contamination from the milling tools and impurities coming from the environment's gases, such as oxygen and nitrogen, can alter the final properties of the powder.

High-energy ball milling has been introduced to overcome the long processing time required in conventional milling. This method involves high-velocity collisions between the milling balls and the inner walls, which repeatedly fracture and cold-weld powder particles (Suryanarayana, 2001). Therefore, higher energy impacts are produced compared to conventional methods. Yadav et al. (2005) reported that high-energy ball milling at 400 rpm required 10 hours and 80 hours to achieve average grain sizes of 95 nm and 17 nm, respectively using $Al_{50}Cu_{28}Fe_{22}$ alloy.

Sintering is a thermal treatment applied to green compacts to increase strength through particle bonding. During this process, recrystallisation and grain growth may occur in the sintered material. Recrystallisation is the formation of a new grain structure when the material is exposed to temperatures above the recrystallisation

temperature. Recrystallisation and grain growth decrease the yield strength of a hardened metal. A review by Fang et al. (2009) showed that sintering at temperatures above 1000 °C is incapable of retaining the nanograin size in tungsten carbide (WC-Co).

Powder metallurgy can often produce porous parts, and this could become a liability (Upadhyaya, 1997). Hot isostatic pressing (HIP) is one of the methods used to decrease the porosity in powder-based products. HIP is based on the simultaneous application of heat and high inert gas pressure to the encapsulated powder. Nevertheless, Tang et al. (2005) found that after HIP and hot rolling, the grain size of the Al 5083/SiCp composite increased from 30 nm to approximately 100-200 nm. Thus, sintering reduces the effectiveness of ball milling in producing NC metals. Other difficulties include storing and handling metal powders due to their small particle sizes, the high cost of metallic powders, and the high tooling and equipment cost, particularly for compacting and sintering steps.

Electrodeposition, or electrochemical deposition, is a process in which metal ions in a solution are driven by an electric field to coat an electrode. The part to be coated is the cathode, while the anode serves as the source of metal ions to be deposited. Both electrodes are immersed in a chemical solution that permits the flow of electricity. The anode and cathode are connected to the positive and negative terminals, respectively, as shown in Figure 2.1.

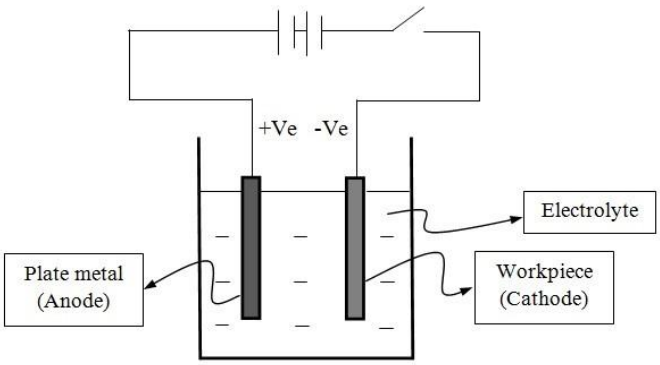

Figure 2.1: A basic circuit for an electrodeposition operation.

When an electric current is applied, cations with a positive charge from the solution are attracted to the negatively charged cathode and deposited on the cathode. As replenishment for these deposited cations, the metal from the anode is dissolved

and goes into a solution to balance the ionic potential. These cations will coat the cathode (part) continuously until it creates a required layer on the part. Research by Cheung et al. (1995) showed that pulsed direct current could produce NC nickel with an average grain size of less than 11 nm. This approach is called pulse electrodeposition. NC structures are obtained by adjusting process parameters such as current density, overvoltage, pulse parameter, bath composition, and temperature. The electrodeposition technique has advantages over other methods for synthesising NC materials, such as the potential for synthesising a large variety of nanograin materials, low investment, and high production rates. In contrast, the disadvantage was the shape limitation of the product, which consisted of a relatively thin deposited layer (Meyers et al., 2006).

Rapid solidification refers to a process that changes the condition of a material from a liquid state at high temperature, to a solid material at RT. According to Lavernia and Srivatsan (2010), these changes of state require a fast cooling rate of at least 10^4 K/s to achieve microstructural refinement. There were three different cooling methods, namely imposing a high degree of undercooling before solidification, high velocity of advance during continuous solidification, and high cooling rate during solidification. To achieve such high cooling rates throughout the material, its thickness usually needs to be very small, which limits the application of rapid solidification to thin strips of metal.

2.2.2 Top-Down Approach

The top-down approach starts with bulk metal and involves subdividing the grains by SPD. SPD can be defined as a process that involves plastic deformation of a metal to a certain value of strain, to convert its CG structure to either UFG or NC structure, without producing substantial changes in the initial shape and dimensions of the billet. Compared with powder metallurgy or electrodeposition, SPD produces a large bulk of non-porous samples. The exact nature of grain refinement due to SPD is still debated.

Typically, there are two types of mechanisms to explain grain refinement. The first type is grain boundary dislocation, while the second type relates to shear band formation. This dislocation mechanism was explained by Meyers et al. (2006), as

shown in Figure 2.2. During plastic deformation, a combined grain-boundary source sink model evolved. These dislocations that met the opposing grain boundary acted as a sink. As grain boundary dislocation was severely limited, the grain size was reduced.

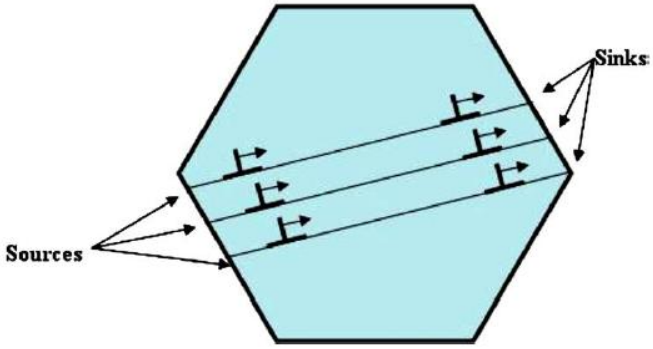

Figure 2.2: Grain boundary source-sink model (Meyers et al., 2006).

The second mechanism, described by Wei et al. (2002) that involves grain refinement through the formation of shear bands during the onset of plastic deformation. Shear localisation appears after plastic deformation begins, and with increasing strain, existing bands continue to develop alongside multiple new shear bands. Finally, new grains form within the shear bands. Figure 2.3 shows TEM images of the development of these shear bands.

Edalati et al. (2024) showed that dislocation accumulation, subgrain formation, and dynamic recovery at grain boundaries helped refine grains during severe plastic deformation, supporting the grain-boundary dislocation mechanism. They also pointed out that shear banding, which created small zones of intense deformation, helped new ultrafine grains form. Although the exact mechanisms are still not fully understood, both grain-boundary dislocations and shear banding explain how ultrafine grains develop and why metals exhibit higher strength.

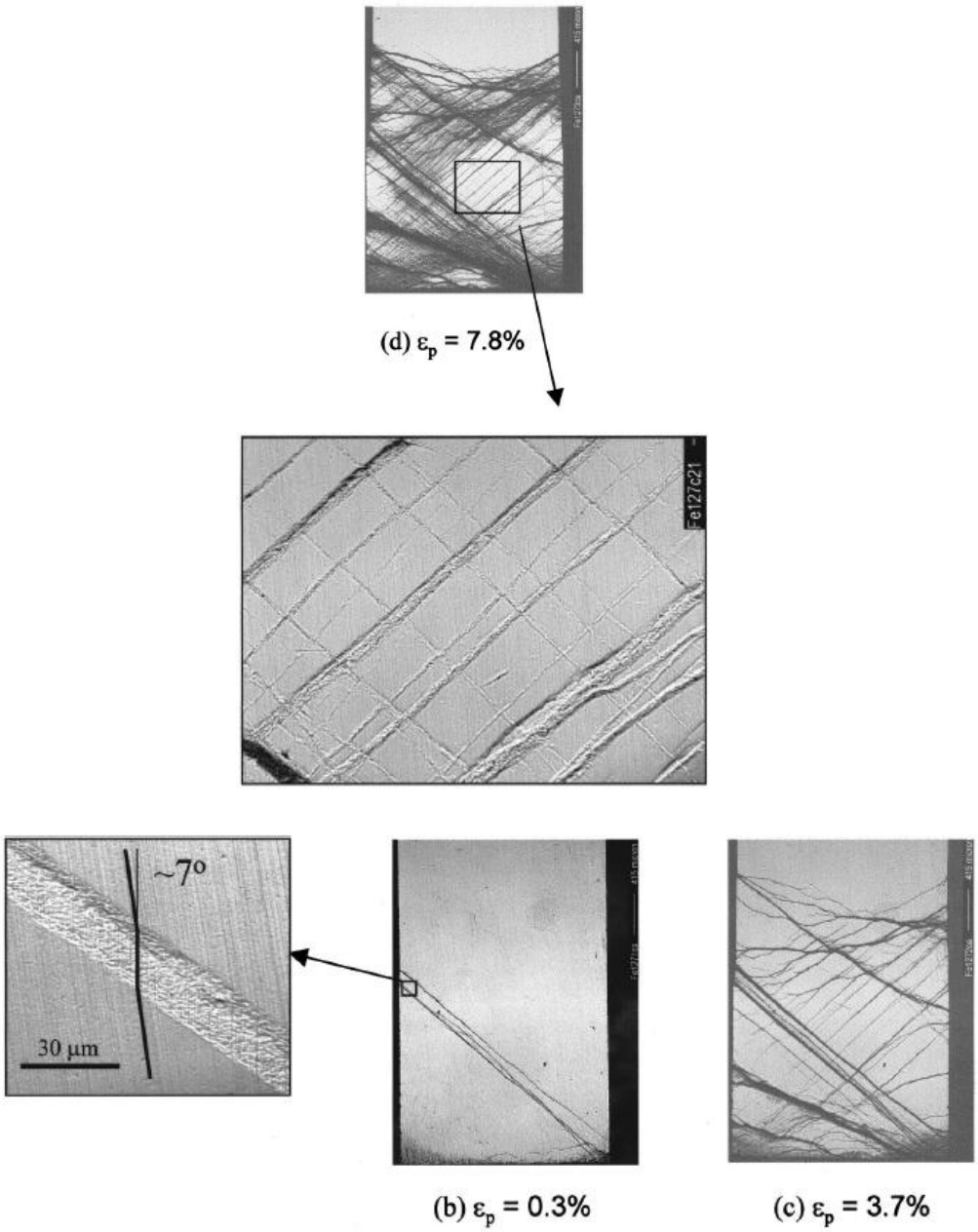

Figure 2.3: TEM images of development of the shear bands at various strain levels (0.3%, 3.7% and 7.8%) (Wei et al., 2002).

SPD processes are generally divided into two groups: batch and continuous. Batch processes use compact billets with approximately equal dimensions, while continuous processes can refine the grain structure in long billets. The major batch SPD processes include high-pressure torsion (HPT), equal channel angular pressing (ECAP), cyclic extrusion compression (CEC), repetitive corrugation and straightening (RCS), and twist extrusion (TE). Well-known continuous SPD processes include

accumulative roll bonding (ARB), continuous repetitive corrugation and straightening (CRCS), ECAP-Conform, and continuous confined strip shearing (CCSS/C2S2).

2.2.2.1 Batch SPD Processes

The principle of HPT is based on the classic work of Bridgman (1943), who experimented with a cylindrical or tubular specimens subjected to a substantial compressive load (up to 5700 kg/cm^2) and simultaneous twisting by a large angle. The results showed that no fracture occurred in the specimen as an increasing compressive load significantly increased the ductility. In his study, Bridgman did not mention anything related to microstructure. The same approach was later used for disk samples, which enabled the producing of materials with UFG or NC structures. For HPT, as shown in Figure 2.4, the equivalent strain ($\varepsilon(r)$) is expressed by Equation (2.2) (Azushima et al., 2008).

$$\varepsilon(r) = \frac{2\pi nr}{l\sqrt{3}} \tag{2.2}$$

where r is the distance from the axis of the disk, n is the number of rotations, and l is the thickness of the sample.

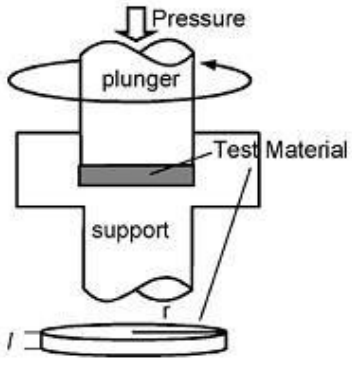

Figure 2.4: Schematic illustration of the thin disc HPT process (Azushima et al., 2008).

According to Equation (2.2), the maximum imposed strain occurs near the edge and reduces to zero at the centre. Consequently, the hardness at the centre is expected to be significantly lower than at the edge. This behaviour was confirmed for Al-0.5Mg, Al-1Mg, Al-6061, and Al-0.01 alloys after the HPT process was conducted through one turn at RT (Kawasaki et al., 2011). Bhovi et al. (2016) investigated the hardness of Al-3Mg-0.25Sc alloy subjected to up to five turns of HPT at RT. As shown in Figure 2.5, the hardness near the centre gradually increased with the number of turns until it reached a nearly uniform distribution across the disc after five turns.

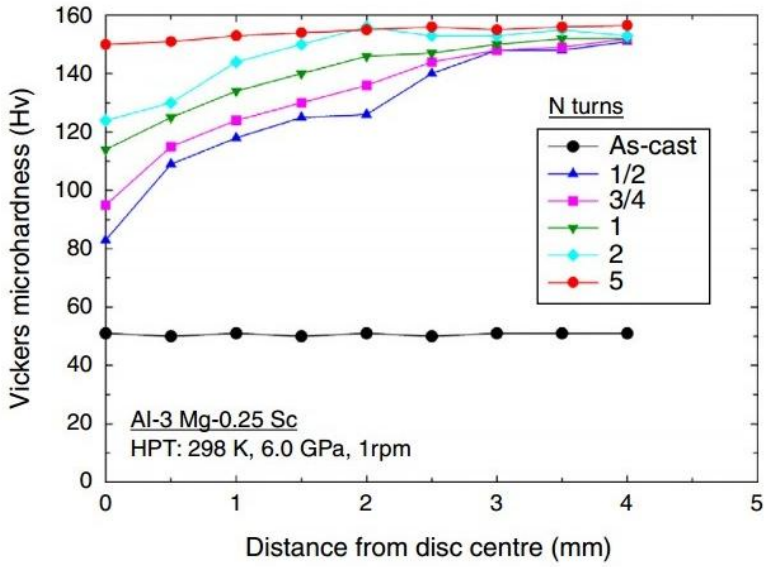

Figure 2.5 : Vickers microhardness of an Al-3Mg-0.25Sc disc subjected to HPT at RT with different numbers of turns (Bhovi et al., 2016).

HPT can produce a finer grain structure than other SPD processes. For example, HPT of copper (99.98%) to a true strain of 7 at RT and a pressure of 7 GPa produced a mean grain size of 100 nm (Valiev et al., 2000). However, due to the very high pressure, the tools made must be very strong, which increases their cost. HPT generally involves the processing of thin disks, which is not of much use for practical applications. In addition, a special dedicated machine must be built, which increases the cost further.

ECAP, also called equal channel angular extrusion (ECAE), is the most popular SPD method because of its low force requirement and simple tool geometry. Segal invented conventional ECAP in 1977 with the objective to develop a metal

forming process in which high strains can be introduced into the metal billet by simple shear (Azushima et al., 2008). When the billet is side extruded through the channel, as shown in Figure 2.6, the total strain, (ε) is expressed by Equation (2.3) (Iwahashi et al., 1996).

$$\varepsilon = \frac{1}{\sqrt{3}}\{2cot(\phi/2 + \psi/2) + \psi cosec(\phi/2 + \psi/2)\} \quad (2.3)$$

where ϕ is the angle of intersection of two channels (die channel angle), and ψ is the angle subtended by the arc of curvature at the point of intersection.

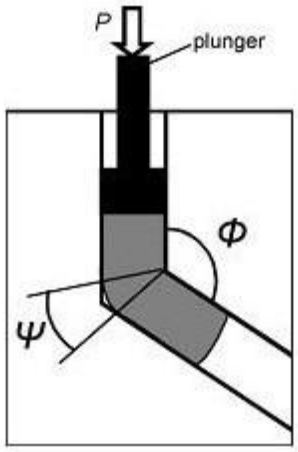

Figure 2.6 : Schematic representation of the ECAP process (Azushima et al., 2008).

To achieve the required strain in ECAP, the billet is processed repeatedly in the same die. The billet can be rotated about its axis between consecutive passes of ECAP. There are four basic rotation options, designated as A, C, B_A, and B_C as shown in Figure 2.7. In route A, the billet is processed without rotation; in route B_A, the specimen is rotated by 90° in alternating directions; in route B_C, the specimen is rotated by 90° in the same direction each time; and in route C, the specimen is rotated by 180°. Among the processing routes for the die channel angle ϕ of 90°, route B_C has been proven to be the most effective for producing homogeneous microstructures (Stolyarov et al., 2001; Oh-Ishi et al., 1998). Oh-Ishi (1998) carried out ECAP at RT using high-purity (99.99%) aluminium, while Stolyarov (2001) focused on commercial-purity titanium, with processing temperatures starting at 450 °C.

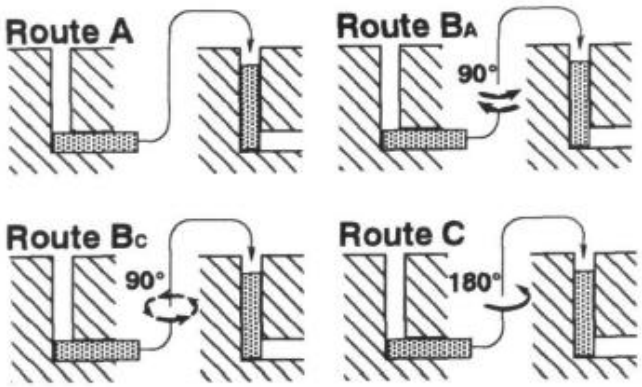

Figure 2.7: Schematic illustration of the four ECAP routes (Horita et al., 1999).

However, homogeneous microstructures produced by route B_C do not necessarily have finer grains. Prangnell et al. (2004) conducted a study using electron backscatter diffraction (EBSD) on two types of UFG materials (Al-3Mg and Al-0.1Mg) produced by ECAP using routes A, B_C, and C with the number of passes up to very high plastic strains ($\varepsilon > 7$). The experiments were conducted with a die channel angle of 90° and at different process temperatures (20 °C and 200 °C).

The results (Figure 2.8) showed that route A produced the smallest grains for Al-3Mg, while route B_C was slightly more effective for Al-0.1Mg. They also showed that smaller grains were accompanied with a higher fraction of high-angle grain boundaries (HAGB). Grain boundary misorientation is generally divided into two categories: low-angle grain boundaries (LAGB) and HAGB. LAGB and HAGB refer to grain boundary misorientation angles between 2° - 15° and more than 15°, respectively. The details of this classification were described by Lejček (2010).

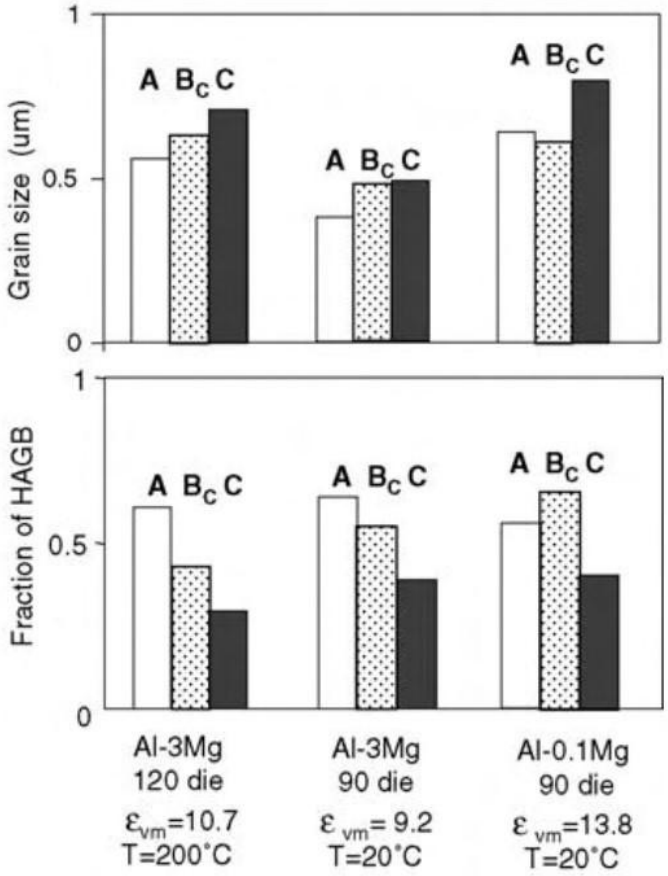

Figure 2.8: Column charts showing grain size and fraction of HAGB for different materials and ECAP routes, as measured by EBSD (Prangnell et al., 2004).

The advantage of ECAP is that it can process large bars and plates (Ferrasse et al., 2008; Frint et al., 2016). Hence, the variety of products can be produced. However, there are some limitations to this process. First, the length of the specimen is limited by the aspect ratio (length/diameter), which must remain below a critical value of about 6-10 to prevent excessive process force from friction in the channel and to avoid buckling of the slender punch during pressing. Second, a significant length near each end of a processed billet contains material with a non-uniform strain distribution and microstructure, which has to be discarded, consequently increasing the cost of producing UFG metals (Raab et al., 2004). Third, this process cannot be directly applied to sheet metal. Furthermore, ECAP is not well suited for industrial operations because it involves a repetitive process of inserting the billet into the die.

According to Richert et al. (2003), the original method of CEC was patented in Poland in 1979. This method combines forward extrusion and compression in a

single deformation cycle, which is repeated several times to achieve a large and uniform strain. The details of the CEC process were explained by Richert and Korbel (1995). Referring to Figure 2.9, the accumulated equivalent strain (ε) is expressed by Equation (2.4) (Azushima et al., 2008),

$$\varepsilon = 4n\ln(D/d) \tag{2.4}$$

where D is the chamber diameter, d is the channel diameter, and n is the number of deformation cycles.

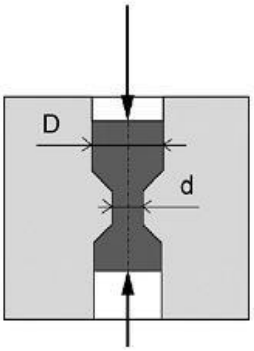

Figure 2.9: Schematic diagram of CEC (Azushima et al., 2008).

Due to the substantial opposing forces applied to the material, CEC generates high hydrostatic pressure. As a result, some sections of the die are subjected to high contact stress (Rosochowski, 2005). Special tool steels and pre-stressed tools are required to increase tool life. Therefore, CEC is better suited for processing soft materials such as aluminium alloys.

Huang et al. (2001) developed a new technique called RCS. A basic RCS cycle consists of two steps, namely corrugation and straightening. In this process, a workpiece is repetitively bent and straightened. Figure 2.10 shows the die set used for the corrugating and straightening step. The straightening is accomplished by pressing the corrugated workpiece between two flat platens. As shown in Figure 2.10, the equivalent strain (ε) per operation is expressed by Equation (2.5) (Azushima et al., 2008).

$$\varepsilon = 4\ln\frac{[(r\ +\ t)/(r\ +\ 0.5t)]}{\sqrt{3}} \tag{2.5}$$

where t is thickness of the specimen and r is curvature of the bent zone.

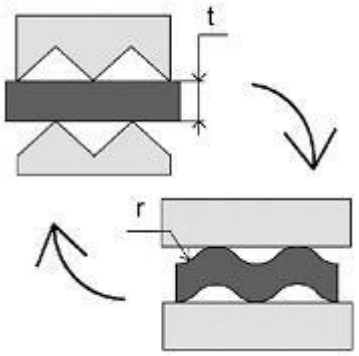

Figure 2.10: Principle of RCS (Azushima et al., 2008).

According to Beygelzimer et al. (2009), TE is based on pressing a prism-shaped specimen through a die with the profile consists of two prismatic regions separated by a helical twist part. TE is performed under high hydrostatic pressure, which is generated by applying backpressure to the billet as it exits the die. Four separate deformation zones are formed, as shown in Figure 2.11. Their study focused on investigating the strain intensity within these deformation zones.

The research proved that the geometry of the die cross-section plays an important role in the non-uniform strain intensity distribution achieved at the end of the process. As shown in Figure 2.12, the average strain (ε_{ave}) is distributed within the cross-section of the specimen, where the minimum (ε_{min}) and maximum (ε_{max}) accumulated strain after one pass can be estimated using the simplified expressions in Equations (2.6) and (2.7) (Orlov et al., 2009).

$$\varepsilon_{min} \approx 0.4 + 0.1 tan\beta \tag{2.6}$$

$$\varepsilon_{max} \approx \frac{2}{\sqrt{3} tan\beta} \tag{2.7}$$

where β is the twist angle.

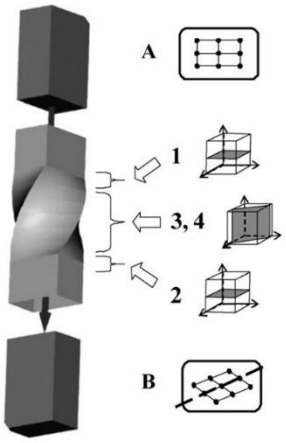

Figure 2.11: The position of the four deformation zones in TE (Beygelzimer et al., 2009).

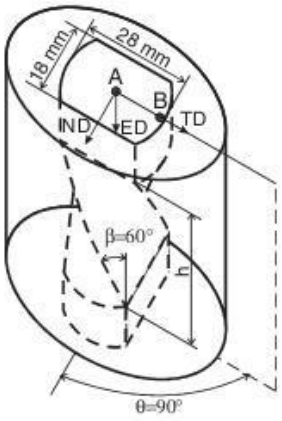

Figure 2.12: Schematic diagram of TE (Orlov et al., 2009).

2.2.2.2 Continuous SPD

ARB was first proposed by Saito et al. (1998). Figure 2.13 shows the sequence of operations in this process, in which the rolled material is cut into two sheets, after being surface treated and stacked together, are rolled again to reduce the total thickness of the pack by 50%. This sequence can be repeated indefinitely, allowing a very large plastic strain to be achieved. As shown in Figure 2.14, the equivalent plastic strain (ε) after n cycles of ARB is expressed by Equation (2.8) (Rosochowski, 2004).

$$\varepsilon = n\frac{2}{\sqrt{3}} ln\left(\frac{T}{t}\right) \tag{2.8}$$

where T is the initial thickness of the stacked sheets and t is the thickness after roll.

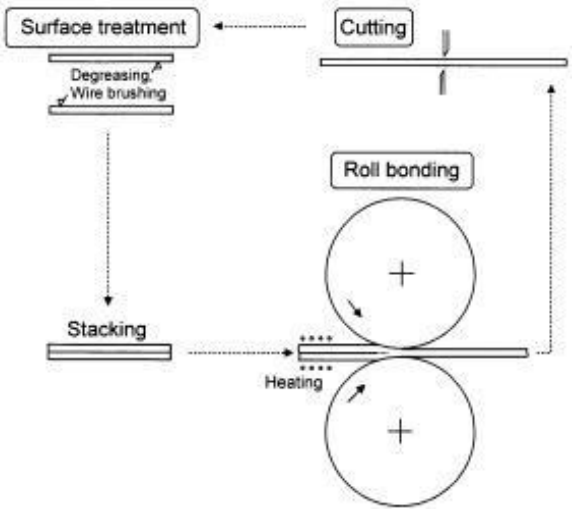

Figure 2.13: Schematic illustration of the ARB process principle (Saito et al., 1998).

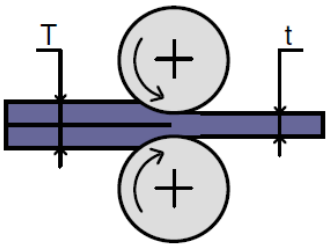

Figure 2.14: Schematic illustration of ARB (Rosochowski, 2004).

Huang et al. (2004) focused on developing a new version of the RCS process to produce a continuous bulk of nanostructured materials. This modified design, termed as CRCS, as shown in Figure 2.15, produces continuous strips of materials. Corrugation is achieved using a pair of gear-like rollers, while another pair of rollers presses the corrugated strips to achieve straightening. Experimental trials revealed certain limitations of the CRCS process, such as the formation of fatigue cracks and non-uniform strain distribution on the surface of the processed material.

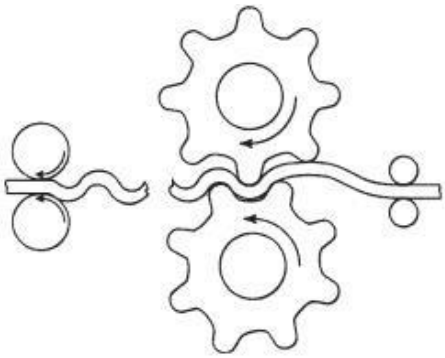

Figure 2.15: Schematic of CRCS (Huang et al., 2004).

The ECAP-Conform process was introduced by Raab et al. (2004); it combines ECAP with the Conform process as shown in Figure 2.16. Conform is a continuous extrusion forming technique, which uses the frictional force between a circular feeding wheel and the material. The results showed that ECAP-Conform can produce specimens of Al 99.95% with a grain size of approximately 650 nm after four passes. However, only a minimal change of the ultimate tensile strength (UTS) was observed between the first and fourth passes, which are 160 MPa and 180 MPa, respectively.

Another study by Polyakov et al. (2011) showed that the UTS of Ti Grade 4 after the first and fourth passes of ECAP-Conform reached nearly 950 MPa and 1050 MPa, respectively. For ductility, the value of 12% elongation remained unchanged between two and eight passes. From these results, the increase in UTS after four passes ranged between 10% to 15%. However, ECAP-Conform requires very high torque to ensure a successful process. Higher torque involving high-capacity motor resulted in a high cost needed to build this machine.

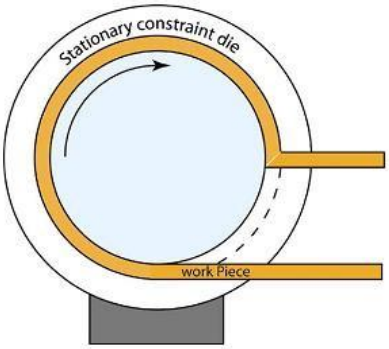

Figure 2.16: Schematic illustration of the ECAP-Conform setup (Raab et al., 2004).

Lee et al. (2001) proposed a continuous SPD process based on ECAP and Conform, called CCSS/C2S2, as illustrated in Figure 2.17. This new process concept enables the production of metal strips in a continuous manner with high formability. The metal strip passes through the ECAP channel at controlled speeds by guide and feeding rolls, which allows multi-pass operation. An outstanding increase in hardness was achieved after four passes. However, the hardness decreased linearly from the fifth pass onwards (Lee et al., 2002).

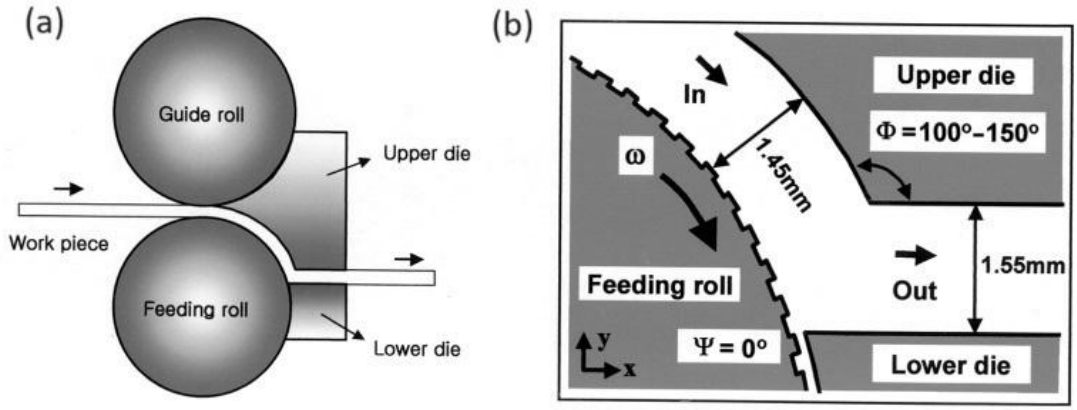

Figure 2.17: Schematic illustration of the CCSS/C2S2 process (a), and the details of the ECAP channel (b) (Lee et al., 2001).

2.3 Effect of ECAP Processing Temperature on Mechanical Properties of Al 5083

Horita et al. (2000b) found cracks in Al 5083 specimens after four passes of ECAP at RT. In contrast, no cracks were reported for Al 5083 when ECAP was conducted at elevated temperatures.

Chang et al. (2005) studied the effects of ECAP processing at 373 K and 473 K on the material properties of commercial Al 5083. All specimens were annealed at 723 K for 1 hour prior to ECAP. The average grain size of the CG specimens was approximately 200 μm. ECAP conducted up to eight passes (route C) resulted in an average grain size of about 0.3 μm at both processing temperatures. Tensile tests were carried out at an initial strain rate of 1×10^{-3} s^{-1} at RT.

Figure 2.18(a) and Figure 2.18(b) present the tensile results obtained at processing temperatures of 373 K and 473 K, respectively. This study demonstrates that increasing the processing temperature to 473 K significantly reduces the material strength by up to 25% compared to 373 K. However, the strength and ductility of specimens with different numbers of passes were almost the same for ECAP processing at 473 K. In contrast, ECAP at 373 K produced different yield strengths, UTS values, and elongations to failure depending on the number of passes. Chang et al. reported that the grain boundaries formed at 373 K were less distinct than those at 473 K. TEM images further revealed that ECAP at 473 K produced a higher fraction of a HAGB compared to ECAP at 373 K.

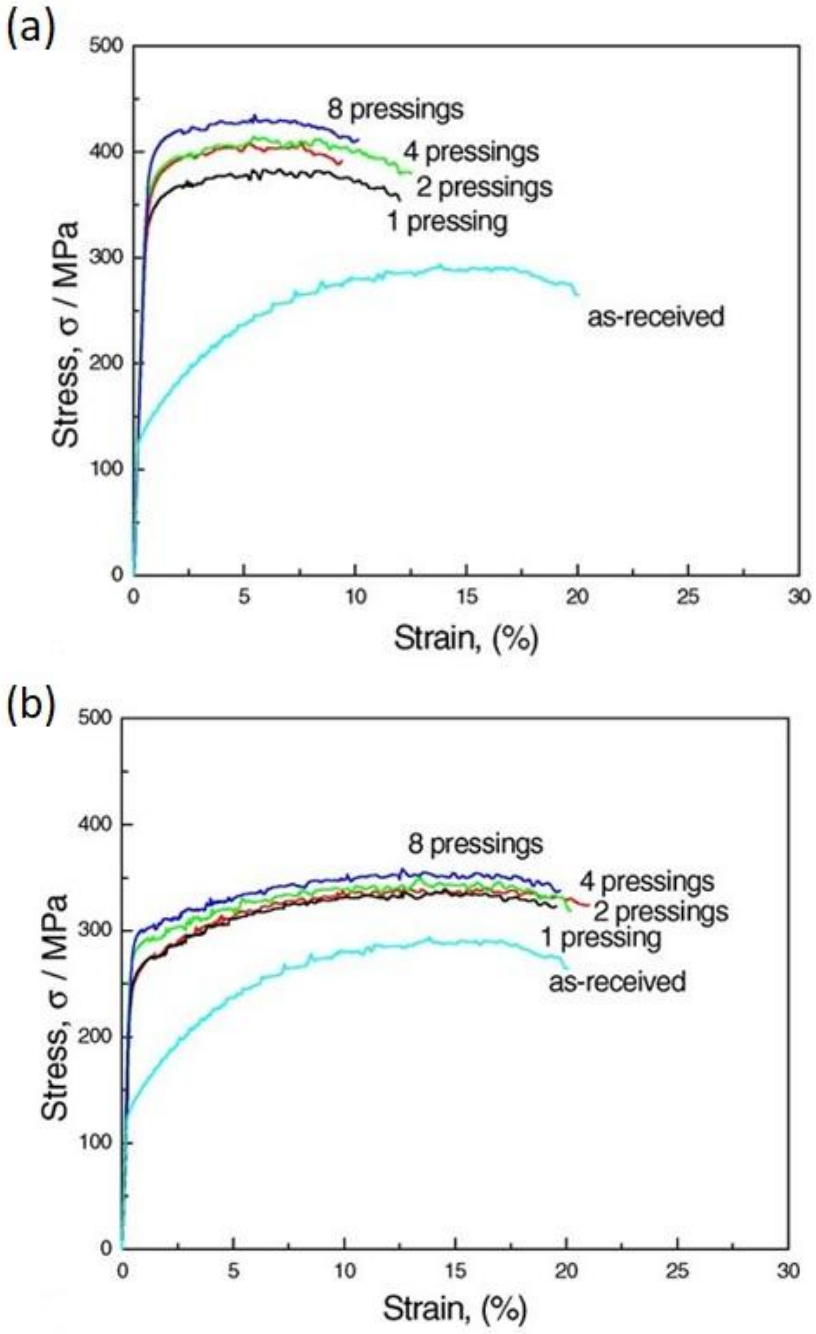

Figure 2.18: Tensile stress-strain curves at RT for Al 5083 subjected to route C ECAP at 373 K (a), and 473 K (b) (Chang et al., 2005).

2.4 Influence of ECAP Passes on Mechanical Properties

Horita et al. (2001) investigated the effect of ECAP at different numbers of passes on six different commercial fully annealed Al alloys (1100, 2024, 3004, 5083, 6061 and 7075). ECAP with a die channel angle of 90° was conducted at RT for up to eight passes using route B_C. Al 5083 underwent only three passes of ECAP, as cracks started to appear at the fourth pass. Tensile tests were carried out at RT for all materials with an initial strain rate of 3.3×10^{-4} s^{-1}. For Al 5083, the 0.2% yield stress of the as-received material and after one, two, and three passes was 170 MPa, 390 MPa, 410 MPa, and 420 MPa, respectively (Figure 2.19).

Compared to the other aluminium alloys, Al 5083 exhibited the highest yield stress after three passes of ECAP. This study shows that increasing the number of passes significantly enhances the strength of the material.

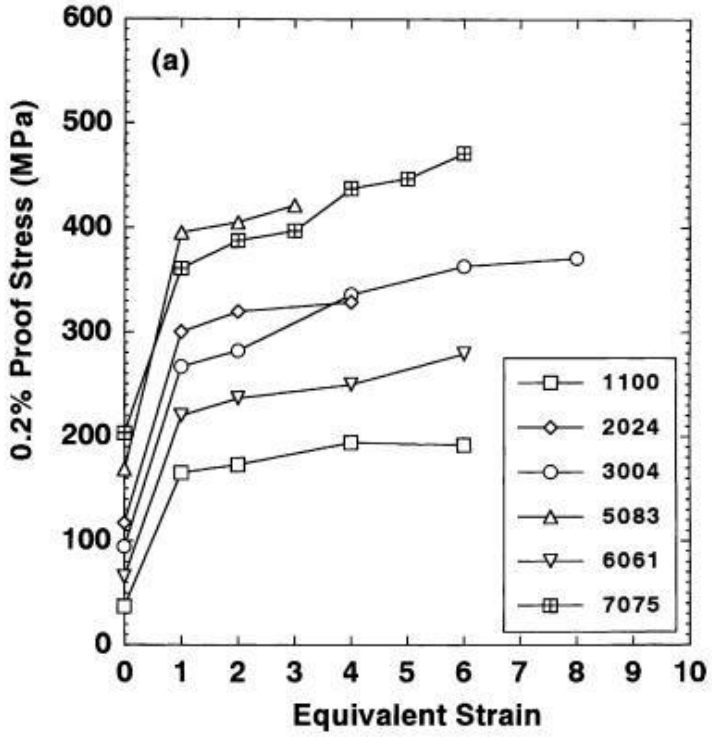

Figure 2.19: 0.2% yield stress of Al alloys processed by ECAP at RT using route B_C (Horita et al., 2001).

Further research by Park et al. (2004) found no significant difference in the average grain sizes (0.3 μm) between four and eight passes; the difference was observed only in the grain boundary misorientation. The results showed that eight passes produced a higher fraction of HAGB. For comparison, the HAGB fraction increased from approximately 35% after four passes to about 50% after eight passes, as shown in Figure 2.20.

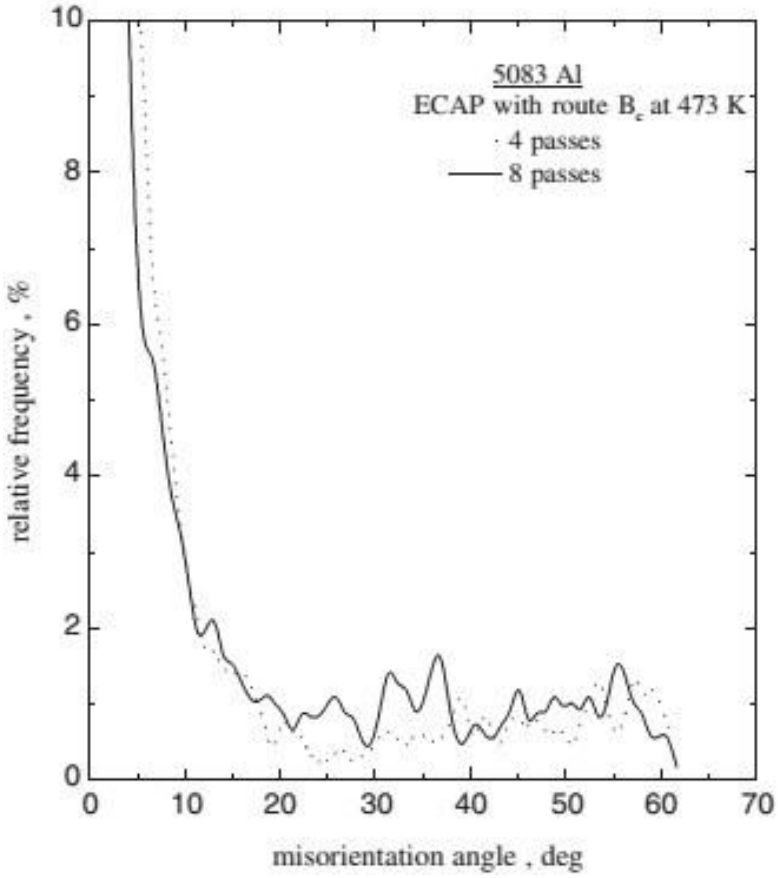

Figure 2.20: Relative frequency of grain boundary misorientation angles for Al 5083 subjected to ECAP using route B_C at 473 K (Park et al., 2004).

In addition, as shown in Figure 2.21, the elongation to failure after eight passes was higher than that after four passes. This behaviour may be related to the larger fraction of HAGB. From the stress-strain curve for eight passes, the maximum elongation to failure was recorded as 315% under testing conditions of a 5×10^{-4} s^{-1} strain rate and a temperature of 548 K.

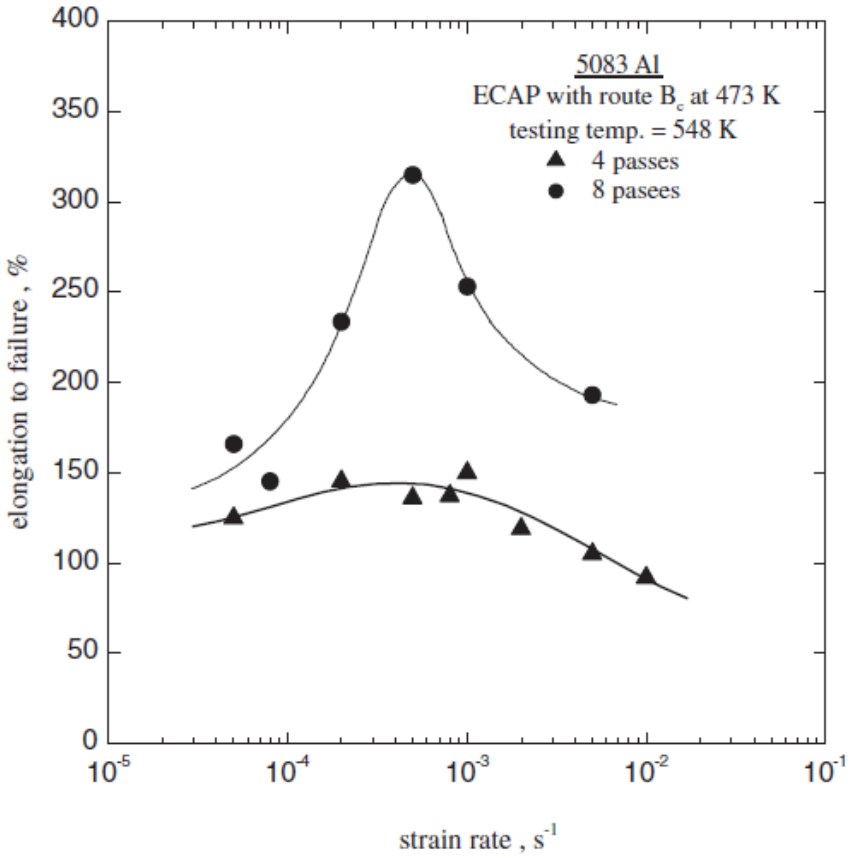

Figure 2.21: Variation of elongation to failure at 548 K for Al 5083 subjected to 4 and 8 passes of ECAP at 473 K, plotted as a function of the initial strain rate (Park et al., 2004).

A similar trend was also reported by Kawasaki et al. (2009). In their study, ECAP was performed at RT using route B_C with a 90° die channel angle for up to 12 passes on high-purity (99.99%) aluminium. No notable changes in average grain size were observed from four to twelve passes. However, the fraction of HAGB increased from 11% after one pass to 50% after four passes, 53% after eight passes, and 74% after twelve passes.

2.5 Effect of Temperature on Grain Growth of Al 5083

The production of UFG materials at high temperatures should be done at the right temperature to prevent grain growth. Several studies have examined how Al 5083 behaves during grain growth after ECAP and heat treatment.

Dupuy et al. (2000) studied the thermal stability of Al 5083 that underwent four passes of ECAP using a 90° die channel angle and route BC at 150 °C. After that, the material was annealed at temperatures between 160 °C and 360 °C for one hour. Figure 2.22 shows that as the annealing temperature increases from 160 °C to 200 °C, the hardness remains nearly constant at 130 HV, but it drops sharply above 240 °C. This study suggests that the optimum post-ECAP processing temperature for Al 5083 is around 200 °C.

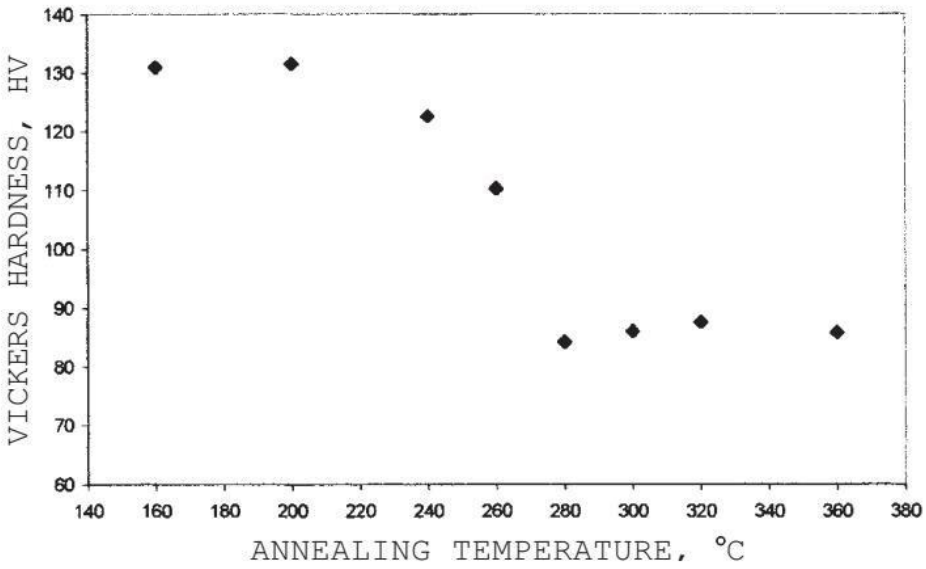

Figure 2.22: Vickers hardness of Al 5083 after four passes of ECAP at 150 °C (route B_C) and one-hour annealing at various temperatures (Dupuy et al., 2000).

Research by Park et al. (2002) reported a similar trend, as shown in Figure 2.23. The material underwent eight passes of ECAP at 473 K (~200 °C) with a 90° die channel angle using route B_C. Post-ECAP annealing was carried out for one hour at temperatures between 323 K and 773 K. The hardness stayed almost the same, around 135 HV, for annealing temperatures between 323 K and 423 K. When the temperature increased from 473 K to 573 K, the hardness slowly decreased and then became almost constant between 573 K and 773 K. This drop in hardness was linked to grain growth, as shown by the TEM images.

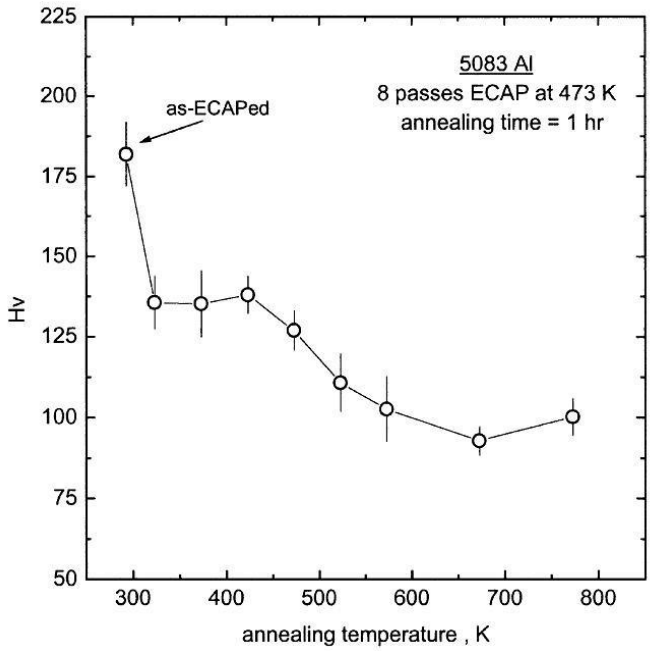

Figure 2.23: Variation of microhardness with annealing temperature after eight passes of route B_C ECAP at 473 K (Park et al., 2002).

Another study by Roy et al. (2006) showed no significant grain growth for UFG Al 5083 at 473 K (~200 °C), even after prolonged annealing for 50 hours, as shown in Figure 2.24. Significant grain growth was observed in TEM results at temperatures above 573 K (~300 °C).

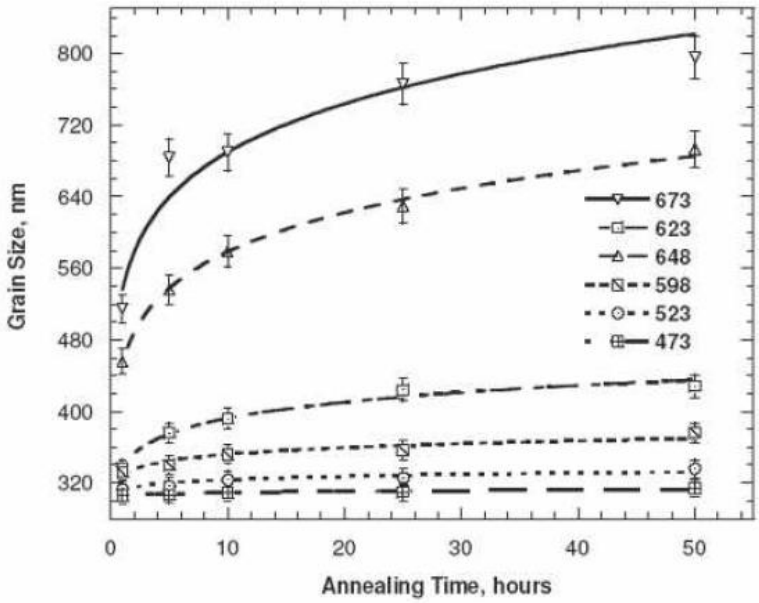

Figure 2.24: Grain size as a function of annealing time at different temperatures for UFG Al 5083 (Roy et al., 2006).

2.6 Mechanical Properties of UFG Al 5083

Park et al. (2005) performed compression tests at RT (298 K) and cryogenic temperature (77 K) using coarse-grained (CG, annealed at 773 K for two hours) and UFG Al 5083. The UFG materials were produced by up to eight passes of ECAP using route B_C at 473 K, followed by annealing at 453 K for 48 hours.

Compression tests were carried out on cylindrical specimens measuring Ø6 mm × 9 mm (aspect ratio 1.5) at an initial strain rate of 0.001 s^{-1}, followed by a constant crosshead speed. The microstructures of both CG and UFG annealed materials exhibited nearly uniform size distributions, with average grain sizes of approximately 40 µm and 0.5 µm, respectively. The results of this test are shown in Figure 2.25. The approximate 0.2% yield stresses for the CG and UFG materials at 298 K were 140 MPa and 500 MPa, respectively. This study shows that, at RT, the 0.2% yield stress of UFG Al 5083 is about 3.5 times higher than that of CG Al 5083.

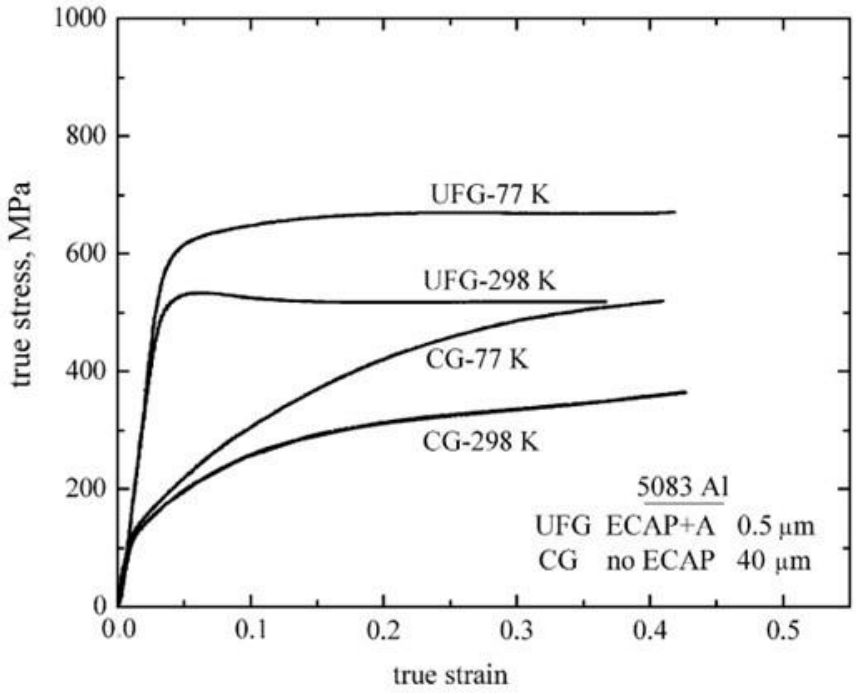

Figure 2.25: True compression stress-strain curves for CG and UFG Al 5083 (ECAP route B_C) at RT (298 K) and cryogenic temperature (77 K) (Park et al., 2005).

Witkin et al. (2005) carried out compression testing on Al 5083 at RT and up to 573 K, using constant strain rates from 5×10^{-5} to 10^{-2} s^{-1}. The material was processed by HIP of cryomilled powders followed by extrusion. Compression samples with a height-to-diameter ratio of 1 were lubricated with molybdenum disulphide. The average grain size of these samples was 0.138 μm.

Figure 2.26 shows the compression true stress-true strain curve at a constant strain rate of 10^{-3} s^{-1}, corrected for machine compliance. At RT and 373 K, the curves gradually increased with strain due to work-hardening. At 423 K and higher temperatures up to 573 K, the curves remained nearly flat.

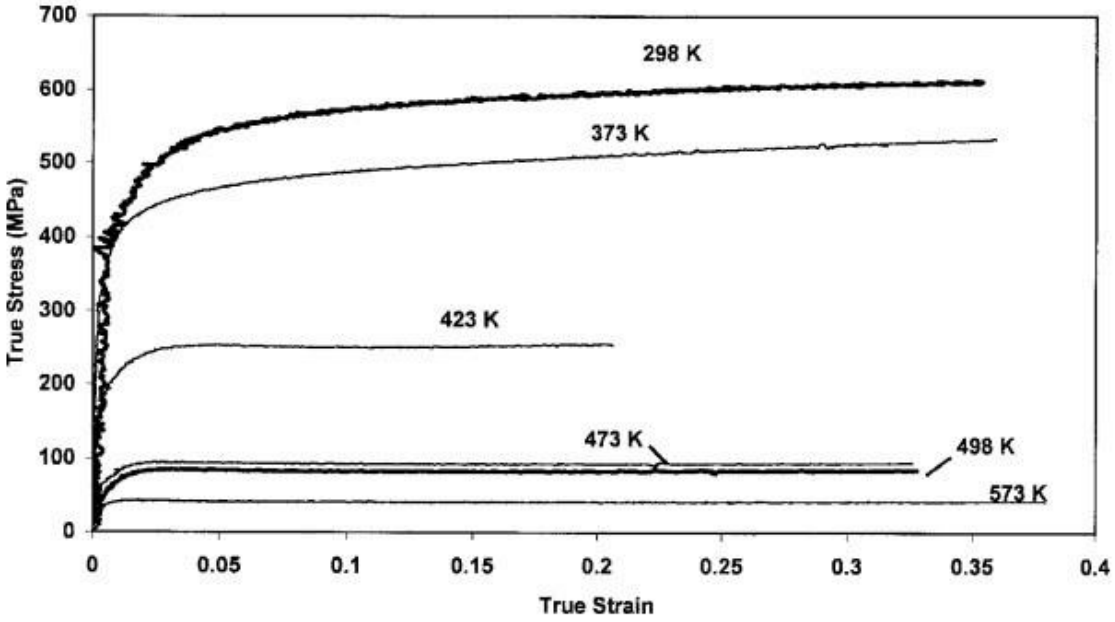

Figure 2.26: True compression stress-strain curves for UFG Al 5083 at various temperatures (Witkin et al., 2005).

Similar results were obtained by Tokarski et al. (2012). The authors performed compression tests from RT up to 450 °C at a strain rate of 0.01 s^{-1} using UFG Al 5083 (average grain size of 0.7 μm) produced by rapid solidification. The compression specimens measured 8 mm in height and 6 mm in diameter, giving a height-to-diameter ratio of 1.3.

The authors did not indicate whether any lubricant was used during testing. As shown in Figure 2.27, increasing the test temperature led to a reduction in the compression flow curves. The curve at 20 °C exhibits the same work-hardening

behaviour as in Figure 2.26, which contrasts with the softening behaviour observed in Figure 2.25. All other curves obtained at elevated temperatures remained nearly constant beyond the yield point.

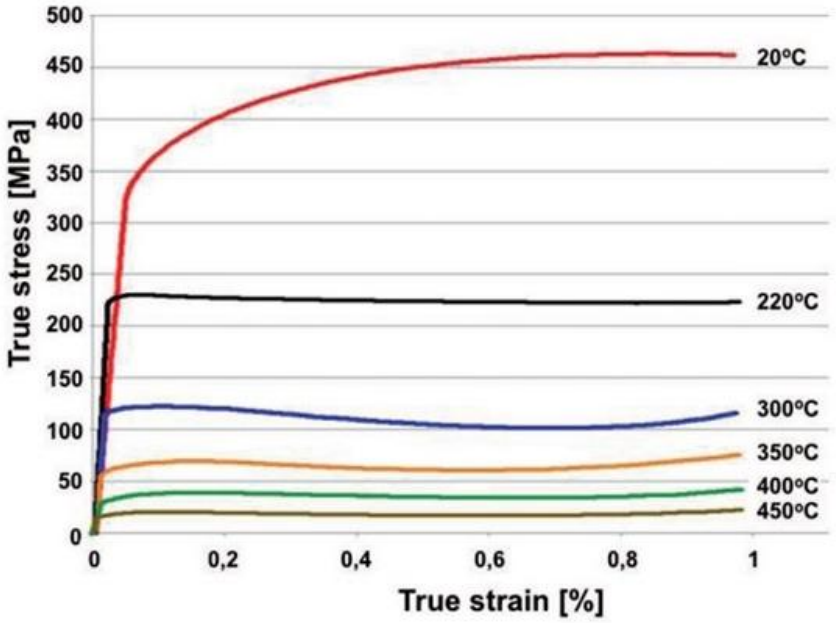

Figure 2.27: True compression stress-strain curves for rapidly solidified Al 5083 at various temperatures (Tokarski et al., 2012).

2.7 Hot Embossing: Process and Microstructural Effects

Hot embossing is one of the processes in microfabrication or replication technology suitable to generate plate microgeometries with high aspect ratios and large surface areas. Hot embossing is performed in three steps, which are embossing, cooling, and demoulding. Embossing refers to the mould filling process, cooling refers to reducing the temperature of both the mould and the embossed material, and demoulding refers to a process that separates the mould from the embossed product.

Hot embossing begins by heating both the embossing material (usually a polymer) and the mould to a set temperature. The material is heated above its softening point, called the glass transition temperature (Tg). The Tg is the temperature at which the material changes its behaviour from glassy to rubbery. Then the mould is pressed into the embossing material by applying an embossing force. Upon completing the mould filling, the embossing force is maintained for sufficient time, while cooling of

the embossed material and the mould takes place. Finally, after reaching a demoulding temperature, the part is separated from the mould.

Referring to Worgull and Heckele (2004), the process parameters for hot embossing are moulding temperature, embossing force, cooling time, demoulding temperature, and demoulding velocity. The stages of the hot embossing process are shown in Figure 2.28.

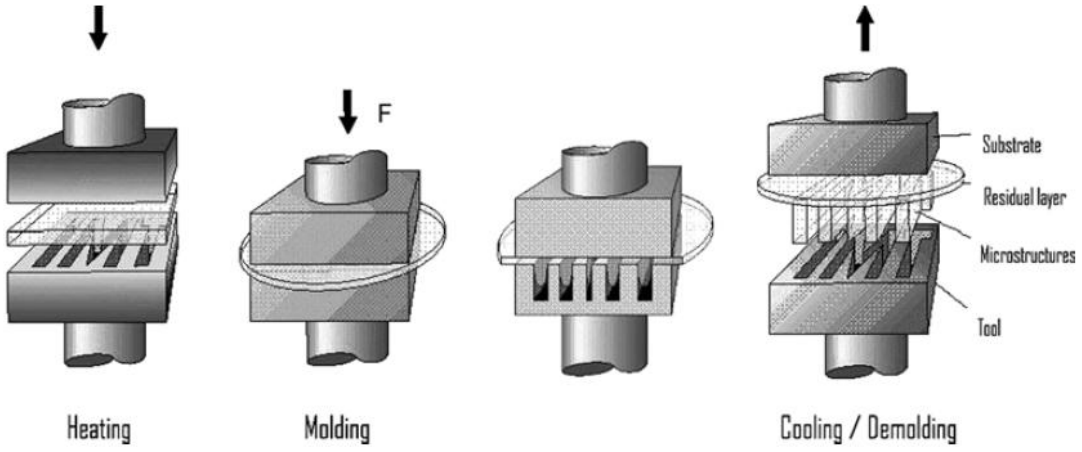

Figure 2.28: Illustration of the hot embossing process (Worgull & Heckele, 2004).

Early research on hot embossing focused primarily on plastic materials, and this method was successful in fabricating high precision, and high quality microstructured parts (Heckele, Bacher, & Müller, 1998). Otto et al. (2000) conducted both cold and hot embossing using the superplastic alloy ZnAl78 and showed that it is a promising technique for manufacturing microparts.

Qiao et al. (2010) performed hot embossing for both CG and UFG Al 1050 to produce micro heat exchangers. The UFG Al 1050 produced by ECAP was used as the embossed material, while silicon served as the mould. ECAP with a die channel angle 90°, conducted at RT up to 12 passes, produced an average grain size of 0.88 μm. Microhardness testing was then performed on UFG Al 1050 to study recrystallisation. Samples subjected to different numbers of passes, were exposed to temperatures ranging from 200 °C to 500 °C for 30 minutes, and the results are shown in Figure 2.29. In general, microhardness decreased as the annealing temperature increased from 200 °C to 350 °C for all numbers of passes. No significant changes in microhardness were observed at temperatures above 350 °C, indicating that recrystallisation was

complete. The selected optimum embossing temperature was 300 °C based on hardness data. At this temperature, recrystallisation was not yet complete and no grain grown occurred.

As shown in Table 2.1, the key process parameters were embossing temperature, maximal force, loading rate, and holding time. The results showed that hot embossing of UFG Al 1050 produced much smoother channels (Figure 2.30) compared with the same process for CG Al 1050 (Figure 2.31). A force of 3 kN was sufficient for full pattern transfer to UFG foil embossed material with a thickness of 1 mm. The better results for UFG Al 1050 are attributed not only to its lower yield strength but also to its fine microstructure, which contributed to the well-formed shape.

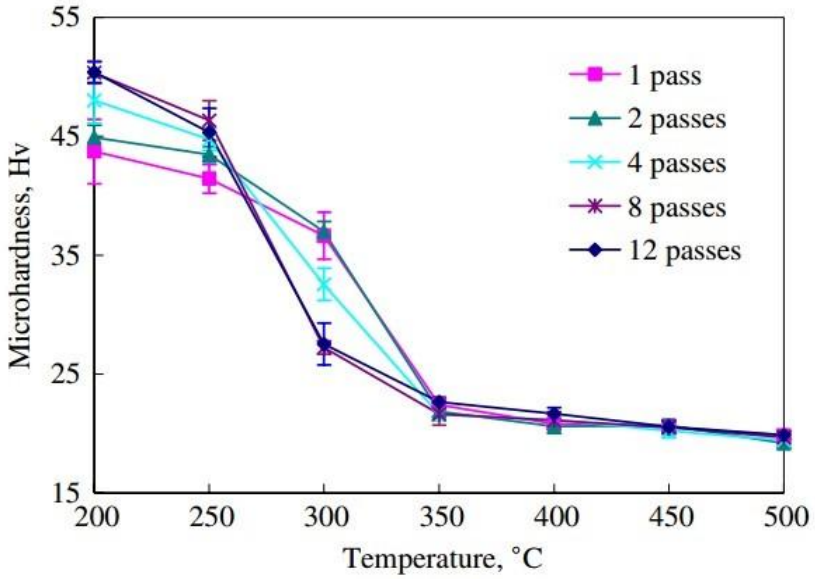

Figure 2.29: Microhardness of UFG Al 1050 at elevated temperature (Qiao et al., 2010).

Table 2.1 : Process parameters for cold and hot embossing of CG and UFG Al 1050 (Qiao et al., 2010).

Process parameters	Hot embossing
Embossing temperature, °C	300
Maximal force, kN	3
Loading rate, N/s	50
Holding time, sec	300

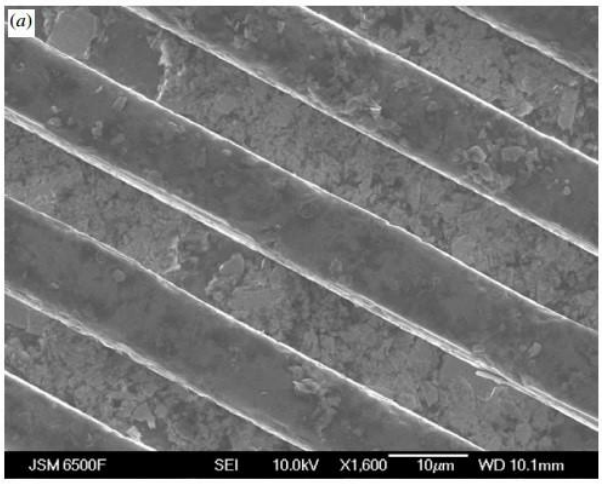

Figure 2.30: Smooth channels produced by hot embossing of UFG Al 1050 (Qiao et al., 2010).

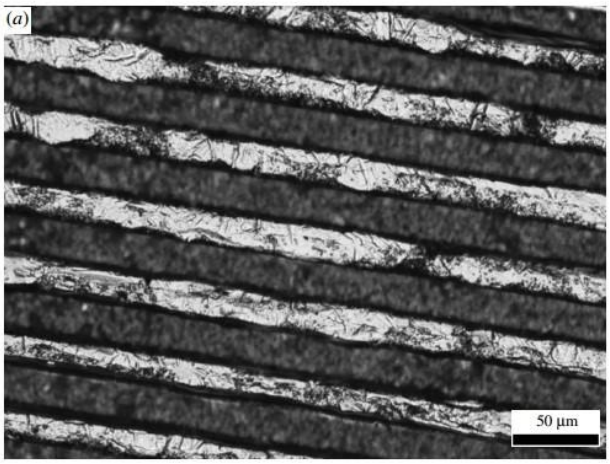

Figure 2.31: Rough channels produced by hot embossing of CG Al 1050 (Qiao et al., 2010).

2.8 Superplastic Forming: Key Principles and Material Requirements

Superplastic forming (SPF) refers to any forming method that takes advantage of material superplasticity (Barnes, 2007). Superplasticity is defined as the ability of a material to undergo large tensile elongation, typically around 500%, compared with conventional materials (Sherby & Wadsworth, 1985).

Metal forming, or simply forming, is generally divided into sheet forming and bulk forming. Sheet forming uses a metal sheet as the workpiece to produce a part, with common processes including bending, deep drawing, and shearing. In contrast, bulk forming processes involve non-sheet or massive workpieces and include rolling, forging, extrusion, and drawing. These processes can be carried out at room or elevated temperatures, depending on the ductility of the material. Figure 2.32 and 2.33 show examples of sheet forming and bulk forming processes, respectively.

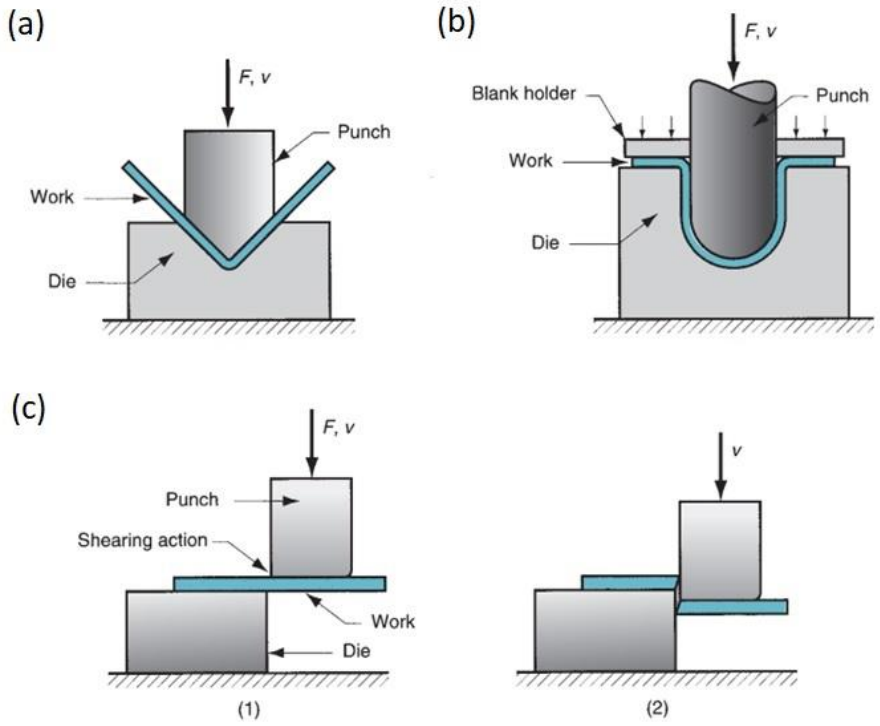

Figure 2.32: Basic sheet forming processes: bending (a), drawing (b), and shearing (c) (Groover, 2020).

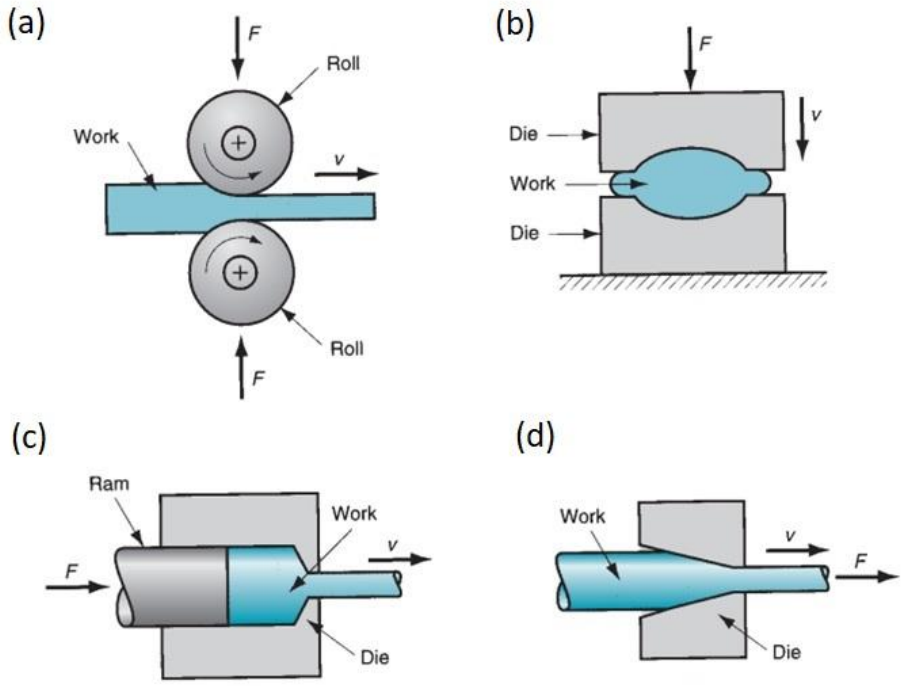

Figure 2.33: Examples of bulk-forming processes: rolling (a), forging (b), extrusion (c), and drawing (d) (Groover, 2020).

There are two basic requirements for successful SPF: the average grain size and the deformation temperature of the material (Langdon, 2009). In general, the smaller the grain size, the easier it is for the grains to rotate and slide over each other, which contributes to larger deformation and superplastic behaviour. The average grain size for a superplastic material is usually less than 10 μm, and the deformation temperature for SPF metals is typically at or above $0.5T_m$, where T_m is the absolute melting temperature. Lowering the deformation temperature can be achieved by reducing the average grain size, as mentioned by Comley (2004). In this work, a similar finished part is achieved using fine-grained Ti-6Al-4V at 775 °C compared with commercial Ti-6Al-4V at 900 °C. The absolute melting temperature for Ti-6Al-4V is around 1660 °C. This approach is known as low-temperature SPF.

According to Langdon (2010), other issues that need to be considered in SPF are strain rate sensitivity, the limited range of useful strain rates, and cavitation, which affects the value of maximum elongation. Strain rate sensitivity depends on both temperature and strain rate. In most cases, a strain rate sensitivity value of around 0.5 is required to achieve maximum elongation. Horita et al. (2000a) reported that the useful strain rate is 3.3×10^{-2} to 3.3×10^{-3} s^{-1}. In this study, UFG Al-Mg-Sc alloys

produced by ECAP were tensile tested at 673 K. A maximum elongation of approximately 2280% was achieved at an initial strain rate of 3.3×10^{-3} s^{-1}. The materials must also have high resistance to grain growth and void formation at elevated temperatures, which are essential characteristics for SPF.

2.9 Backward Micro-Extrusion of Superplastic Materials

In general, there are two types of extrusion, which are forward and backward extrusion. Forward extrusion (Figure 2.34), also known as direct extrusion, is a process where the billet (specimen) material and punch move forward in the same direction. Backward extrusion or indirect extrusion (Figure 2.35), also called reverse extrusion, involves the billet material flowing in the opposite direction to the punch movement.

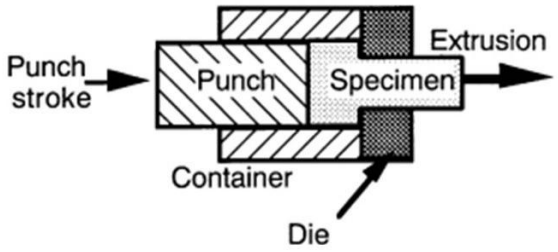

Figure 2.34: Illustration of forward extrusion (Saotome & Iwazaki, 2001).

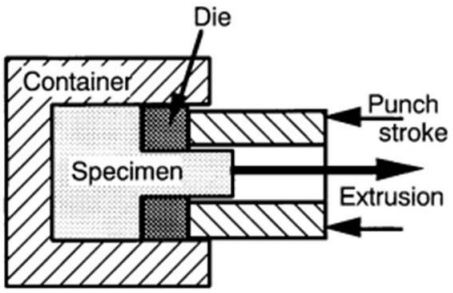

Figure 2.35: Illustration of backward extrusion (Saotome & Iwazaki, 2001).

Generally, extruding a material requires more force if the material is stronger. The required force also depends on factors such as the extrusion ratio, friction between the billet, the container, and the die, as well as process parameters like temperature and extrusion speed. The extrusion ratio, *R*, also called the reduction ratio, is defined as the ratio of the cross-sectional area of the initial billet to that of the final extruded rod. A higher extrusion ratio leads to an increased extrusion force. Compared to forward extrusion, backward extrusion of rods requires a lower force due to reduced friction between the billet surface and the container. Additionally, higher temperatures and lower process speeds decrease the extrusion force.

Saotome and Iwazaki (2001) studied the process of backward micro-extrusion to produce a micro gear shaft under superplastic conditions. In this work, two materials were used: Al-78Zn superplastic alloy and $La_{55}Al_{25}Ni_{20}$ amorphous alloy, both displayed superplastic behaviour. There were three sizes of the shaft, characterised by different gear modules of 10, 20, and 50 μm.

The process parameters, such as the extrusion load, extrusion pressure applied to the punch, working temperature, and working time, are summarised in Table 2.2. The 20 μm module produced a very fine, smooth surface compared with the 10 μm module, as shown in Figure 2.36. This was because extrusion did not occur at a punch stress of 130 MPa for the 10 μm module due to a threshold caused by friction between the punch, the material, and the container. A micro shaft with a 50 μm gear module was successfully produced using the $La_{55}Al_{25}Ni_{20}$ amorphous alloy, as shown in Figure 2.37. This material exhibits Newtonian viscous flow, which means viscosity remains constant, and the amount of deformation depends on the applied pressure. Clearly, 408 N of extrusion load extruded more material than 157 N. This study proved the ability of superplastic backward micro-extrusion to produce fine and smooth microparts.

Table 2.2: Process parameters for superplastic backward micro-extrusion.

Figure	Material	Module, μm	Extrusion load, N	Extrusion pressure, MPa	Working temp, K	Working time, s
Figure 2.36 (a)	Al-78Zn	10	408	130	520	600
Figure 2.36 (b, c)	Al-78Zn	20	176	56	520	600
Figure 2.37 (a)	$La_{55}Al_{25}Ni_{20}$	50	157	50	500	600
Figure 2.37 (b)	$La_{55}Al_{25}Ni_{20}$	50	408	130	500	600

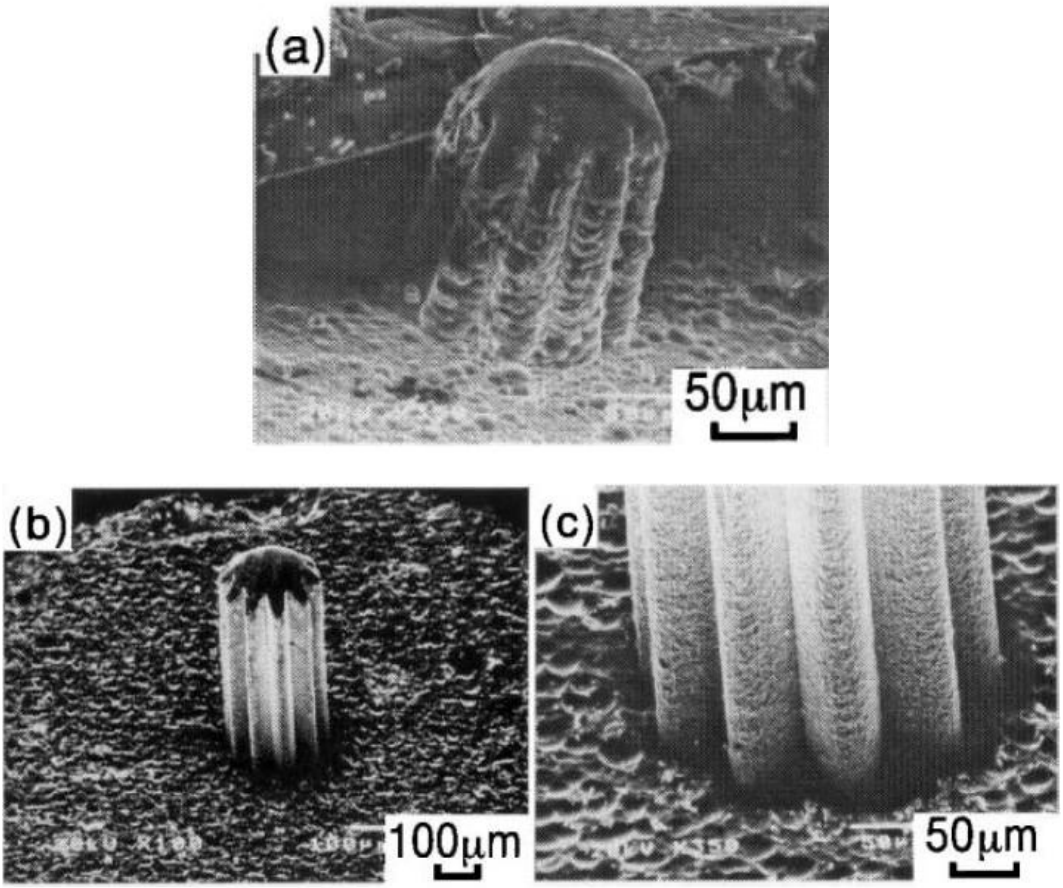

Figure 2.36: Micro gear shafts obtained by backward micro-extrusion using Al-78Zn superplastic alloy with a module of 10 μm (a) and a module of 20 μm (b, c) (Saotome & Iwazaki, 2001).

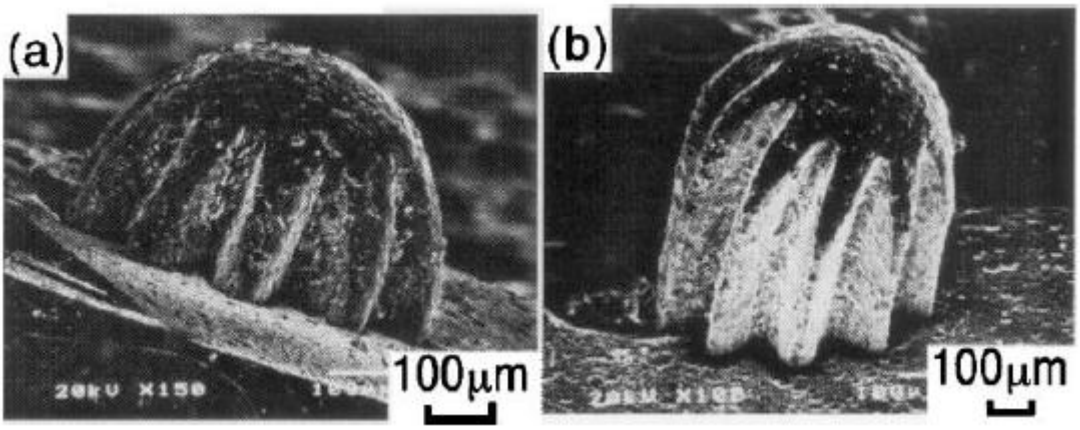

Figure 2.37: Micro gear shaft obtained by backward micro-extrusion using La55Al25Ni20 amorphous alloy with an extrusion load of 157 N (a) and 408 N (b) (Saotome & Iwazaki, 2001).

Geiger et al. (2001) mentioned that the success of microforming is related to the material, process, tools, and machines/equipment. More detailed information related to these four aspects is shown in Figure 2.38.

In terms of material, the grain size is important as it affects the accuracy of the product dimensions. Smaller grain size allows easier material flow during the process and enables better filling of the desired shape. In general, the smaller the specimen size, the lower the required process force. The accuracy of tool fabrication depends on the capabilities of the available manufacturing process, particularly for complex internal shapes. Regarding machines, precise assembly is crucial, and additional equipment such as precision sensors may be required to meet the high machine precision standards.

To study the size effect in microforming, an upsetting (compression) experiment was carried out using a copper alloy (CuZn15) with an average grain size of 79 μm. Both the compression specimens and the tools were scaled down proportionally, referred to as the shrinkage scale factor. Four different shrinkage scales were tested, and the resulting flow curves are shown in Figure 2.39. The results indicated that the size effect causes the flow stress to decrease as the specimen size was reduced.

Geiger et al. (2001) explained in detail the fundamentals of microforming, but there was a lack of work related to processing UFG material and elevated temperature processes. The formability of backward micro-extrusion and material flow compared

to CG and UFG material was not addressed, leaving uncertainties in improving process stability.

Engel and Eckstein (2002) also pointed out a major drawback in the current trend of research, which focuses mainly on microforming of conventional materials at RT. For this reason, they proposed exploring microforming at elevated temperatures using UFG materials, emphasizing the potential benefits of lower process forces and improved formability. Therefore, conducting backward micro-extrusion of UFG material under elevated-temperature conditions could provide a better understanding of the relationship between grain size and process control. This work aims to contribute toward closing this existing knowledge gap.

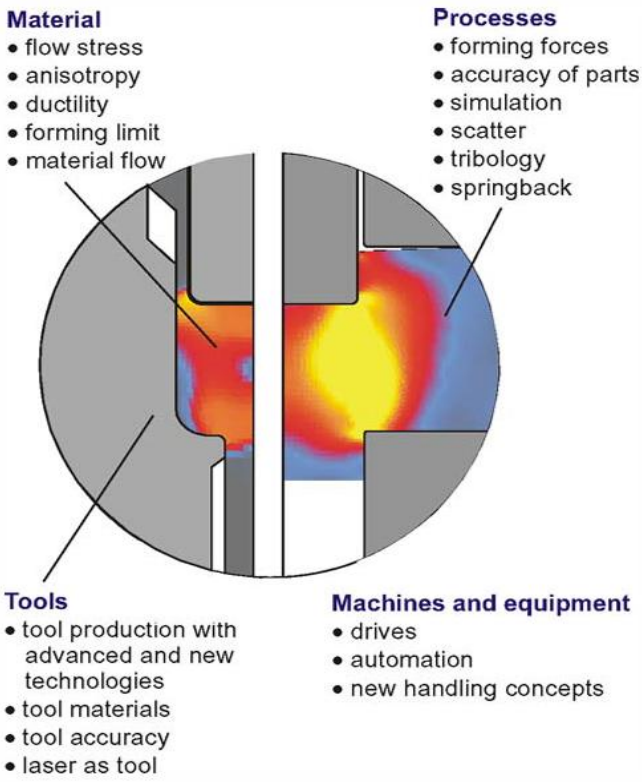

Figure 2.38: Detailed issues in microforming (Geiger et al., 2001).

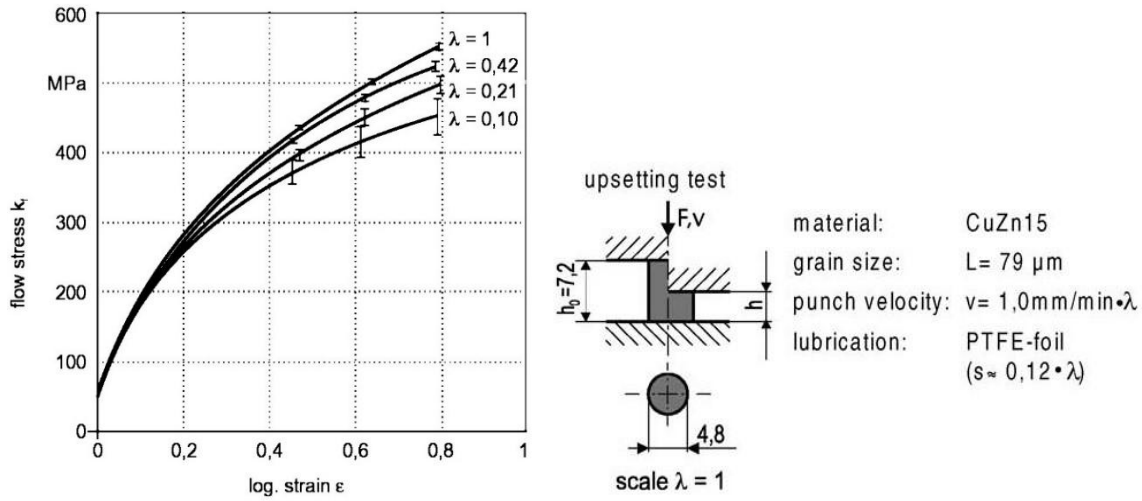

Figure 2.39: Flow curves obtained from compression tests to investigate the size effect in microforming (Geiger et al., 2001).

New exploration directions in microforming include high energy rate forming (HERF) (Sharma et al., 2022) and impact micro-forming (Zhu et al., 2025). HERF is a broad category that includes many high-energy techniques such as explosive forming, electromagnetic forming, and laser shock forming. In contrast, impact micro-forming is a more specific method that involves high-strain-rate deformation applied to micro-scale materials. Examples of these techniques include laser shock forming, electromagnetic forming, water-jet forming, electrohydraulic forming, and impact hydroforming. All these approaches aim to overcome size-effect issues and significantly improve material formability.

Another growing research area in microforming is tribology, which focuses on friction, wear, and lubrication, particularly in relation to the tool conditions during forming. Raja and Ramesh (2021) highlighted the effectiveness of tool surface engineering and coatings in reducing friction. Similarly, Funazuka et al. (2025) demonstrated that nano-textured punch and die surfaces can improve tribological performance by lowering the forming load and reducing material sticking.

Overall, these two areas are now leading the direction of microforming research.

2.10 Current Limitations and Knowledge Gaps

It is well established that increasing the number of ECAP passes significantly reduces grain size, thus improving the material properties. However, it remains unclear whether additional passes lead to further grain size reduction or eventually stabilise at a certain level. A clearer understanding of the relationship between the number of ECAP passes and grain size reduction is therefore required.

Most existing microforming research has concentrated on CG materials rather than UFG materials. As a result, the formability, flow behaviour, and process stability of UFG materials in microforming are not fully understood. This gap creates uncertainty about the true benefits of grain refinement material for microforming processes.

Another constraint is the lack of research on microforming at elevated temperatures. These conditions are expected to improve formability and offer several potential benefits, such as lowering process forces that contribute to longer tool life.

Therefore, addressing these research gaps is essential not only for a better understanding but also for the successful implementation of elevated temperature microforming with UFG materials.

2.11 Summary

This chapter presents a literature review relevant to the topic of this thesis. The focus of this research is on material and micromanufacturing in the production of miniature conical pins. It has been well established that materials with grain sizes down to the UFG level demonstrate significant improvements in micromanufacturing, both in terms of product quality and reduction in processing load at elevated temperatures.

There were two approaches that were presented to fabricate UFG materials through grain refinement, which are bottom-up and top-down techniques. Powder metallurgy, electrodeposition, and rapid solidification were categorised under bottom-up, whereas top-down refers to any large plastic strain deformation known as SPD. The details of SPD are discussed and categorised into batch and continuous. Among the batch of SPD processes, ECAP was selected as a process to produce UFG in this work, later referred to as I-ECAP.

The process parameters for ECAP are temperature, die channel angle, processing route, and number of passes. For Al 5083, the optimal process temperature is 200 °C, while temperatures above this level can cause grain growth. Among the route options, B_C produces more homogeneous microstructures. Furthermore, it has been demonstrated that increasing the number of ECAP passes leads to a refinement of grain size and an increase in the fraction of HAGB.

Based on the review of micromanufacturing processes: hot embossing, superplastic forming, and backward micro-extrusion, the processing temperature and working time are the two most important parameters for achieving high-quality products.

Overall, this review provides a better understanding of how processing conditions affect material properties, the final microstructure, and the finished product. The following experiments in this work will be guided by this knowledge.

CHAPTER 3
EXPERIMENTAL PROCEDURES FOR PRODUCING UFG MATERIALS USING I-ECAP

3.1 Introduction

This chapter explains the experimental procedure to produce UFG billets using the double-billet I-ECAP process. In this approach, square billets are positioned in the die channel, moved up into the deformation zone by a screw jack, and subjected to punch oscillations to impose severe plastic deformation. The description further covers the I-ECAP rig configuration, process operation, heating and control system, as well as the preparation and lubrication of billets.

This research seeks to investigate how the double-billet I-ECAP process influences the refinement of grain structures in aluminium billets. This study focuses on route B_C, stepwise lubrication, and a processing temperature of 200 °C. It also examines how the number of four and eight passes affects the formation of a UFG microstructure.

The novelty of this work lies in comparing four and eight I-ECAP passes to produce uniform microstructures of UFG billets.

Although I-ECAP is widely used for grain refinement, there is limited understanding of how double-billet with route B_C, stepwise lubrication, and processing at elevated temperatures affect microstructural evolution at different pass numbers. This study addresses this gap to establish optimised process parameters for producing high-quality UFG billets for microforming applications.

3.2 Double-billet I-ECAP Process

I-ECAP is one of the SPD technique developed by Rosochowski and Olejnik (2007a). Unlike the classical ECAP process, I-ECAP separates the feeding and deformation stages, allowing more efficient control of material during the process (Rosochowski et al., 2008). In the present study, the I-ECAP process was applied using a double-billet configuration, where two billets were simultaneously processed inside the die channel, as illustrated in Figure 3.1.

The stationary dies (A) define as the input channel, punch (C) moves in a reciprocating motion, while *a* defined as feeding step. Using two billets side by side gives better stability, reduces the change of misalignment inside the die, and helps achieve more uniform deformation.

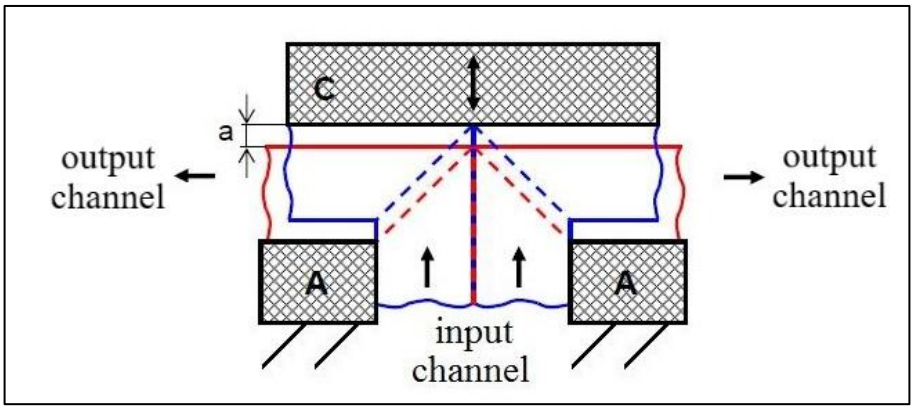

Figure 3.1: Principle of the double-billet I-ECAP process (Rosochowski et al., 2008).

During operation, the reciprocating punch (C) deforms both billets against the stationary die (A). The billets are inserted from the top of the input channel and incrementally fed upward by a screw jack located at the bottom of the rig, as shown in Figure 3.2. The screw jack feeds the billets upward by a step distance of *a*. When the feeding stops, the punch moves downward and plastically deforms the billets along the shear plane. This cycle of feeding and deformation is repeated continuously until the billets exit the output channel.

Figure 3.2: Two billets placed into the die channel before the I-ECAP process.

Rosochowski and Olejnik (2011) reported that billets processed by I-ECAP reached an equivalent plastic strain of about 1.15 per pass. Oh and Kang (2003) found similar values, in the range of 0.5 to 1.4, based on DEFORM simulations.

Numerous studies have demonstrated that I-ECAP succeeds in enhancing material characteristics and refining the microstructure. For instance, Olejnik et al. (2008) reported that after eight passes, I-ECAP produced an average grain size of less than 500 nm in Al 1070 plate. Similarly, Gzyl et al. (2014b) demonstrated that processing AZ31B magnesium alloy by I-ECAP at 250 °C refined its microstructure to an average grain size of about 5 μm after four passes, while also improving its mechanical properties by enhancing both strength and ductility.

Theoretically, I-ECAP can process infinite-length bars, plates, or sheets with low friction during feeding, which reduces the feeding force.

3.3 I-ECAP Rig

A 100-ton servo-controlled hydraulic press was used to operate the I-ECAP rig as shown in Figure 3.3. This press is located at the Advanced Forming Research Centre (AFRC), Inchinnan, Glasgow. The rig mounted on the press consisted of two main subsystems: a feeding system powered by a screw jack, and a deformation system actuated by a reciprocating punch.

Figure 3.3: I-ECAP rig on the 100-ton hydraulic press.

3.3.1 Punch and Die Alignment

Prior to starting the experiment, the punch and die slot must be accurately aligned for double-billet I-ECAP processing to work smoothly. Figure 3.4 shows that a precision gauge block was used to check the punch alignment with the die walls. To ensure the punch is centred between the two billets, the clearance on both outer punches must be equal (X = X). This alignment step was crucial to avoid tool wear and to deform both billets uniformly.

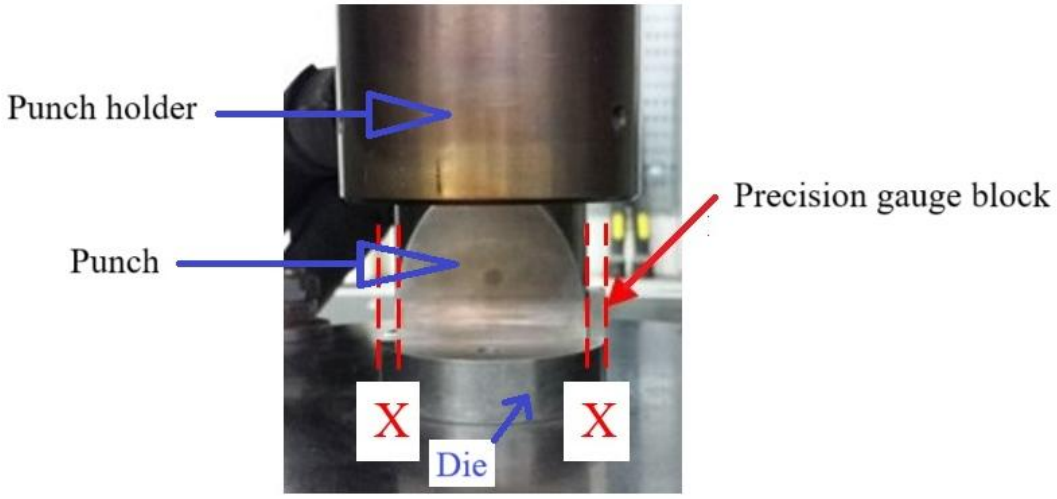

Figure 3.4: Alignment of punch and die slot with a precision gauge block.

3.3.2 Heating and Temperature Control Setup for I-ECAP

During I-ECAP processing, the billets were heated to the appropriate forming temperature using electric heating. Both the die and the punch had heating and cooling components to guarantee consistent processing conditions. The temperature controller (TC) was used to monitor and control the temperature for the die and the punch.

Figure 3.5 shows the heating elements at three different areas, namely a band heater on the die pre-stressing ring (1), aluminium blocks with inserted heating rods on top of the die (2), and a small band heater around the punch holder (3), as well as a cooling system for the LC1. The heating power for heaters (1), (2), and (3) was 3000 W, 1500 W, and 600 W, respectively.

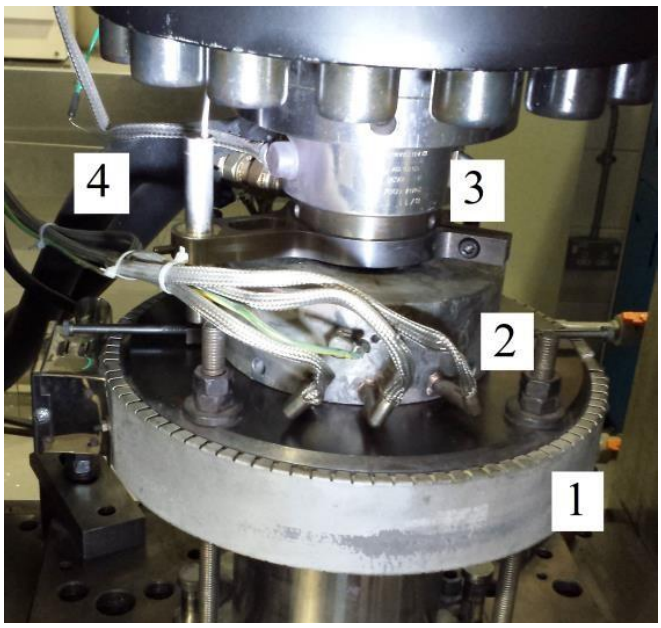

Figure 3.5: Heating/cooling elements for I-ECAP.

3.3.3 I-ECAP Control System

Figure 3.6 shows the schematic of the control system for this press, which consists of two computers to control the process using Cubus software and LabView software, developed by Zwick Testing Machines Ltd and National Instrument (NI), respectively. These two software platforms are integrated into the press's control system. The Cubus software (Zwick Testing Machines Ltd), regulates the punch's (P) reciprocating action. While LabView software (National Instruments) synchronises the punch cycle and the screw jack's (SJ) feeding motion.

To quantify the punch force and the feeding force applied by the screw jack, two load cells were fitted in the system: LC1 and LC2. Two linear variable differential transformers (LVDTs) were used to detect displacement. While LVDT2 sensed the exact location of the punch, LVDT1 monitored the hydraulic actuator's piston movement. Elastic deflections and gap close in the press and rig structure caused these readings to vary somewhat, but taken as a whole, they guaranteed precise process control.

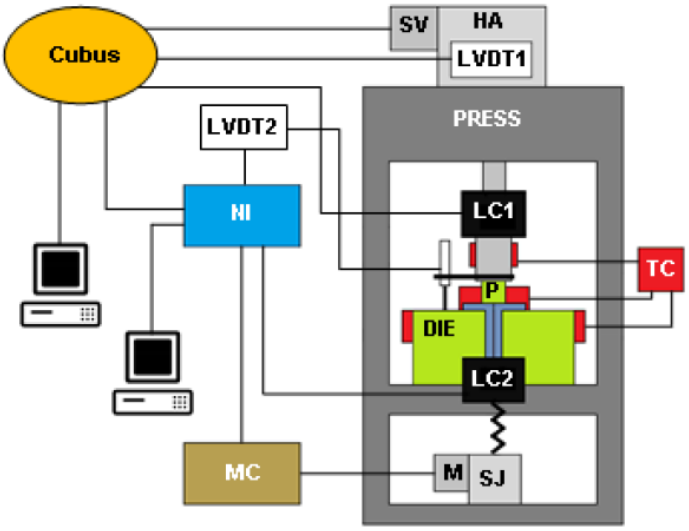

HA	Hydraulic Actuator
SV	Servo Valve
LVDT	Displacement Transducer
NI	National Instruments Modules
MC	Motor Controller
M	Electric Motor
SJ	Screw Jack
LC	Load Cell
P	Punch
TC	Temperature Controller

Figure 3.6: Schematic of the control system for I-ECAP (Gzyl, 2014a).

3.3.4 I-ECAP Process Setup and Operation Procedure

The process parameters for the I-ECAP double-billet experiment are shown in Table 3.1. These parameters are the die channel angle at 90°, the temperature settings for the die and punch, the feeding stroke of the screw jack, and the punch oscillation conditions (frequency and amplitude). The overall processing temperature was set at 200 °C; therefore, the die was heated to 200 °C, while the punch was maintained at 300 °C to maintain a consistent billet temperature during processing. The billets were deformed following route B_C, in which the billet was rotated 90° between successive passes.

The input values of punch oscillation and feeding stroke per cycle were selected based on preliminary work to ensure no damage occurred to the billets. The parameters were defined as follows: punch amplitude = 0.8 mm (1.6 mm peak to peak), punch frequency = 0.5 Hz, and feeding stroke per cycle = 0.2 mm (Salamati et al., 2016). The process of I-ECAP is illustrated schematically in Figure 3.7, showing punch oscillation and screw jack displacement.

Table 3.1: Process parameters for the double-billet I-ECAP experiment.

Parameters	Value
Die channel angle, °	90
Die temperature, °C	200
Punch temperature, °C	300
Route	B_C
Screw jack feeding stroke, mm	0.2
Punch frequency, Hz	0.5
Punch amplitude, mm	0.8

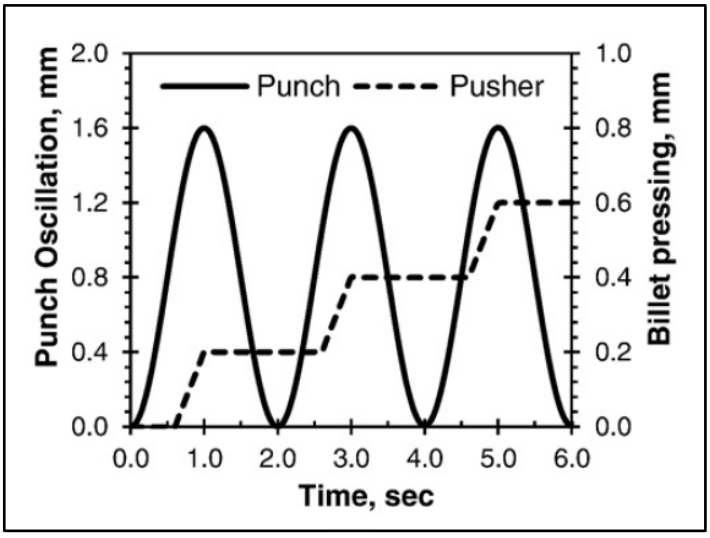

Figure 3.7: An illustrate movement of punch and screw jack (Pusher) during I-ECAP process (Qarni et al., 2017).

There were three preparatory steps before the I-ECAP process could be carried out. First, a zero-reference position for the punch was established. Second, the sine wave values for the punch oscillation were set. Finally, the feeding step displacement for the screw jack was adjusted. The detailed procedure for each step is described below.

1. Setting a zero-reference position for the punch

i. Lower the punch until it contacts the stopper block positioned at the input die channel and stop when the punch force reading reaches approximately -1 kN (Figure 3.8).

ii. Assign a zero value to the displacement transducer LVDT1 (Figure 3.9).

iii. Raise the punch to a specific value (in this case, 0.8 mm) to define the reference position for the sine wave.

iv. Repeat step (ii) by setting a new zero reference on the displacement transducer.

v. Remove the stopper block.

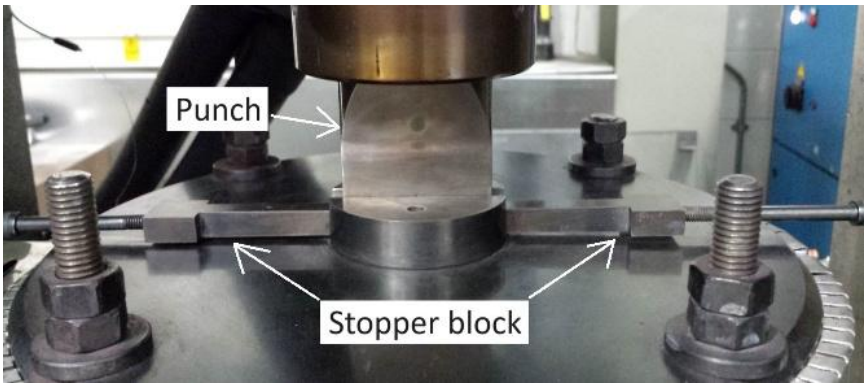

Figure 3.8: Location of the stopper block.

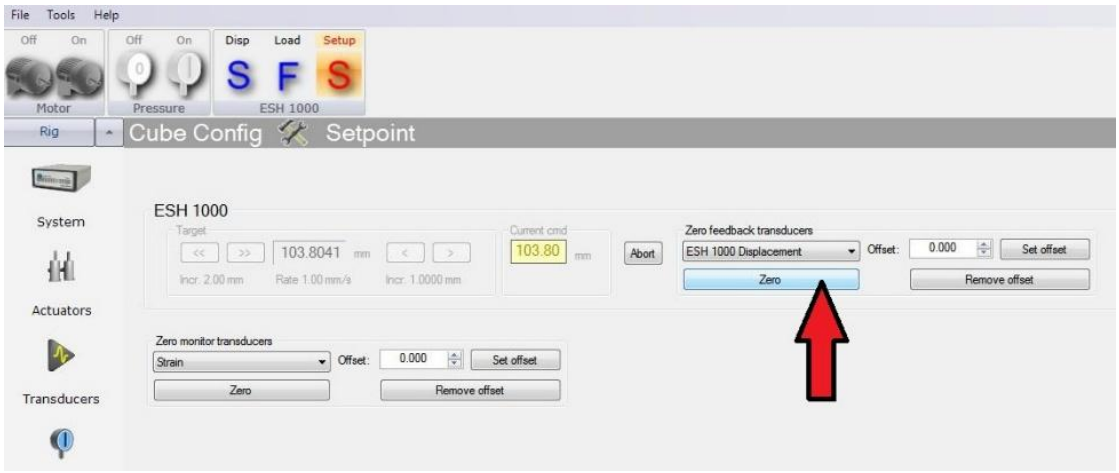

Figure 3.9: Cubus software interface for zeroing the displacement transducer.

2. Setting the sine wave value for the punch

i. There are two methods to determine the punch amplitude value: using the amplitude/mean setting or the upper/lower setting. In this study, the amplitude/mean setting was used, with an amplitude of 0.8 mm (1.6 mm peak-to-peak), while the punch oscillation frequency was set to 0.5 Hz, as shown in Figure 3.10.

ii. After setting the amplitude and frequency values, the Start button was selected to initiate the sinusoidal movement of the punch (Figure 3.10).

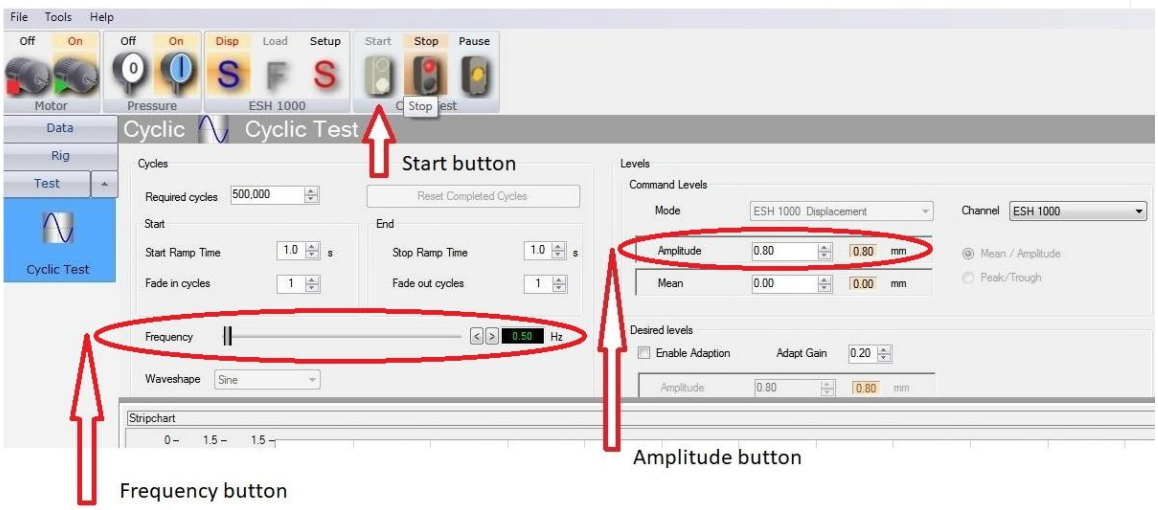

Figure 3.10: Cubus software interface showing controls for punch oscillation (start, amplitude, and frequency).

3. Feeding step displacement setup for the screw jack

i. The feeding step displacement for the screw jack was set to 0.2 mm (Figure 3.11) by adjusting the trigger positions that controlled the screw jack motor-green dotted line for switch-on and red dotted line for switch-off.

ii. A maximum feeding force limit was defined to prevent potential damage to the screw jack during operation.

iii. Once the billets had been inserted into the die and stabilised at the processing temperature (approximately 15 minutes), the Start Acquisition button was pressed to begin recording the I-ECAP experiment.

iv. Immediately afterwards, the Start Synchronisation button was activated to initiate the billet feeding.

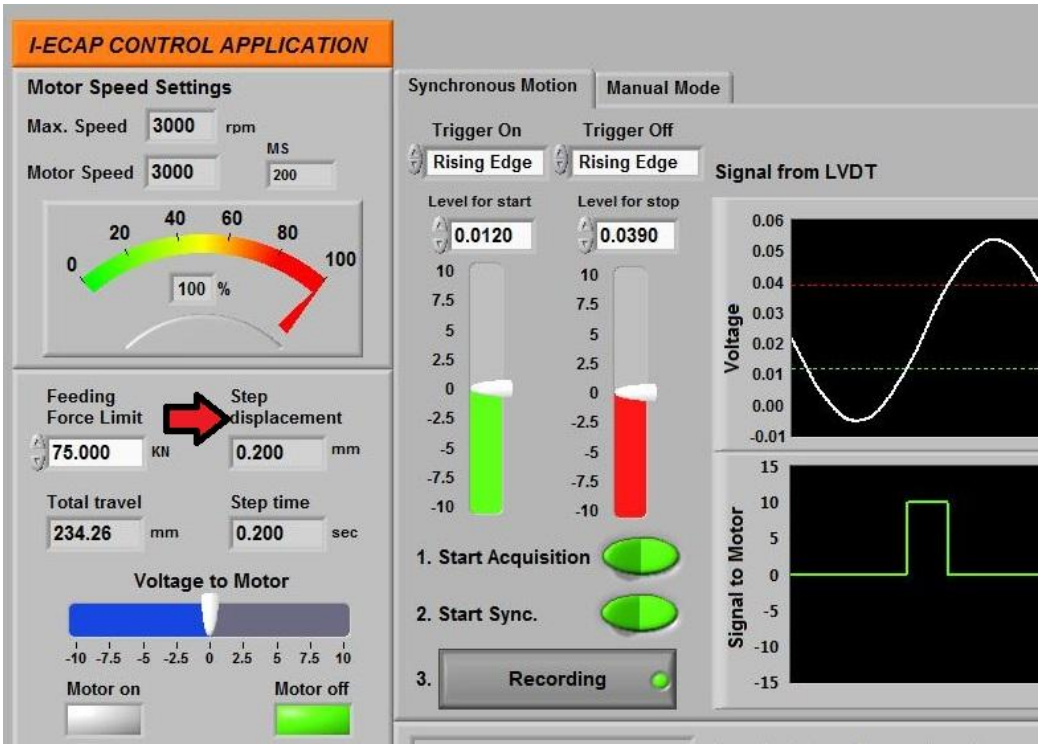

Figure 3.11: LabView interface for configuring screw jack feeding step displacement in the I-ECAP process.

During the I-ECAP process, the input command values and the actual feedback for step displacement and punch load were continuously monitored using the Cubus interface, as shown in Figure 3.12.

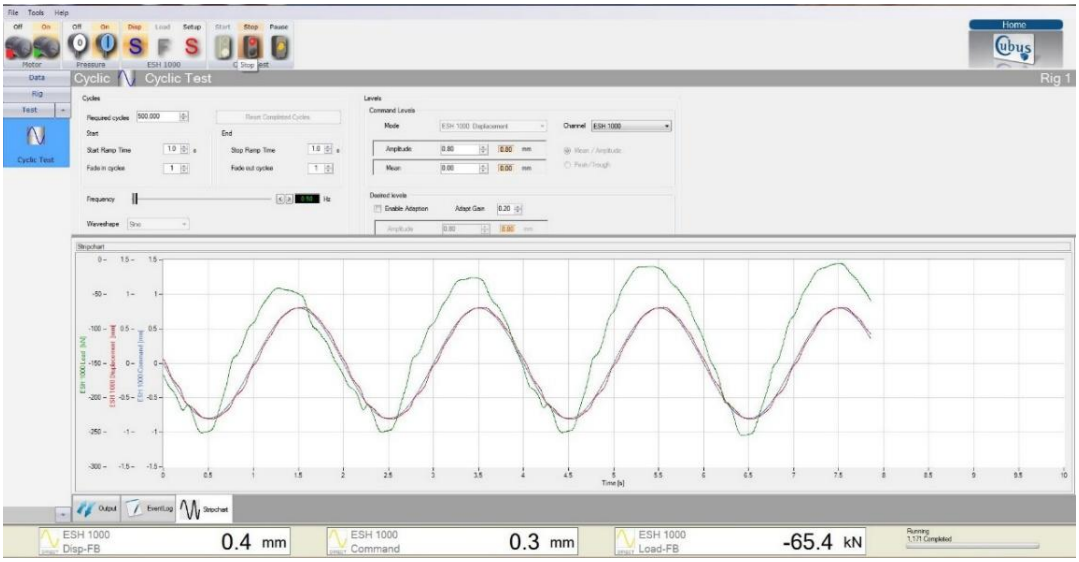

Figure 3.12: Cubus interface for monitoring step displacement and punch load in the I-ECAP process.

3.4 Billet Preparation and Lubrication

Al 5083 is one of the commercial materials with excellent resistance to corrosion, good ductility, and a medium strength level that makes it suitable for formability. It is well known for its low density and excellent thermal conductivity, as well as being one of the Al alloys with low temperature superplasticity. This alloy has been extensively used in many industries, such as automotive, marine, and chemicals. Because of its non-heat-treatable characteristic, deformation at elevated temperatures has no significant effect on its mechanical properties. For these reasons, Al 5083 was selected in this study for I-ECAP and backward micro-extrusion experiments at elevated temperatures.

Aluminium alloys are divided into two major categories: wrought compositions and cast compositions. Wrought aluminium alloys are generally divided into two principal groups: heat-treatable (precipitation-hardenable) alloys (2XXX, 6XXX, 7XXX, and some of the 8XXX) and non-heat-treatable alloys (1XXX, 3XXX, 4XXX, and 5XXX series). Solution heat treatment, quenching, precipitation, or age hardening can alter the material properties of heat-treatable alloys, whereas the material properties of non-heat-treatable alloys can only be changed by strain hardening. In the standard temper designation system for aluminium, the letter ‘T’ is assigned to heat-treatable alloys, while non-heat-treatable alloys are designated as O-annealed (soft temper), F-as fabricated (no specific temper), and H-strain hardened. Aluminium alloys in the strain-hardened state can be specified as H1y-strain hardened only, H2y-strain hardened followed by partial annealing, H3y-strain hardened and stabilised, and H4y-strain hardened and lacquered or painted (Hirsch, 2011). Some basic temper codes for the strain-hardened state are shown in Table 3.2.

Table 3.2: Temper H-codes for strain hardened aluminium alloys (Benedyk, 2010).

Temper code	Description
H12	Work hardened by rolling to quarter hard
H112	Slightly strain hardened from hot working or from limited cold work
H116	Specially fabricated, controlled strain, corrosion resistance
H22	Work hardened by rolling then annealed to quarter hard
H32	Work hardened by rolling then stabilised by low-temperature heat treatment to quarter hard
H323	A version of H32 to provide acceptable resistance to stress corrosion cracking
H42	Strain hardened and lacquered or painted with remaining strain hardening at quarter hard

Casting aluminium alloys are described using a three-digit system followed by a decimal value. For instance, heat-treatable alloys include Al–Cu (210–206), while non-heat-treatable alloys include Al-Mg (513, 515, 518). The 2XX, 3XX, and 7XX series fall under the category of heat-treatable casting alloys. In the International Alloy Designation System, the 5000 series aluminium alloys are mainly alloyed with magnesium. The typical chemical composition and mechanical properties of Al 5083 are shown in Table 3.3 and Table 3.4, respectively. Al 5083 is commonly available in bar, flat-rolled plate, and sheet forms.

In this study, a commercial cold-rolled Al 5083 plate with a thickness of 10 mm was used as the starting material, as shown in Figure 3.13. The billets were processed without any annealing treatment either before or after the I-ECAP process.

Table 3.3: Typical chemical composition of Al 5083 alloy according to ASTM B221M (in weight percent, wt. %).

Element	Composition (wt. %)
Magnesium (Mg)	4.00 - 4.90
Iron (Fe)	≤ 0.40
Copper (Cu)	≤ 0.10
Manganese (Mn)	0.40 - 1.00
Silicon (Si)	≤ 0.40
Chromium (Cr)	0.05 - 0.25
Zinc (Zn)	≤ 0.25
Aluminium (Al)	Balance

Table 3.4: Mechanical properties of Al 5083-H22/H32 plate (thickness 6-12.5 mm) (www.en.investa.pl).

Property	Value
Ultimate tensile strength (MPa)	min. 305 – max. 380
0.2% Yield strength (MPa)	≥ 215
Vickers hardness, HV	~ 104
Elongation at fracture, A50 (%)	≥ 10

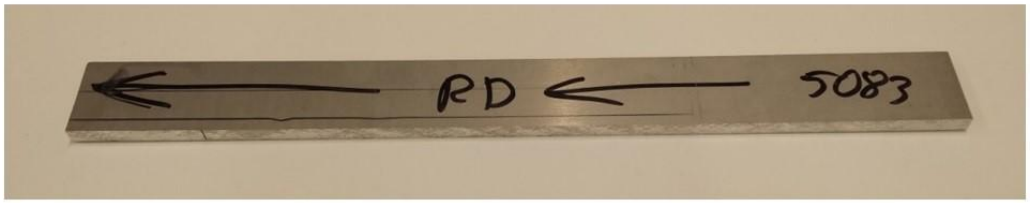

Figure 3.13: Commercial Al 5083 plate (50×10×5 mm^3) used as raw material.

The geometry of billet for I-ECAP is shown in Figure 3.14. The geometry of the billet is a 10×10 mm^2 square cross-section and 115 mm in length, cut using wire electric discharge machining parallel to the rolling direction. At the top edge of the billet, around 1 mm of chamfer was machined to facilitate the material flow in the early process of I-ECAP.

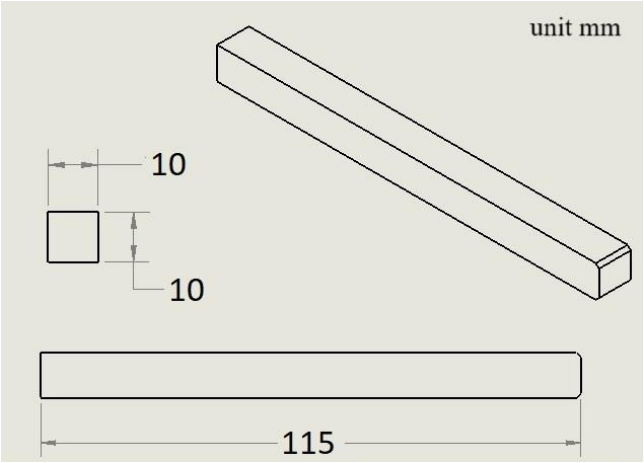

Figure 3.14: The geometry of billet for I-ECAP.

Figure 3.15 shows the difference between the billet before and after the first pass of I-ECAP. During processing, the billet is compressed inside the die, which typically causes its width to increase by 5%–7% after I-ECAP.

To restore the billet dimensions required for subsequent passes, material removal can be carried out either by grinding or milling. In this study, a grinder-polisher machine, as shown in Figure 3.16, was used for this purpose. Additionally, the processed billet exhibited slight buckling; hence, a straightening operation was performed by bending the billet between two flat surface plates.

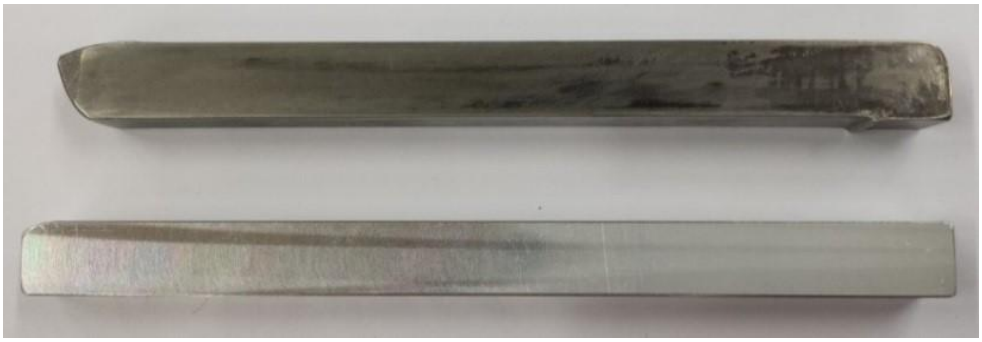

Figure 3.15: Billet before I-ECAP, after machining and before conversion coating (bottom), and after one pass of I-ECAP (top).

Figure 3.16: Grinder-polisher machine.

Figure 3.17 shows the billet before I-ECAP, after four passes (4P), and after eight passes (8P) of I-ECAP. The length reductions were approximately 20% after 4P and 40% after 8P. This reduction resulted from partially cutting the billets ends and side grinding after each pass to prepare it for subsequent passes.

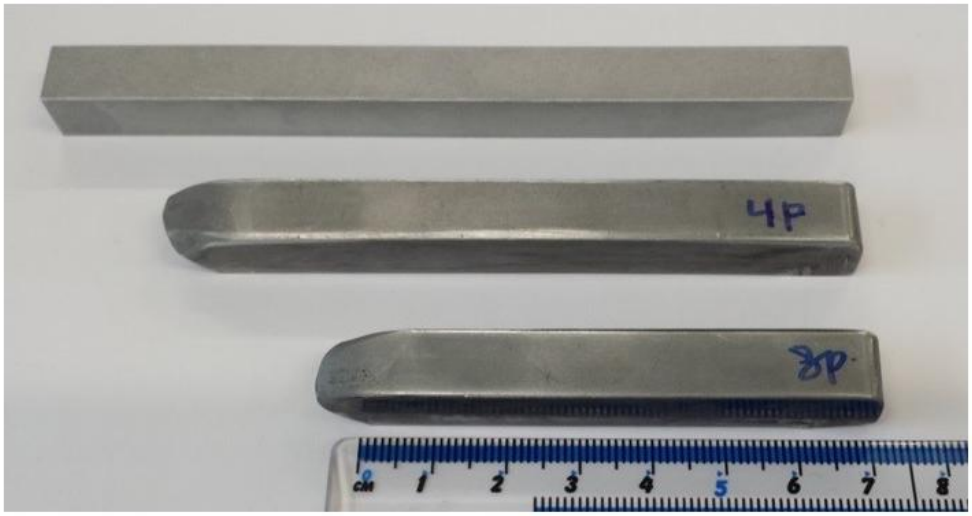

Figure 3.17: Billet before I-ECAP (top), after four passes (middle), and after eight passes (bottom).

Before the I-ECAP process, the billets were initially conversion coated to create a layer of calcium aluminate, as shown in Figure 3.18. Conversion coating is a process where a metal is immersed into a chemical solution with the application of electric current that turns the surface into a porous layer. This process was conducted at the Institute of Manufacturing Processes, Warsaw University of Technology, Poland. The purpose of this porous layer is to create better bonding with lubricants applied to the billet's surface.

The billets were sprayed with Everlube Products' Formkote T-50, a solid film lubricant, after conversion coating. This lubricant is suitable for hot forming at temperatures up to 816 °C. Once the Formkote layer dried, the billets were coated with molybdenum disulfide (grey oil-based plate, Rocol dry moly paste) before being placed into the die channel.

For subsequent passes after the first I-ECAP cycle, the billets were no longer re-exposed to the conversion coating. Instead, as shown in Figure 3.19, they were sandblasted to create a uniformly rough surface, then sprayed with Formkote before being finished with molybdenum disulfide, as shown in Figure 3.20.

Sandblasting was performed to improve the bonding strength of the Formkote. This step-by-step lubrication technique was important to reduce friction, extend tool life, and ensure stable billet flow throughout the I-ECAP process.

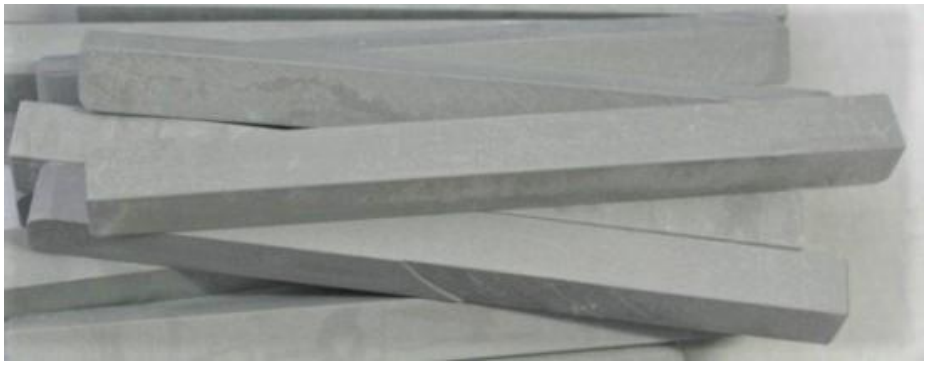

Figure 3.18: Billets after conversion coating (calcium aluminate layer).

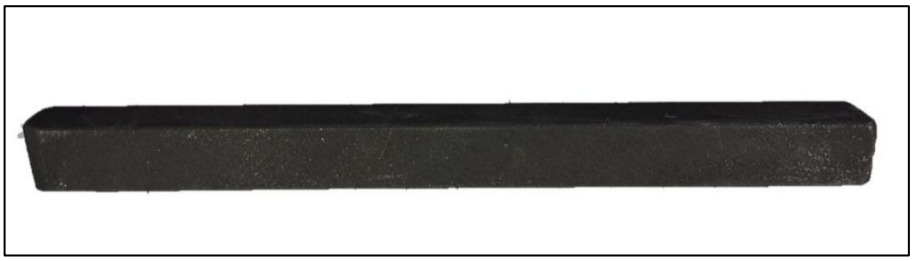

Figure 3.19: Billet after sandblasting and Formkote spraying for subsequent I-ECAP passes.

Figure 3.20: Billets after final lubrication with molybdenum disulfide before I-ECAP.

3.5 Summary

The experimental method of the I-ECAP process for making UFG billets has been described in this chapter. The design of the rig, control system, heating arrangement, billet preparation, lubrication, and processing steps were described in detail. The focus of I-ECAP is on double-billet, whereas the process was conducted on Al 5083 at a working temperature of 200 °C, using route B_C and a die channel angle of 90°.

I-ECAP successfully produced UFG billets up to eight passes without any cracks. After eight passes, there was an overall length reduction of almost 40%. The robustness of the technique was demonstrated by the fact that the Al 5083 billets were not subjected to annealing either before or after I-ECAP in this study.

The contributions to this work are:

1. **Novel Process Design** - The double-billet I-ECAP method is more efficient, produces less waste, and improves billet stability compared to traditional single billet ECAP. It succeeds in producing UFG billets for later microforming, with more uniform deformation and larger billet size and geometry.

2. **Billet Preparation and Lubrication -** A new systematic billet preparation and lubrication technique is introduced, using conversion coating, sandblasting, and step-by-step lubrication with Formkote and molybdenum disulfide. This method keeps the I-ECAP process more stable by ensuring lower friction and minimising tool wear.
3. **Experimental Validation -** Cubus software is able to monitor real-time data on the input and actual for punch load and displacement during the I-ECAP process. It helps to understand the real situation during the process of producing UFG billets.

CHAPTER 4
MICROSTRUCTURAL AND MECHANICAL CHARACTERISATION OF CG, 4P, AND 8P AL 5083 BILLETS

4.1 Introduction

As discussed earlier, the microstructure of metals plays an important role in microforming at RT as well as elevated temperatures. Therefore, microstructural characteristics such as grain size and grain boundary misorientation were examined for the CG, 4P, and 8P billets. The mechanical properties of each type of billet were studied by tensile, compression, and microhardness testing. To characterise the material from an engineering point of view, the tensile test was performed only at RT.

As the backward micro-extrusion process is compression-dominated, the compression test was performed at RT and elevated temperatures under different constant strain rates. The test was conducted to investigate the dependency of the material's properties on temperature and strain rate. Hereafter, these results will be used in the material model for finite element simulation.

The novelty of this study lies in correlating the microstructure obtained after 4P and 8P I-ECAP passes with the resulting mechanical properties. This provides new insight into how the number of passes enhances mechanical properties in microforming applications, an aspect often overlooked in previous studies.

4.2 Microstructure Characterisation

There are many types of microscopes used to capture images of grain sizes, namely light microscopy, SEM, and TEM. Each of these instruments has a resolution limit of approximately 200 nm, 1 nm, and 0.25 nm, respectively. Electron backscatter diffraction (EBSD) is a computer-assisted technique used to measure average grain size, grain boundary misorientation angles, and texture based on SEM results.

The microstructural study was performed at the Institute of Non-Ferrous Metals in Skawina, Poland. EBSD was carried out using a high-resolution SEM (Inspect F50) equipped with EDAX-TSL software (Figure 4.1). The samples for SEM were prepared by grinding with sandpaper (finishing with 5000 grade), polishing with diamond paste down to 0.5 μm, and ion beam milling that was conducted using a Leica EM RES101 (Figure 4.2). During the SEM process, the sample was tilted 70° from the horizontal plane at a 20 kV accelerating voltage and 200 mA beam current. The samples were tested to obtain information regarding the distribution of grain size and grain boundary misorientation angle. The overall process, including sample preparation, equipment operation, and software analysis of the microstructures, was led and supervised by Dr. Sonia Boczkal, an assistant professor at the Institute of Non-Ferrous Metals.

Figure 4.1: High-resolution SEM (Inspect F50) used for EBSD analysis.

Figure 4.2: Leica EM RES 101 ion beam milling system for SEM sample preparation.

4.2.1 EBSD Analysis Procedure

All specimens for microstructural analysis were cut along the transverse direction on the X-plane, close to the central area, as shown in Figure 4.3. The Orientation Imaging Microscopy (OIM) analysis software by EDAX-TSL produced orientation maps of the microstructures, histograms of grain size, and misorientation distribution graphs. The software applied the standard procedure for map cleaning and used an appropriate step size of 0.3 μm for the unprocessed material (CG) and 0.05 μm for the processed material (4P and 8P). The purpose of map cleaning is to remove pixels with poor image quality that could cause incorrect indexing.

The step size refers to the spacing between measurement points and the size of the grid (both horizontally and vertically), representing the ratio of the average grain size to the selected step size. According to EDAX-TSL, a 10:1 ratio between the total number of grains measured and the number of points per grain ensures an optimal balance. This ratio provides sufficient spatial resolution to capture microstructural features accurately, also avoiding unnecessary computational effort and excessive data acquisition time.

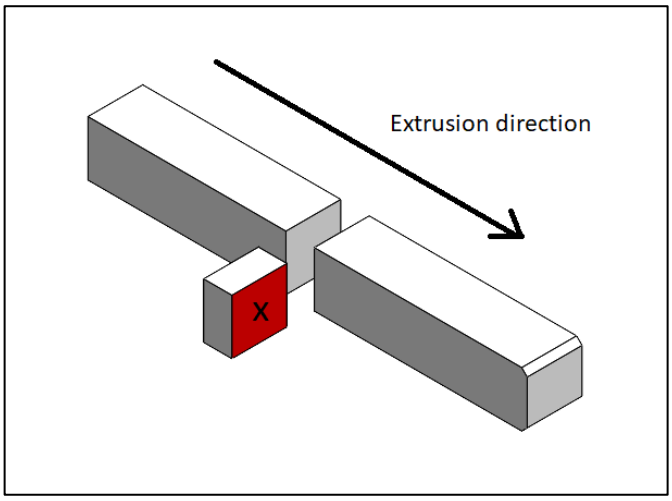

Figure 4.3: Illustration of the cutting plane-X for microstructures characteristics.

4.2.2 Microstructure Results for CG, 4P, and 8P Material

The microstructure of the CG material is shown in Figure 4.4a. The CG material refers to the as-received or unprocessed material. It exhibits an inhomogeneous structure with small, large, and elongated grains. Figure 4.4b shows the microstructure image of the 4P material, which indicates the presence of shear bands as well as fine grains. Almost all large-elongated grains are aligned in the same direction. The colour variation of the large elongated grains suggests a single preferred orientation. According to Prangnell et al. (2004), this pattern of elongated grains, known as 'lamella', mostly occurs at low to medium numbers of passes ranging from two to four, as shown in Figure 4.5a for four passes of ECAP using route A.

Figure 4.4c shows the 8P material, which displays an almost homogenous fine-grained microstructure with reduced lamella boundaries. Compared to Figure 4.5b, the microstructure map still shows lamella boundaries, even though the process successfully produced fine grain size. Colour variation within the grains of the 4P and 8P materials suggests that misorientation occurs during the I-ECAP process.

From these results, route B_C produces a more homogenous microstructure compared to route A. This finding is supported by previous studies, which also concluded that route B_C is the most effective route to produce nearly homogeneous microstructures after a minimum number of passes (Oh-Ishi et al., 1998).

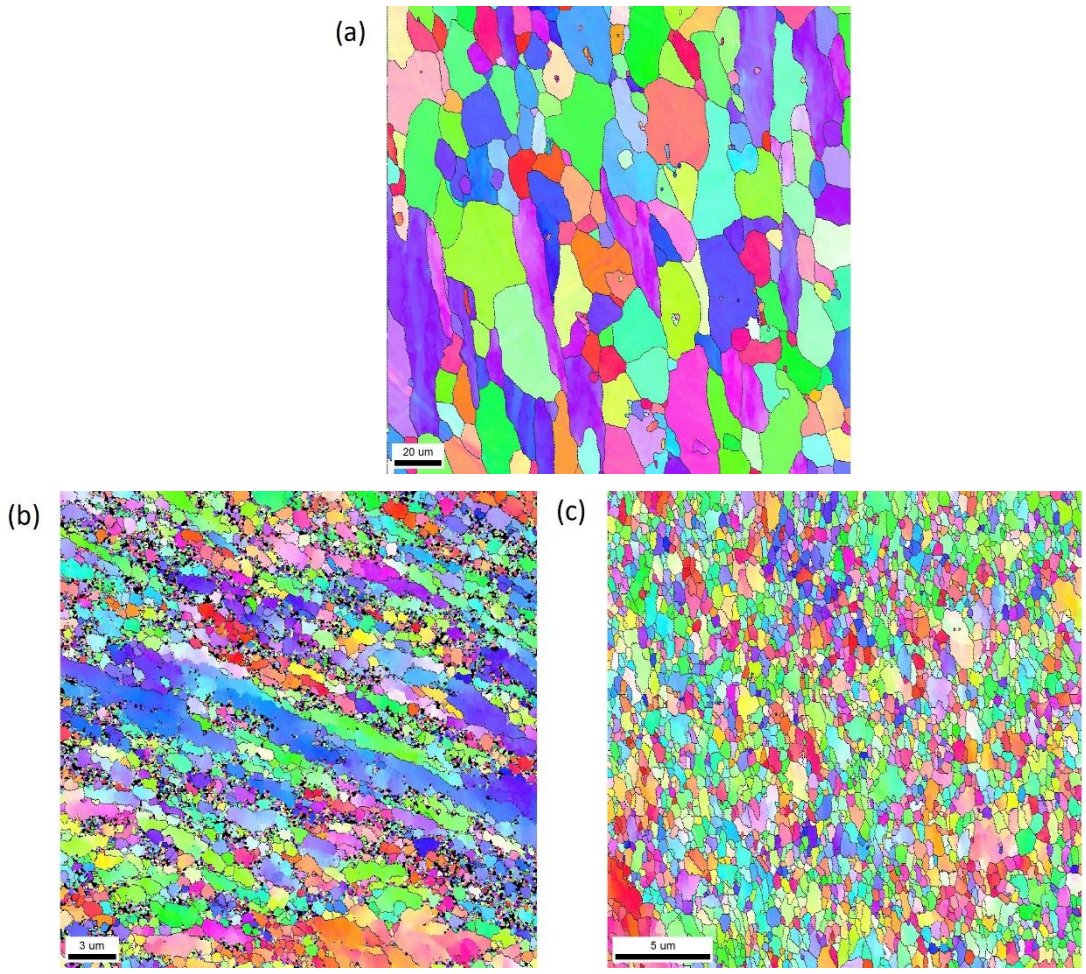

Figure 4.4: EBSD orientation maps of the microstructures for CG (a), 4P (b), and 8P (c) materials processed by I-ECAP route B_C.

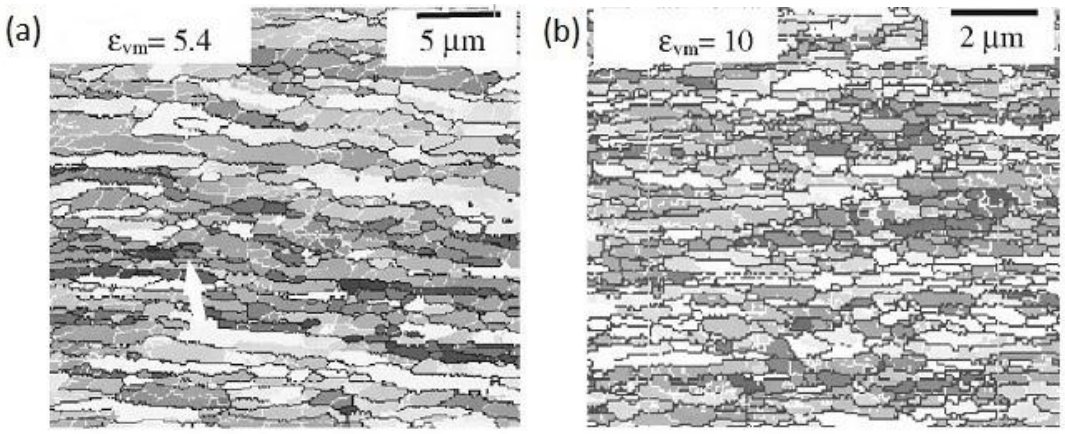

Figure 4.5: SEM images of the microstructures of Al-0.1Mg alloy deformed by ECAP at 20 °C using route A for four passes (a), and eight passes (b) (Prangnell et al., 2004).

Figure 4.6a shows the column chart of the grain size distribution for the CG material with respect to area fraction. Grain size analysis reveals an average grain size of approximately 20 μm for the CG material. The grain size distribution ranges from 1.77 to 42.26 μm, with dominant sizes in the ranges of 10-20 μm and 25-35 μm, indicating a slightly bimodal distribution.

Figures 4.6b and Figure 4.6c show the column charts of grain size distribution for the 4P and the 8P material, respectively. In both cases, a UFG structure was achieved, with average grain sizes of 0.49 μm for 4P and 0.44 μm for 8P. In the 4P material, about 60% of the grains are smaller than 2.0 μm, while in the 8P material, more than 80% of the grains are smaller than 1.0 μm.

These results show that increasing the number of passes, up to eight, not only makes the grains finer but also makes their sizes more uniform.

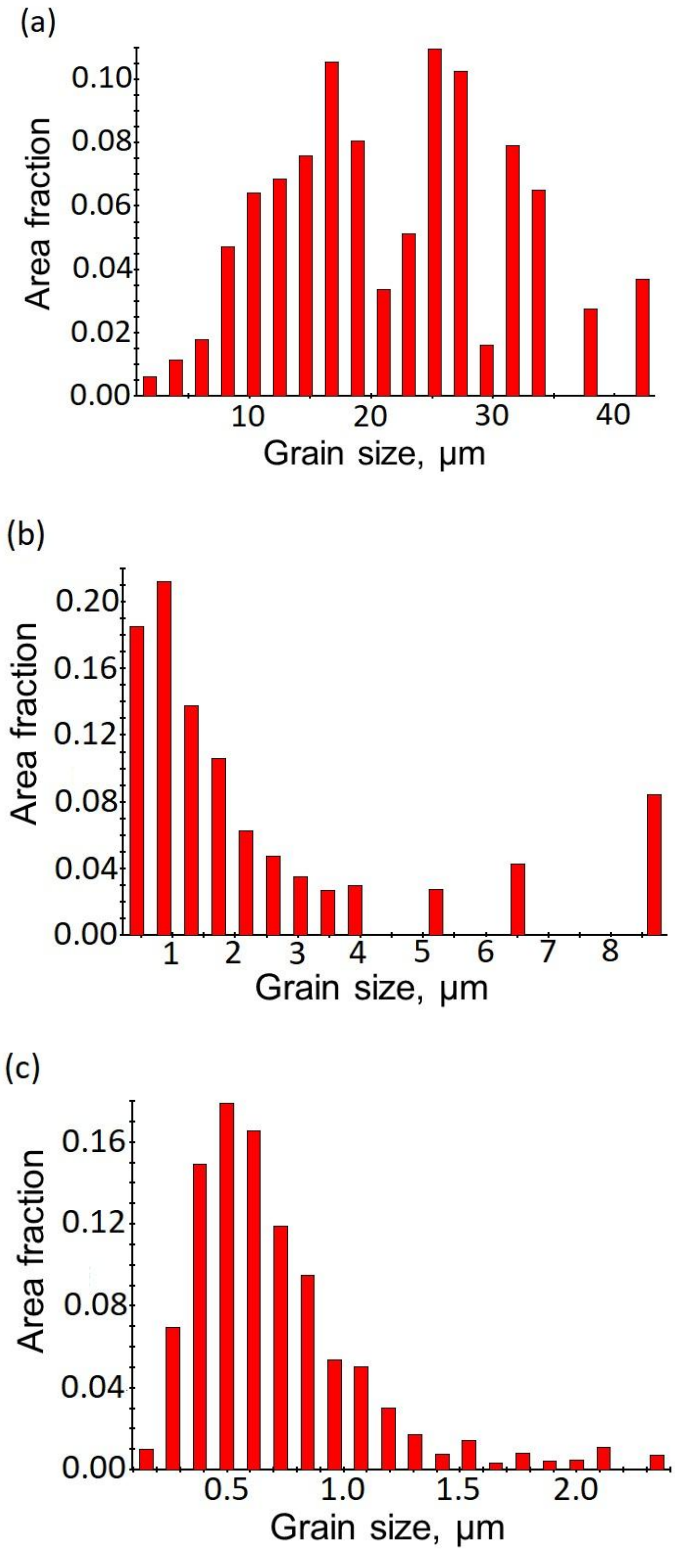

Figure 4.6: Grain size distribution charts for the CG (a), 4P (b), and 8P (c) materials.

In addition to grain size distribution, EBSD analysis provided information on the distribution of grain boundary misorientation angle. Figure 4.7a, Figure 4.7b, and Figure 4.7c show the column charts of misorientation angle with respect to area fraction for the CG material, the 4P material, and the 8P material, respectively. From these three figures, the percentage graphs for LAGB and HAGB were plotted as shown in Figure 4.8.

After eight passes, the HAGB fraction increased from 27% in the CG material to 69% in the 4P material, and further to 72% in the 8P material. This trend is similar to that published by Park et al. (2004), who conducted ECAP of annealed Al 5083 specimens at 473 K using the same route B_C, which resulted in an increase in HAGB from 35% to 50% for 4 passes and 8 passes, respectively.

Compared to Park's results, this study showed a more significant change in grain boundaries during the I-ECAP process, with the fraction of HAGBs increasing from 27% to 72%. This demonstrates that the material created more robust and stable boundaries, which may improve its performance and toughness.

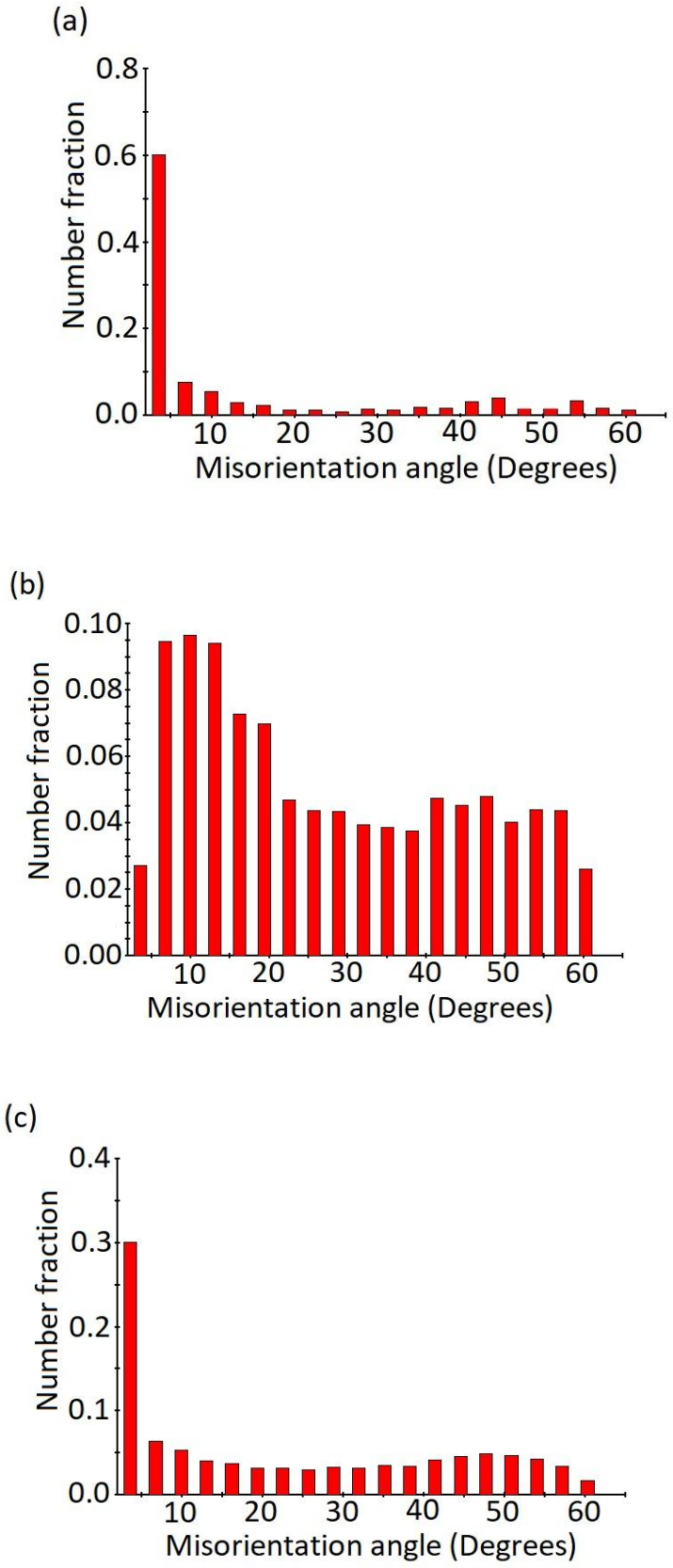

Figure 4.7: Misorientation angle distribution chart for the CG (a), 4P (b), and 8P (c) materials.

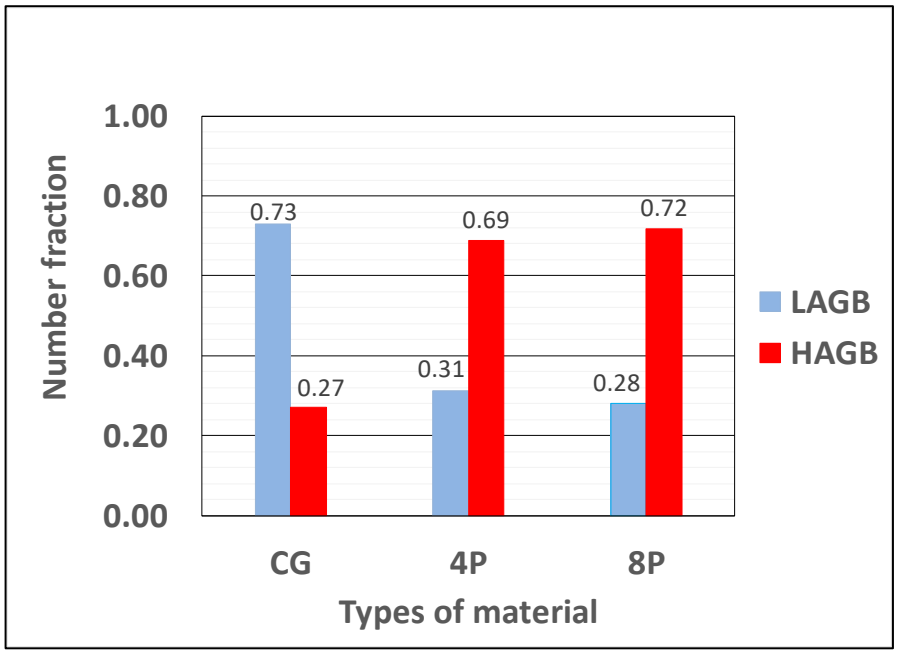

Figure 4.8: LAGB and HAGB fractions in CG, 4P, and 8P materials.

4.3 Tensile Testing Setup and Specimen Preparation

The basic mechanical properties of Al 5083 coarse grain annealed (CGA), CG, 4P, and 8P materials were investigated using a tensile test at RT with an initial strain rate of 2×10^{-2} s^{-1}. CGA indicates the as-received material, which has gone through annealing at 400 °C for 30 minutes followed by natural air cooling. The CGA material was included in the testing to compare the stress-strain behaviour with that of the non-annealed CG material.

Due to limited billet dimensions, miniature flat specimens, with the geometry shown in Figure 4.9, were used. These specimens were cut from the billet parallel to the rolling direction. Specimens were machined using wire electrical discharge machining (Wire EDM). At least two tests were carried out for each material to verify the repeatability of the results. Tensile testing was conducted on an Instron 5969 universal testing machine, with a maximum load capacity of 50 kN and an extensometer (model no: 2630-105/401) as shown in Figure 4.10a. Figure 4.10b shows the flat specimens before and after testing for all materials.

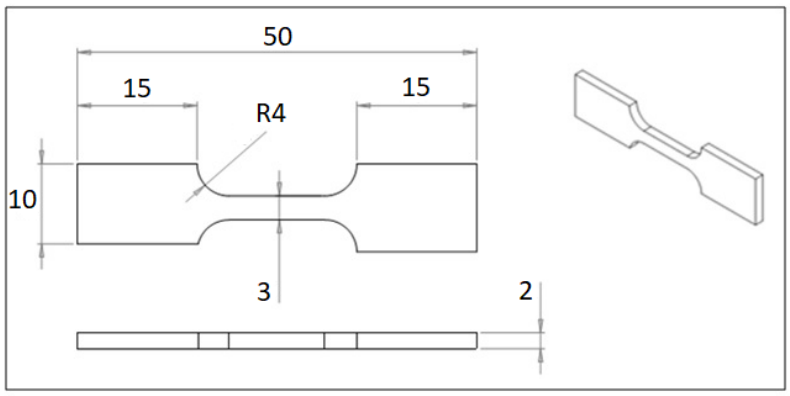

Figure 4.9: Geometry of the miniature flat tensile specimen.

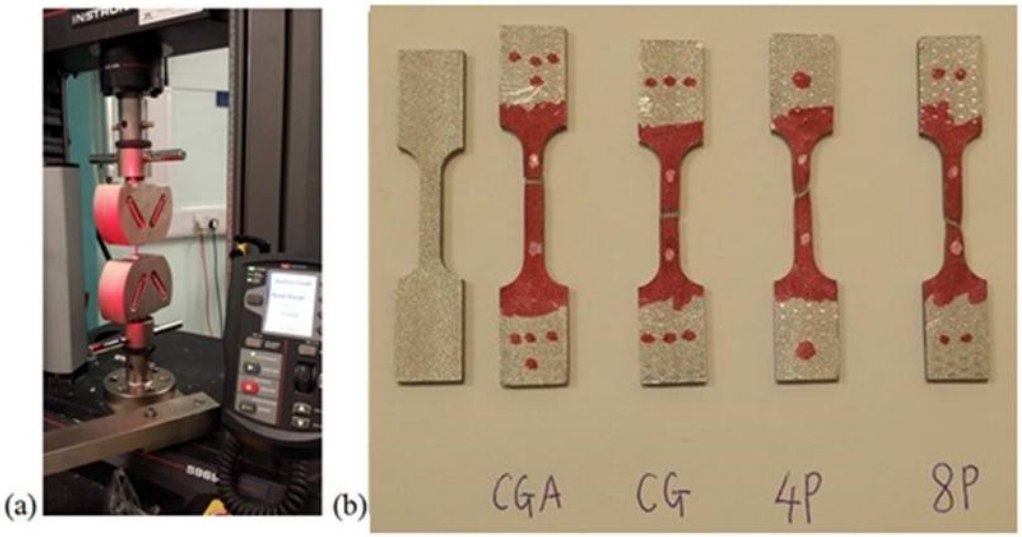

Figure 4.10: Instron 5969 universal testing machine (a), flat specimens before and after tensile testing at RT (b).

4.3.1 Tensile Test Results

Engineering stress-strain curves obtained from the tensile tests at RT for the CGA, CG, 4P, and 8P materials are shown in Figure 4.11. The curves for CGA, 4P, and 8P exhibit patterns almost identical to those published by Chang et al. (2005), as shown in Figure 2.18(b) (ECAP using route C at 473 K).

For the CGA material, the yield strength and UTS are similar to Chang et al. (2005), approximately 140 MPa and 290 MPa, respectively. The elongation to failure for the CGA material is slightly higher, at approximately 32%, compared to Chang's material at roughly 20%. Chang et al. (2005) annealed the Al 5083 samples at 723 K

for 1 hour before ECAP, which resulted in grains with an average size of about 200 µm. In contrast, the grain size of the CGA material is around 20 µm. This smaller grain size of the CGA material helps to increase elongation to failure and improves ductility by allowing more uniform plastic deformation.

The yield strength and UTS for the 4P material are 300 MPa and 350 MPa, respectively, while Chang's values are higher, at 380 MPa and 410 MPa. After eight passes, Chang's yield strength and UTS increase further to 400 MPa and 430 MPa, compared to the 8P material, which decreases by 12.5% and 9% respectively. The elongation to failure for the 4P and 8P materials increases by approximately 50% and 45%, relative to Chang's material.

These differences may be attributed to variations in annealing conditions, as the present study used 400 °C for 30 minutes with natural air cooling, while Chang's study used 723 K for 1 hour. Other contributing factors may include differences in alloy composition, grain size, and experimental setup.

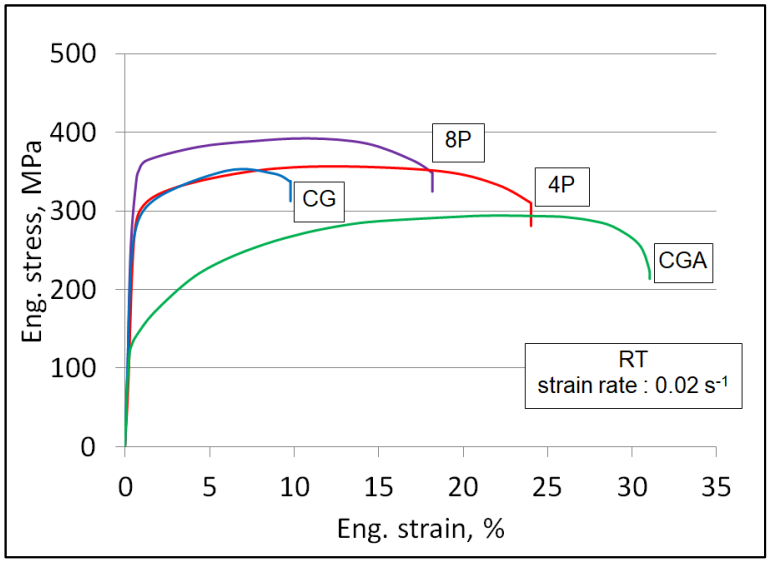

Figure 4.11: Engineering stress-strain curves of Al 5083 for CGA, CG, 4P, and 8P materials.

Based on Figure 4.11, the tensile properties of the CG, 4P, and 8P materials at RT can be compared using a column chart, as shown in Figure 4.12. The chart shows that as the material changes from the CG state to the 4P and 8P states, both the yield strength and UTS increase. This proves that the I-ECAP process makes the material stronger by refining its microstructure.

Compared to the CG material, the yield strength of the 4P and 8P materials improves by 3% and 17%, respectively. Similarly, the UTS of the 4P and 8P materials increases by 3% and 13%, respectively. This suggests that doing more I-ECAP passes gradually makes the material stronger, probably because the grains become finer, more dislocations build up, and the material deforms more evenly.

However, the elongation to failure for the 8P material decreased to 18%, compared to 24% for the 4P material, while both remained higher than the 10% elongation observed for the CG material. The material after four I-ECAP passes improves both strength and ductility, but the 8P material slightly reduce ductility, probably because too many grain boundaries and dislocations make it harder for the material to stretch. The 4P material is able provide good balance between strength and ductility, highlighting that controlling the number of ECAP passes is important for optimum desired properties.

Overall, these results show the relationship between strength and ductility in number of I-ECAP-processed Al 5083. More I-ECAP passes make the material stronger, but they can also slightly reduce how much it can stretch. This matches what microstructural studies have found: very fine grains improve strength but can limit the material's ability to harden further at higher passes.

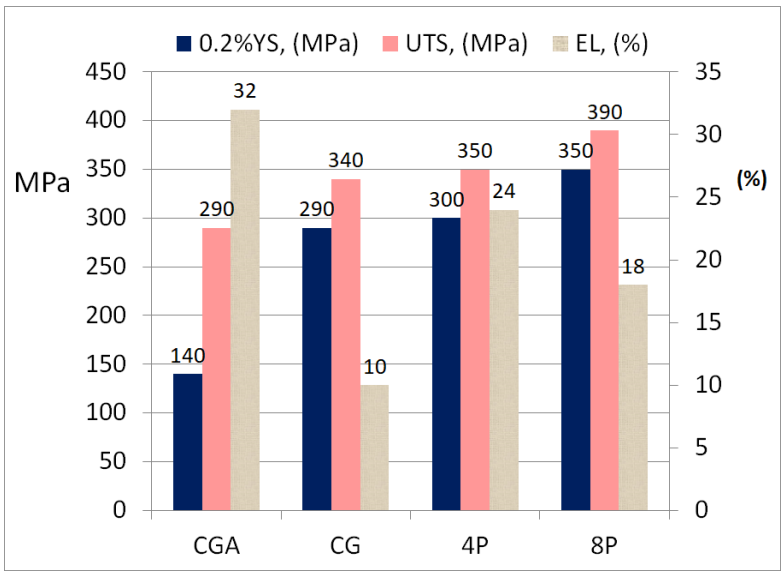

Figure 4.12: Column chart showing the 0.2% yield strength, UTS, and elongation to failure (EL) of CG, 4P, and 8P specimens tested in tension at RT.

4.4 Compression Testing Procedure

Compression tests are commonly performed by applying compressive pressure to a specimen to figure out how a material behaves under crushing loads. The flow curves obtained from compression and tensile testing differ significantly. Flow curves from tensile testing are only valid up to necking, which occurs at strains substantially lower than those expected in backward extrusion. Therefore, compression testing is essential, as backward extrusion is very much compression dominated. The compression flow curve is then used as an input material model in simulations.

There are six modes of deformation in compression testing: buckling, shearing, double barrelling, barrelling, homogeneous, and compressive instability. The specimen ratio between the length (L) and diameter (D) is used to categorise these modes as shown in Figure 4.13.

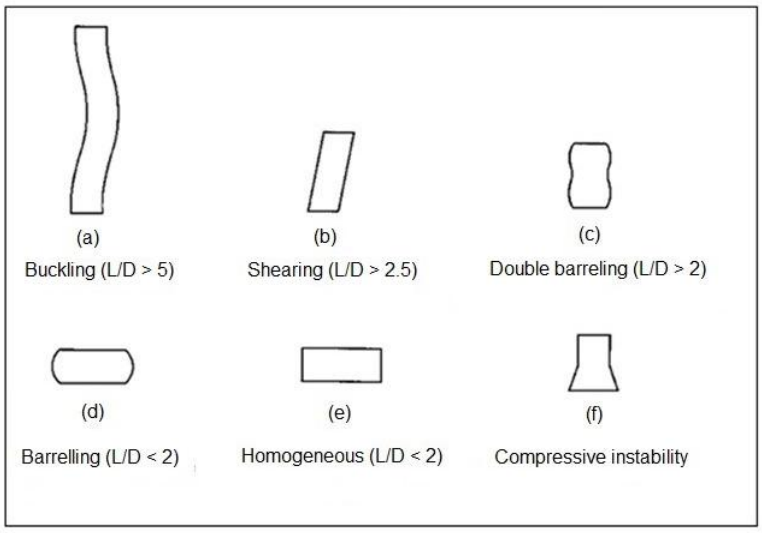

Figure 4.13: Modes of deformation in compression testing (adapted from Instron Company).

The focus for mode of deformation was on homogeneous. An aspect ratio (L/D) of 1 was chosen to avoid any possible buckling, as well as to save the material. The geometrical details of the specimens used in this testing are shown in Figure 4.14, which follows Rastegaev's geometry (Rastegaev, 1940). There is a shallow flat recess on both ends of the specimen to accommodate lubricant. The purpose of the recess is

to prevent lubricant being squeezed out during the compression testing. This could reduce the friction and minimise barrelling during compression testing.

The specimens were cut from the middle section of the ECAPed billet to avoid regions affected by end effects. The specimen's axis was oriented parallel to the billet axis as shown in Figure 4.15. A molybdenum disulphide (MoS_2) lubricant was used on both ends to reduce the friction between the specimen and a pair of parallel platens during the compression testing as illustrated in Figure 4.16.

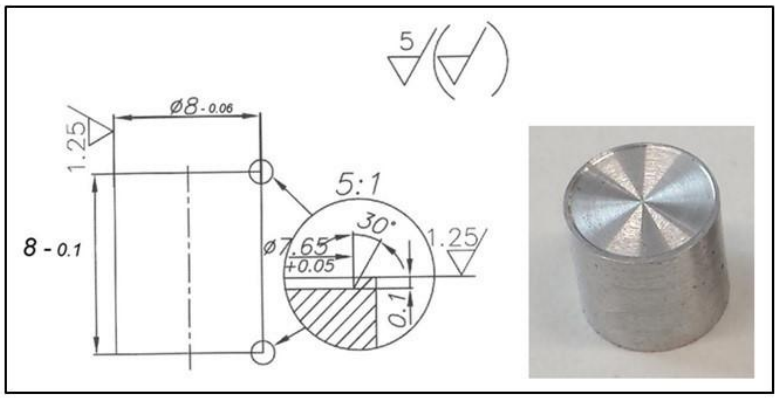

Figure 4.14: Geometrical dimensions and actual specimen used for compression testing.

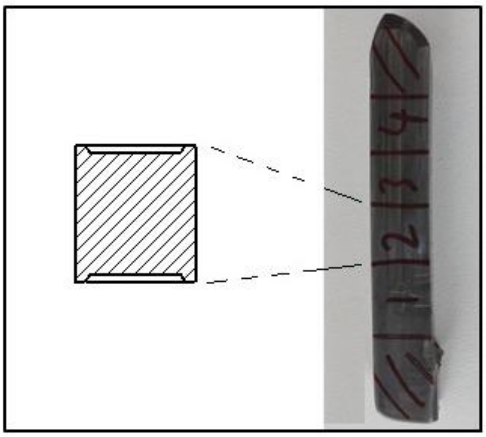

Figure 4.15: Compression specimens cut from the ECAPed billet.

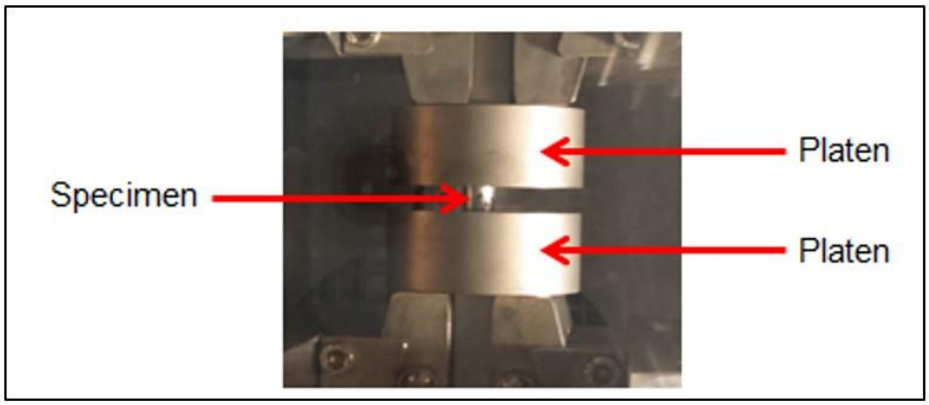

Figure 4.16: Specimen placed between parallel platens during compression testing.

Compression testing was carried out at RT and elevated temperatures with axial force applied at different constant strain rates based on constant rates of crosshead travel using a 100 ±0.5 kN Instron 8801 machine equipped with a 500 series heat chamber (± 1 °C) as shown in Figure 4.17.

Figure 4.17: Instron 8801 testing machine equipped with a heating chamber.

The specimen was placed inside the heat chamber upon reaching the testing temperature. Then, the specimen was heated and held for 10 minutes at the testing temperature before the test started at a pre-load of 0.5 kN. The test was stopped automatically at a 77% reduction in specimen height, corresponding to an equivalent plastic strain of 1.5. However, the true strain value is recorded only up to approximately 1.3. This condition is related to machine compliance or elastic deflection, whereas testing machine is subjected to deform. The deformations are associated with the load frame, load cell, and grips, which need to be removed from the measurement. Corrected true stress-strain were calculated based on the compliance of the testing machine for load and displacement, as explained by Kalidindi et al. (1997). Each type of specimen underwent at least two tests to verify the repeatability of the results. The parameters for compression testing are shown in Table 4.1.

Table 4.1: Compression testing parameters.

Material	Temperature, °C	Constant strain rate, s^{-1}
CG, 4P, 8P	RT	1×10^{-2}
	200, 250, 300	1×10^{-2}, 1×10^{-3}

4.4.1 Results at RT and Constant Strain Rate of 1×10^{-2} s^{-1}

Figure 4.18 displays the compression true stress-strain results for CG, 4P, and 8P testing at RT and constant strain rate of 1×10^{-2} s^{-1} and shows that increasing the number of passes results in increased flow stress, a typical result for UFG materials. The compression 0.2% yield strength for CG, 4P, and 8P is around 160, 340, and 380 MPa, respectively, which means that the compression yield strength increases approximately 2.125 times after four passes and changes only slightly after eight passes. At a true strain of 1.3, the true stress is about 490, 540, and 590 MPa for CG, 4P, and 8P material, respectively. The compression curves for 4P and 8P materials gradually increase over the true strain range.

The values of compression testing beyond a true strain of 1 are still debated among researchers, as they may not be well represented; the sample is so thin that the material flow differs significantly from the "free flow" observed in the earlier stages of the compression test. The decision to test beyond a true strain of 1 was dictated by the fact that the equivalent strain in backward micro-extrusion could be larger than 1, so some insight into this strain range could also be valuable. The specimens after the test are shown in Figure 4.19.

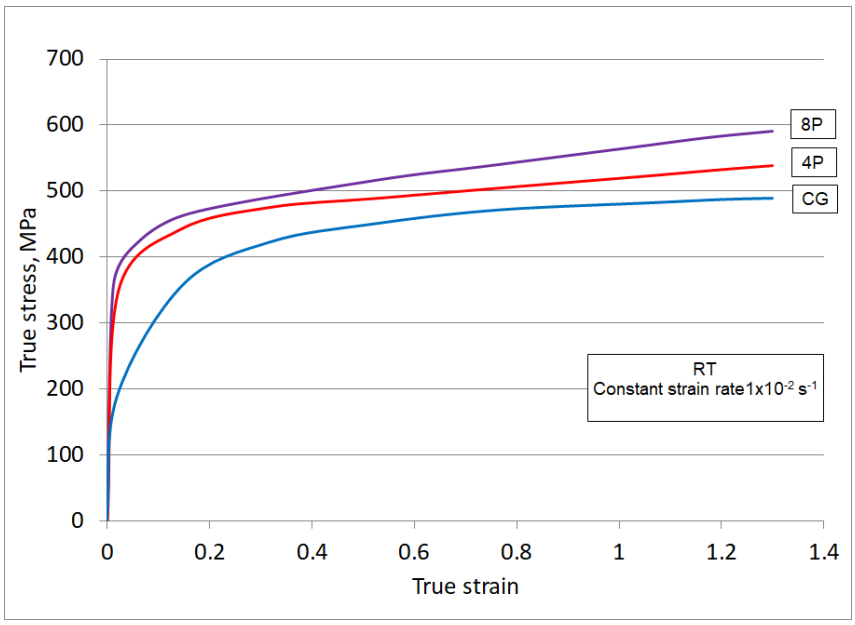

Figure 4.18: Compression true stress-strain curves for 8P, 4P, and CG specimens tested at RT and constant strain rate of 1×10^{-2} s^{-1}.

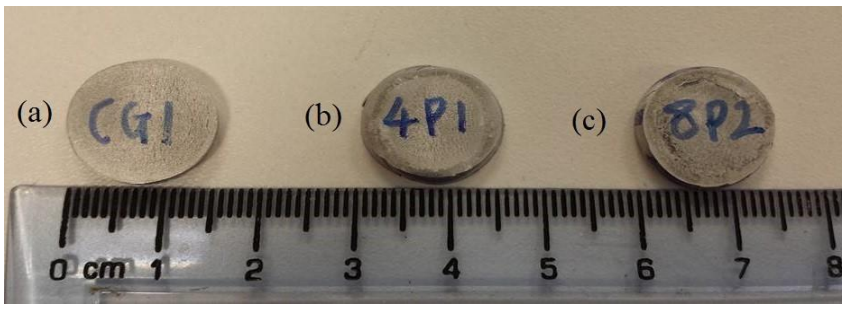

Figure 4.19: The specimens after compression at RT and constant strain rate of 1×10^{-2} s^{-1} for CG (a), 4P (b), and 8P (c) materials.

4.4.2 Results at a Constant Strain Rate of 1×10^{-2} s^{-1} and Different Temperatures

Figure 4.20(a), (b), and (c) show the flow curves for the CG, 4P and 8P materials obtained by compression testing at three different temperatures of 200, 250, and 300 °C, conducted at a constant strain rate of 1×10^{-2} s^{1}. All the curves show a similar shape, increasing steadily with the true strain values. The curves begin to rise more rapidly at a true strain of around 0.8, which is especially noticeable at higher temperatures. Figure 4.21(a), (b), and (c) show all the specimens after compression testing.

The curve patterns show different comparisons at RT, whereas at elevated temperature the UFG material (4P and 8P) exhibits lower flow stress compared to the CG material. The flow stress for the 8P material is also lower than that of the 4P material. The yield strength decreases by around 67% with the increase in temperature from 200 °C to 300 °C for the CG material. While, for the 4P and 8P materials, it is reduced by around 53% and 35% respectively. The results reveal that the flow stress decreases with the increase of testing temperature for both the UFG and CG material.

Furthermore, the CG material exhibits a plateau or even a shallow saddle at lower temperature (200 °C), which may lead to the formation of shear bands. In contrast, the UFG materials do not show this slight curvature, indicating that they are more resistant to shear banding.

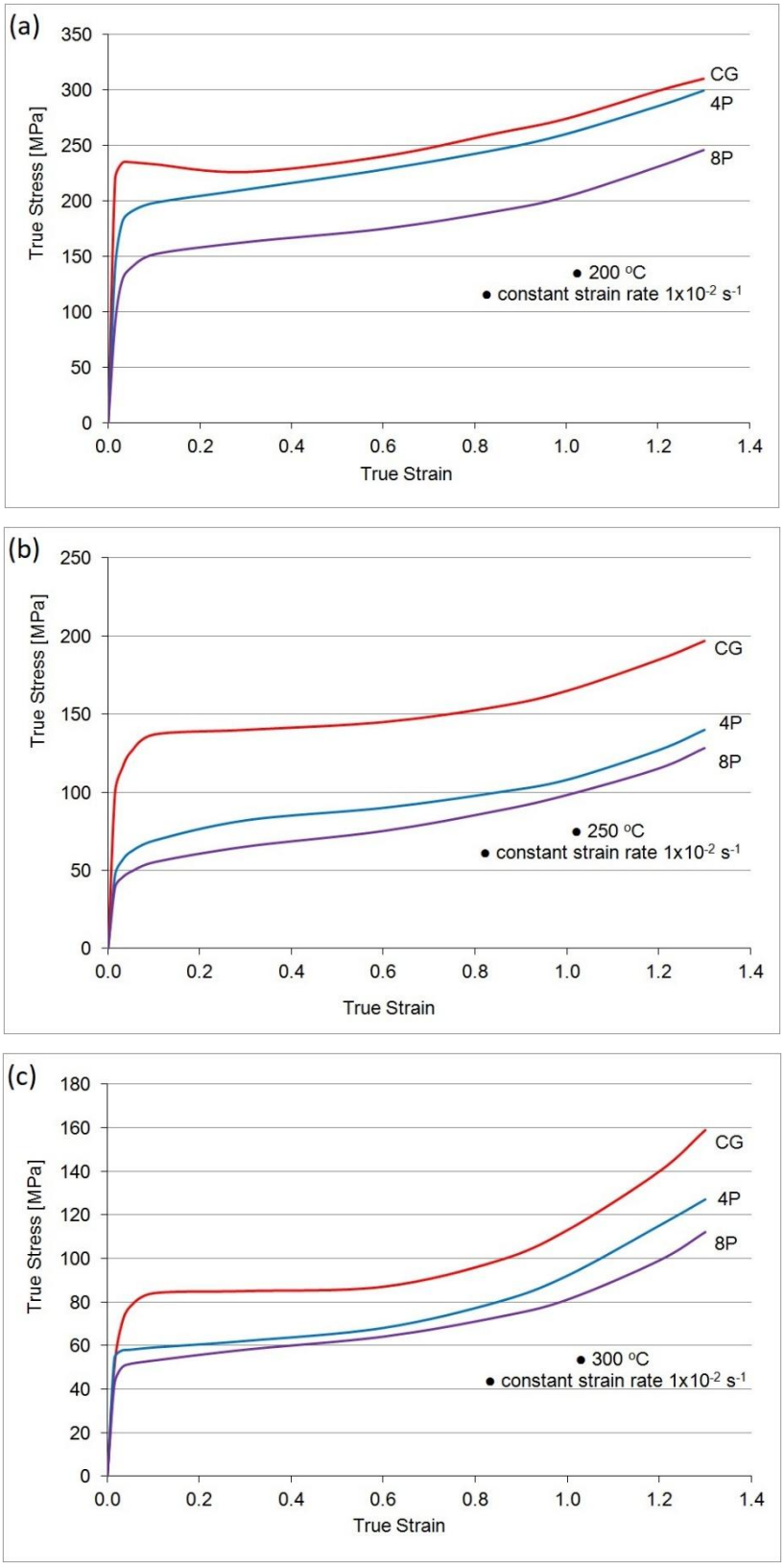

Figure 4.20: True stress-strain curves for CG, 4P, and 8P material compression tested at a constant strain rate of 1×10^{-2} s^{-1} and different temperatures of 200 °C (a), 250 °C (b), and 300 °C (c).

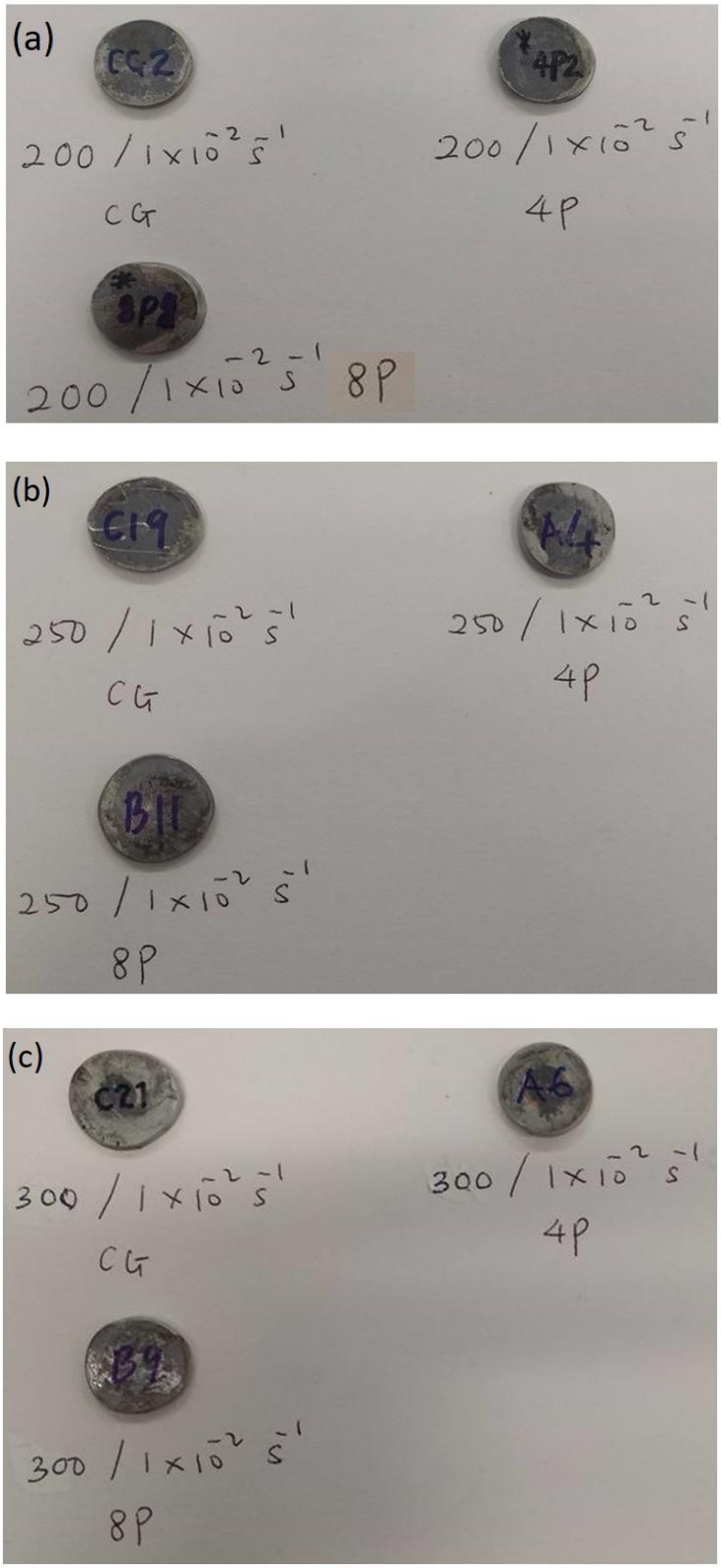

Figure 4.21: Specimens after compression testing of CG, 4P, and 8P material at a constant strain rate of 1×10^{-2} s^{-1} and different temperatures of 200 °C (a), 250 °C (b), and 300 °C (c).

4.4.3 Results at a Constant Strain Rate of 1×10^{-3} s^{-1} and Different Temperatures

Figure 4.22(a), (b), and (c) show the flow curves for the CG, 4P and 8P materials obtained by compression testing at three different temperatures of 200, 250, and 300 °C, conducted at a constant strain rate of 1×10^{-3} s^{1}. The curve patterns for the materials tested at this constant strain rate are similar to those obtained at the higher strain rate of 1×10^{-2} s^{-1}, except that all specimens exhibit lower stress levels.

It can be observed that the CG material tested at 250 and 300 °C shows a rapid stress drop immediately after the yield point. Such strain softening is attributed to the internal heat generated due to plastic deformation. For the CG material, it is predicted the temperature rise is higher than the UFG material due to its larger grain size, which manifests as strain softening. The constitutive equations are presented to describe the deformation behaviour resulting from the flow softening during plastic deformation. This phenomenon was explained in detail by Zhou and Clode (1998).

According to Ding et al. (2020), lower strain rate or higher temperature is able to create the softening curve. Lower strain rate assists more time for energy accumulation, while higher temperature gives more mobility of grain boundary, both conditions reduce the rate of dynamic recrystallisation grain generation. This strain softening is much more obvious in the CG material, which explains why strain softening occurs in the CG material under lower strain rate and high-temperature condition, as shown in Figure 4.22(b) and (c).

Strain softening has also been observed during compression tests at elevated temperature on modified Al 5083 (grain size ~180 μm) produced by ingot metallurgy (Kaibyshev et al., 2005), and for rolled Al 5083 (grain size ~10 μm) (Pérez-Bergquist et al., 2011). Figure 4.23(a), (b), and (c) show all the specimens after compression testing at the lower strain rate (1×10^{-3} s^{-1}).

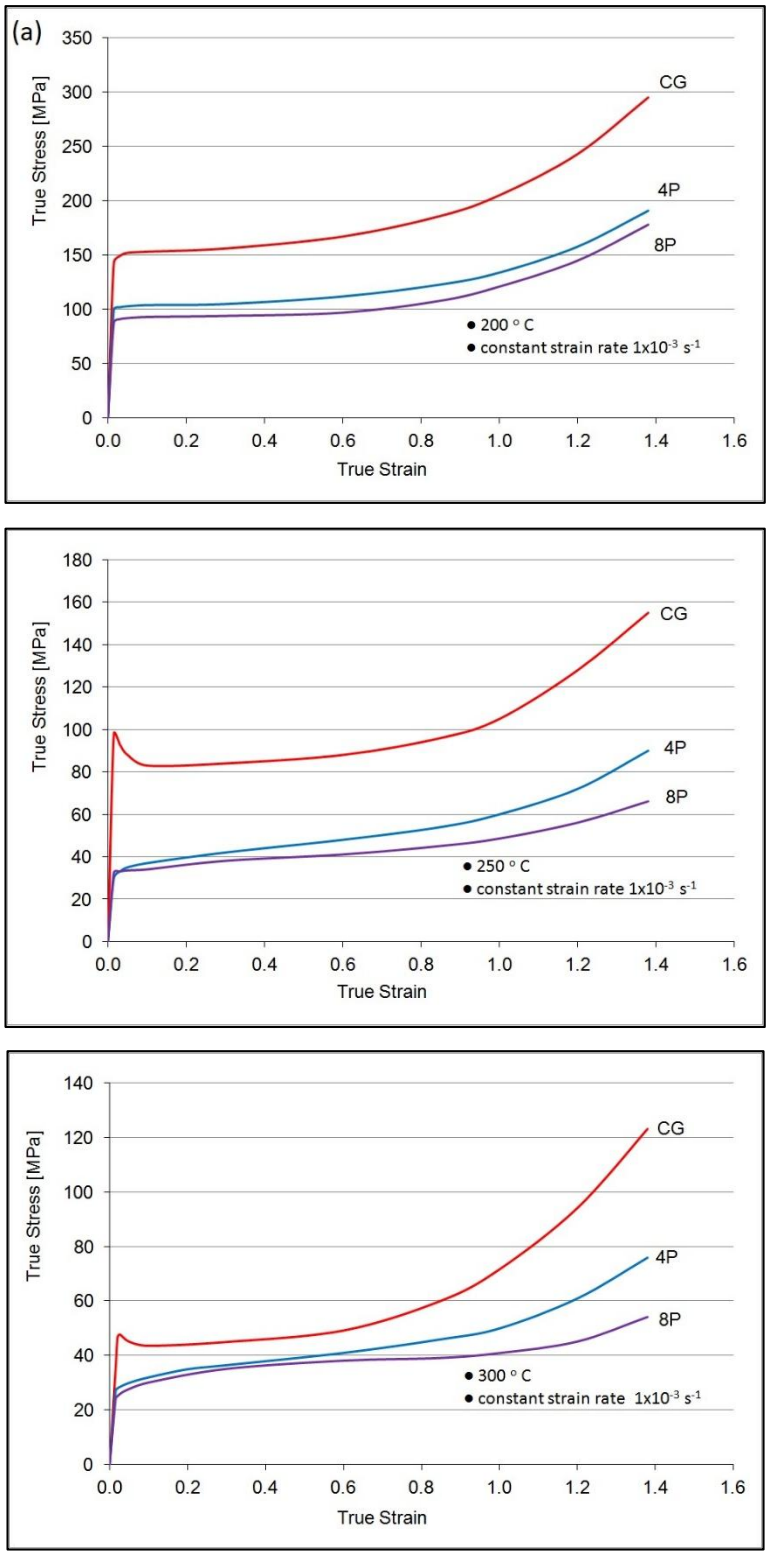

Figure 4.22: True stress-strain curves for CG, 4P, and 8P material compression tested at a constant strain rate of 1×10^{-3} s^{-1} and different temperatures of 200 °C (a), 250 °C (b), and 300 °C (c).

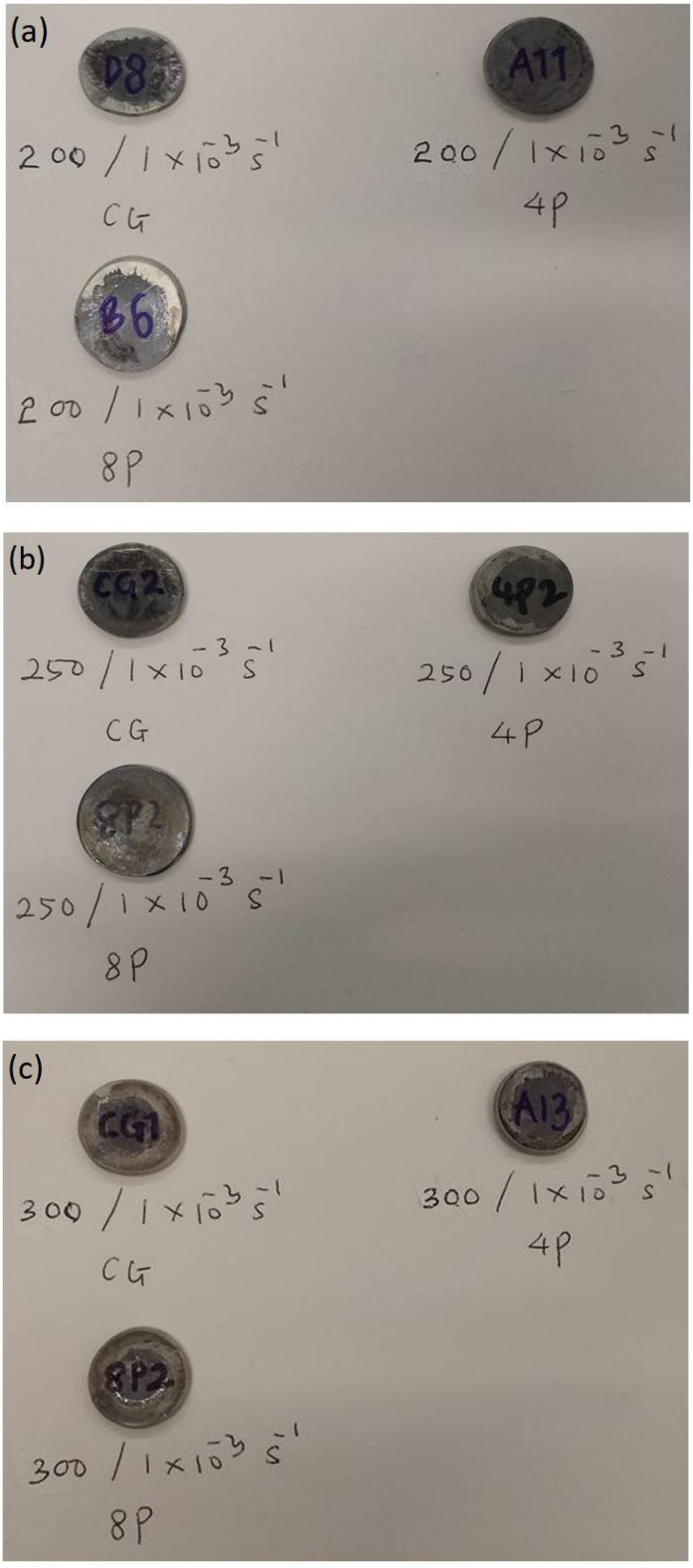

Figure 4.23: Specimens after compression testing of CG, 4P, and 8P material at a constant strain rate of 1×10^{-3} s^{-1} and different temperatures of 200 °C (a), 250 °C (b), and 300 °C (c).

4.4.4 Comparison of Compression Yield Strength for CG, 4P, and 8P at Different Strain Rates and Temperatures

There is a clear trend in material properties revealed by testing at different strain rates and temperatures as shown in Figure 4.24. At the strain rate of 1×10^{-2} s^{-1}, the CG material shows a gradual decrease in the yield strength from 230 MPa to 125 MPa, and further to 75 MPa at deformation temperatures of 200, 250 and 300 °C, respectively. The yield strength for the 4P material decreases from 180 MPa to 60 MPa, and finally to 58 MPa, while the values for the 8P material are lower than those of the 4P material at all temperatures beginning from 130 MPa, followed by 40 MPa, and slightly increasing to 50 MPa.

At the strain rate of 1×10^{-3} s^{-1}, the yield strength for all materials and temperatures is lower compared to that at of 1×10^{-2} s^{-1}. The yield strength reduction sequence for the CG material is 140, 95, and 47 MPa for deformation temperatures of 200, 250 and 300 °C, respectively. At 200 °C, the yield strength values are 100 MPa and 85 MPa for the 4P and 8P materials, respectively. In contrast to this reduction, the yield strength values are similar for the 4P and 8P materials at deformation temperatures of 250 and 300 °C (around 30 MPa).

These results are consistent with typical material behaviour at different strain rates and elevated temperatures as discussed in Subchapter 2.6. Reducing the strain rate and increasing the temperature contribute to reducing the yield strength of the material. Increasing the temperature from 200 °C to 250 °C decreases the yield strength by approximately 35% to 70% for all materials. While, increasing the temperature from 250 °C to 300 °C further reduces it by about 4% to 50% yield strength for all the materials.

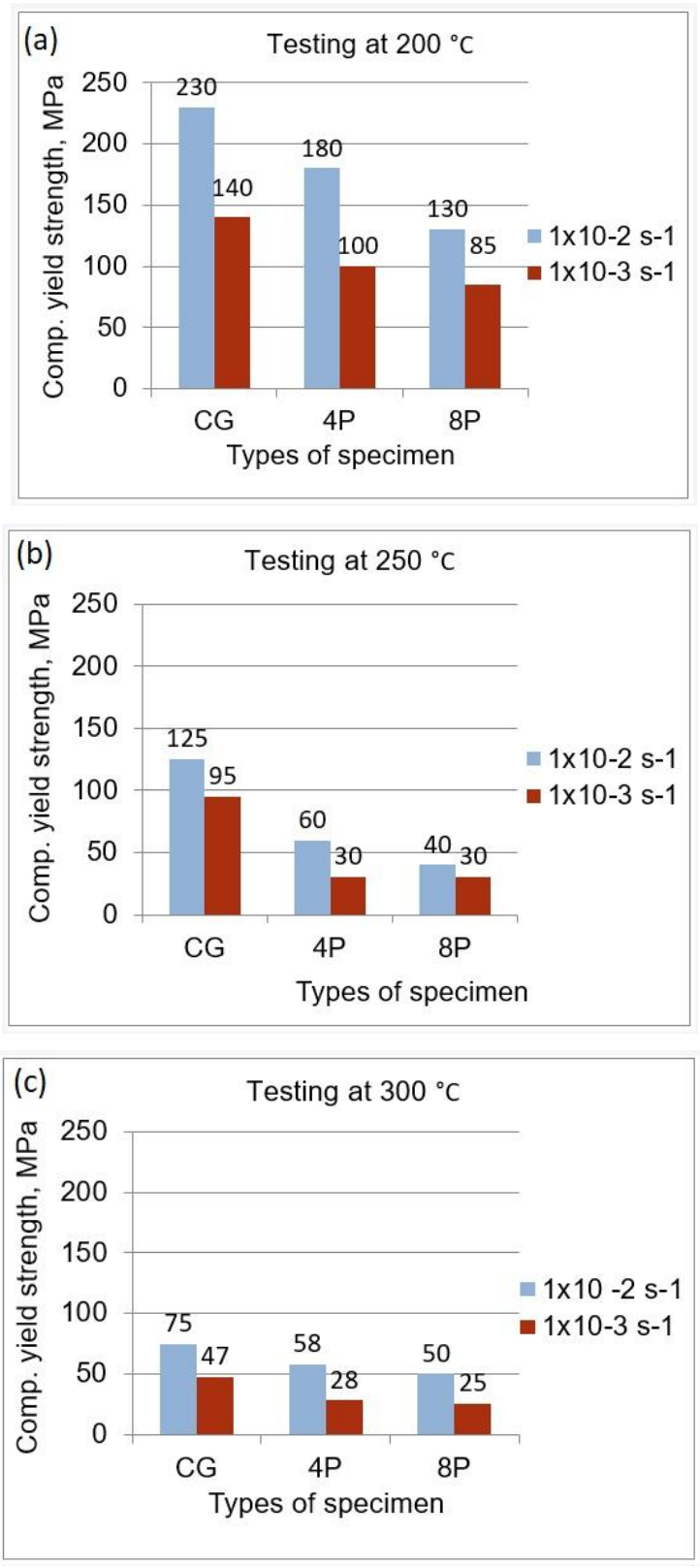

Figure 4.24: Comparison of yield strength for CG, 4P, and 8P materials compression tested at different constant strain rates (1×10^{-2} s^{-1}, 1×10^{-3} s^{-1}) and temperatures of 200 °C (a), 250 °C (b), and 300 °C (c).

4.5 Hardness Measurement Procedure

The purpose of hardness measurements was to investigate the homogeneity of strain distribution during the I-ECAP processing. Prior to testing, the CG, 4P, and 8P Al 5083 billets were polished to a mirror-like surface finish, as shown in Figure 4.25.

Vickers microhardness measurements were carried out using a DuraScan 70 G5 hardness tester (Figure 4.26) with a load of 0.05 kg and an indentation time of 15 s. The Ecos Workflow software was used for data calculation and analysis of the hardness results.

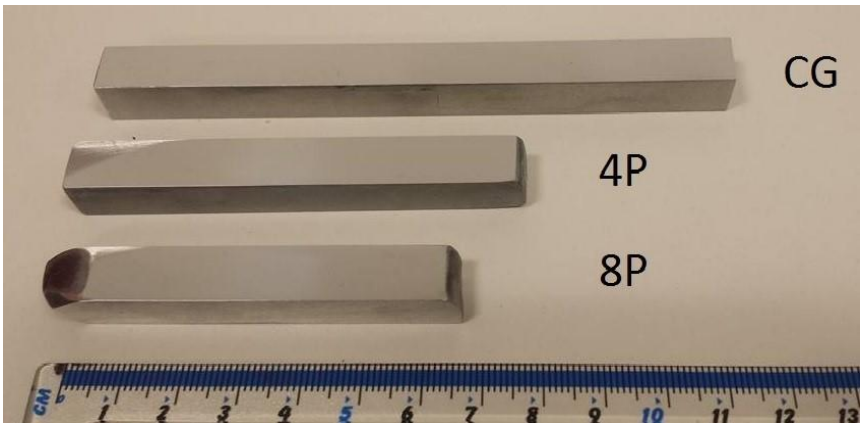

Figure 4.25: Specimens polished to mirror surface finish for hardness measurement.

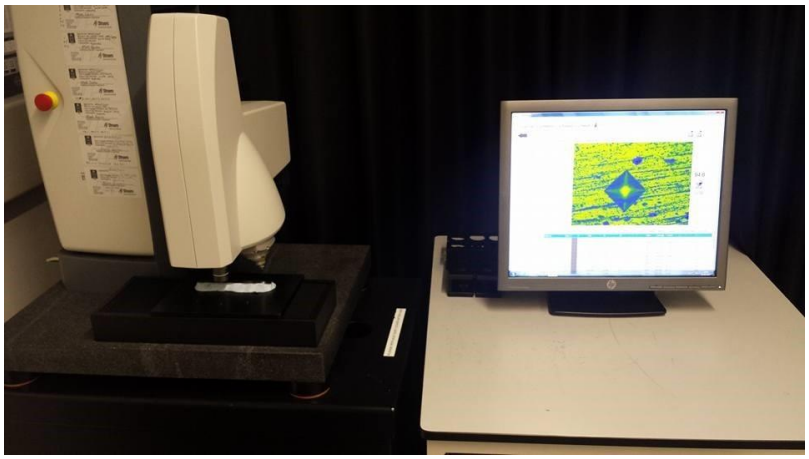

Figure 4.26: DuraScan 70 G5 hardness tester used for Vickers microhardness testing.

The microhardness measurement points were located at the middle of each billet and spaced 1 mm apart along the longitudinal axis. The first measuring point (P1) was positioned 10 mm from the billet edge, as shown in Figure 4.27, to comply with ASTM E384 requirements and to minimise edge effects for more accurate readings.

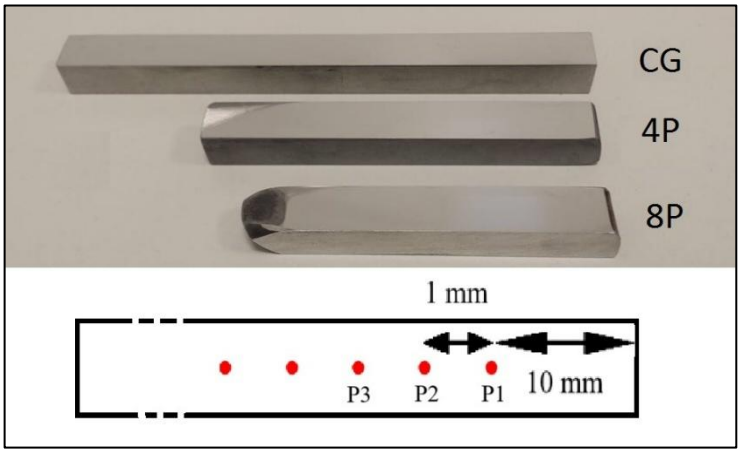

Figure 4.27: Schematic illustration of microhardness measuring points along the billet axis.

4.5.1 Hardness Measurement Results

The hardness distribution for each specimen is presented in Figure 4.28. The average Vickers hardness values for the CG, 4P, and 8P billets were 100, 118, and 122 HV, with standard deviations of 3.71, 3.73, and 3.18, respectively. The results show that hardness becomes higher with more I-ECAP passes. The smaller standard deviation after eight passes means the strain is more evenly distributed.

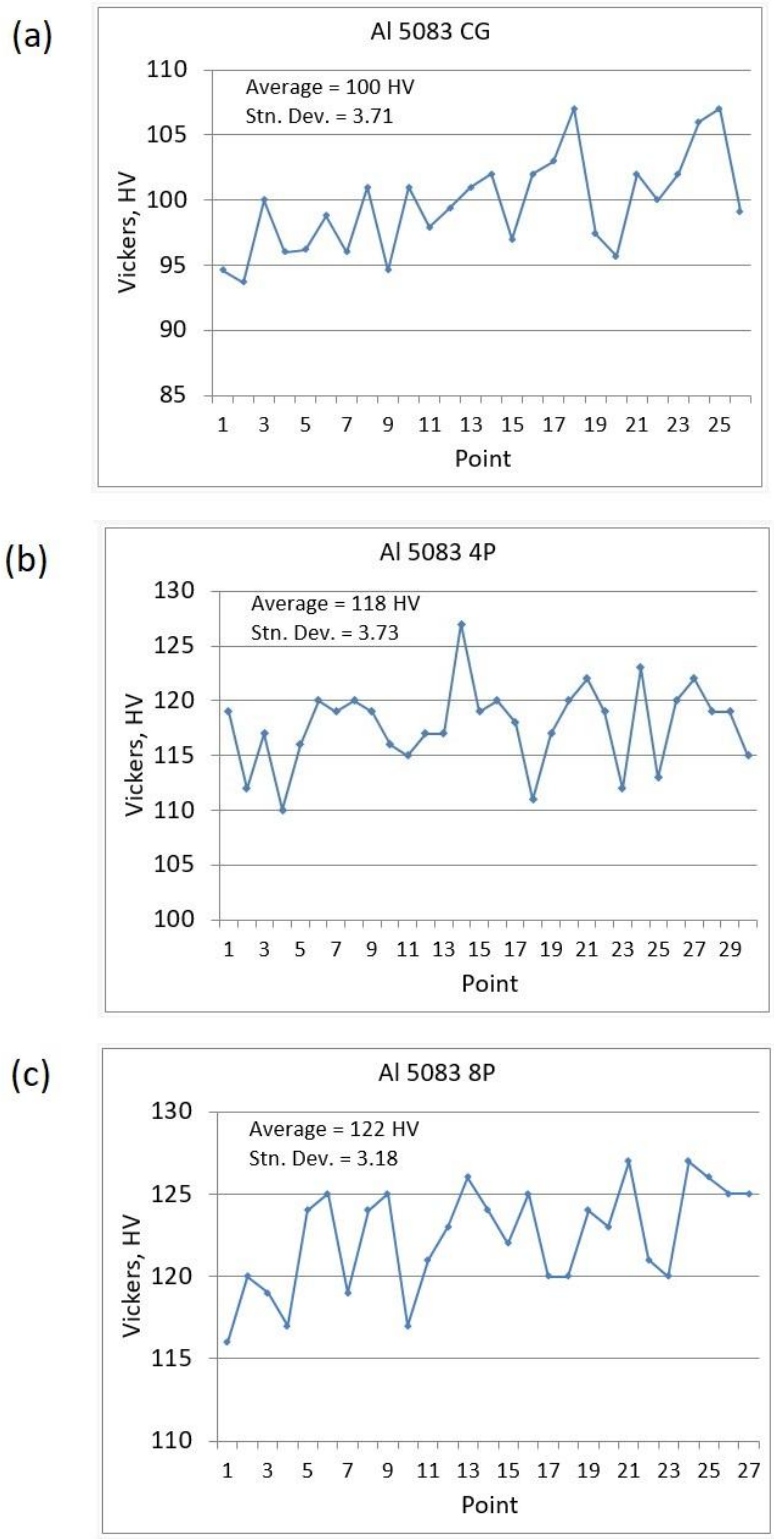

Figure 4.28: Hardness distribution of CG (a), 4P (b), and 8P (c) Al 5083 billets.

To summarise these results, Figure 4.29 shows that the average Vickers microhardness gradually increases for the 4P, and 8P material. The trend is similar to that reported by Chang et al. (2001) for the 4P material. Figure 4.30 presents Chang's results, which show a rapid increase from 80 HV to 104 HV after the first ECAP pass, followed by a slower increase until the fourth pass (around 109 HV), and remaining unchanged after the sixth and eighth passes.

According to Wu et al. (2019), a high density of HAGB reduces the effective grain size, which contributes to an increase in hardness. The increase in HAGB fraction from 69% after four passes to 72% after eight passes produced this effect.

The increase in mean microhardness is almost consistent with the trend in yield strength and UTS observed from tensile tests after I-ECAP processing (Rosochowski et al., 2007b; Park et al., 2010; Chang et al., 2012).

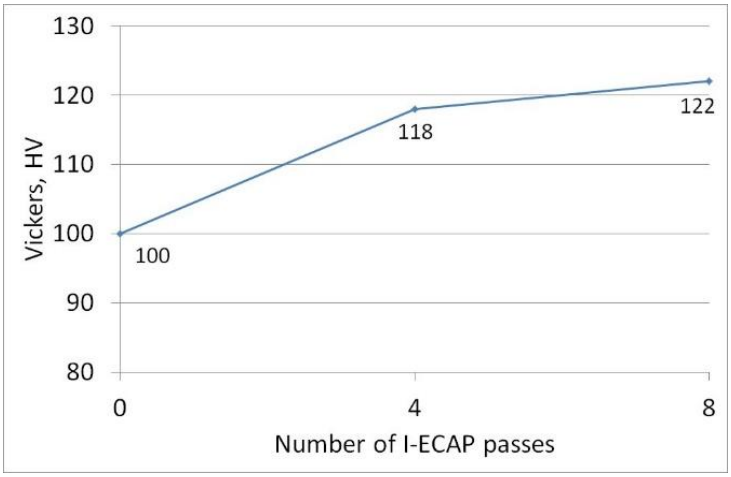

Figure 4.29: Average Vickers microhardness for CG, 4P, and 8P material.

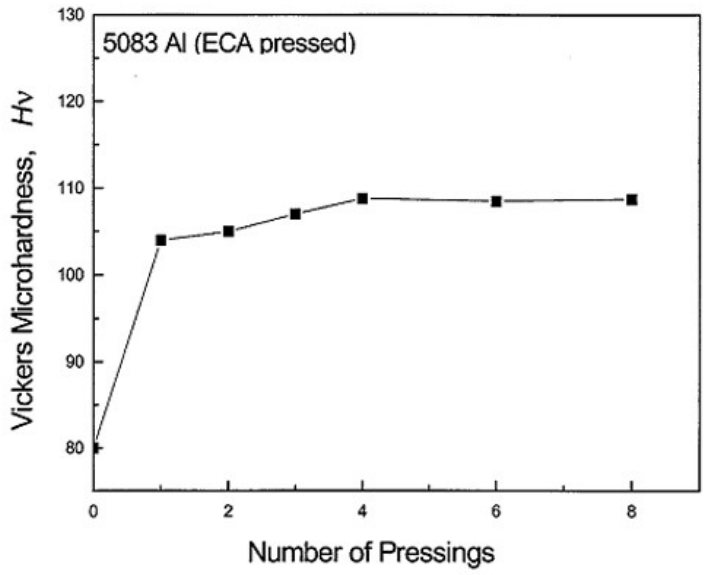

Figure 4.30: Vickers hardness variation with number of ECAP passes at 473 K using route C (Chang et al., 2001).

4.6 Summary

This chapter explains how the I-ECAP process affects the microstructure and material properties of the processed material Al 5083. The results show how grain refinement changes the mechanical properties as the number of I-ECAP passes increases.

The I-ECAP process successfully refined the microstructure of CG Al 5083, producing a UFG structure after four (4P) and eight (8P) passes. The average grain sizes for the 4P and 8P billets were 0.49 μm and 0.44 μm, respectively. The 4P billet retained some elongated grains, whereas the 8P billet exhibited a more homogeneous grain distribution.

The fraction of HAGB increased markedly from 27% in the CG material to 69% after four passes and 72% after eight passes, indicating progressive boundary stabilisation.

Tensile testing at RT confirmed that the I-ECAP process improved the material properties. The yield strength increased from 140 MPa in the CGA condition and 290 MPa in the CG material to 300 MPa for the 4P billet and 350 MPa for the 8P billet. The UTS increased from 290 MPa in the CGA material and 340 MPa in the CG material to 350 MPa for the 4P billet and 390 MPa for the 8P billet. The elongation to failure decreased from 24% for the 4P billet to 18% for the 8P billet, both remaining

higher than 10% for the CG. Overall, the 4P condition provided the best balance between strength and ductility.

Compression testing revealed that the specimens were sensitive to changes in deformation strain rate and process temperature. Higher processing temperatures or lower strain rates produced lower flow curves for all specimens.

The hardness after I-ECAP was measured using the Vickers method. The average hardness increased from 100 HV for the CG material to 118 HV for the 4P billet and 122 HV for the 8P billet. This increase in hardness followed the same trend as the rise in yield strength and UTS after I-ECAP.

Knowledge contributions and novelty

1. This study shows the successful implementation of the double-billet I-ECAP process in producing UFG billets from CG Al 5083.
2. The novelty of this study is the comparison of four-pass and eight-pass billets after the I-ECAP process. Both 4P and 8P billets produce UFG structures with closely similar grain sizes, but the additional passes mainly make the microstructure more uniform and the grain boundaries more stable.
3. The mechanical testing shows that I-ECAP improves the strength and ductility of CG Al 5083, with four passes giving the best overall balance of these properties.

Significance

1. The findings are important for microforming applications, where UFG and stable microstructures are needed to achieve high strength and good formability.
2. Four I-ECAP passes achieve the best mix of strength and ductility, while eight passes further improve microstructural uniformity and grain boundary stability.

CHAPTER 5
BACKWARD MICRO-EXTRUSION: EXPERIMENTAL AND SIMULATION RESULTS

5.1 Introduction

This chapter describes the backward micro-extrusion experiment to produce miniature conical pins, starting with the explanation of the backward micro-extrusion toolset, followed by the process parameters. The temperatures tested in this experiment were RT, 200 °C, and 250 °C. This is followed by an in-depth discussion of the experimental results, namely the pin height of the miniature conical pins. Lastly, finite element simulation was performed to compare the results with the experimental data.

5.2 Experimental Setup for Backward Micro-Extrusion

In every manufacturing process, monitoring the process is essential to provide more information and knowledge of the process. Process monitoring usually uses sensor measurements (e.g., load cells, displacement transducers) to determine the state of the process. Data obtained from load and displacement sensors can be transformed into graphs. For example, a punch force-displacement graph provides insight into the relationship between punch force and displacement. Typical punch force-displacement curves for macro forward and backward extrusion are shown in Figure 5.1.

From Figure 5.1, the extrusion process can be divided into three phases: (1) coining, (2) steady state, and (3) unsteady state (Johnson & Mellor, 1962). In the coining phase, both forward and backward extrusion are characterised by straight lines with different slopes, which gradually changes into curves. The straight-line portion

represents the elastic response of the material, while the curved region indicates the transition from the elastic to the plastic state.

In the steady-state phase, also known as the fully plastic region, each process follows its own curve, representing the material behaviour after plastic flow begins inside the die. Forward extrusion requires a higher force at the beginning of this stage to fill the container compared to backward extrusion.

Subsequently, the force in forward extrusion decreases due to reduced friction within the container. This effect is not observed in backward extrusion, where the force remains relatively constant. In the unsteady-state phase, both processes follow a similar rising curve until the end of a specific stroke distance. This increase is caused by the reduction in the material volume under the punch, which leads to higher friction and changes in the mode of material flow in this region. Figure 5.1 illustrates the coining and steady-state phases, showing that backward extrusion requires less force than forward extrusion.

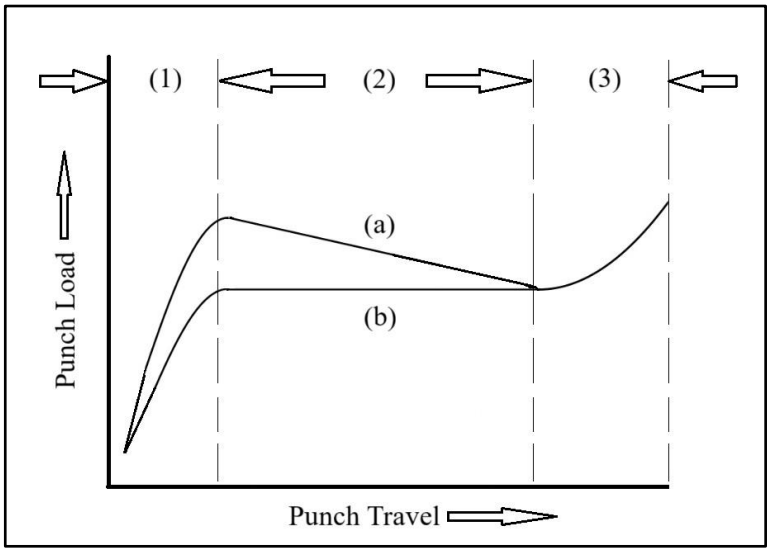

Figure 5.1: Typical punch force-displacement curves for forward extrusion (a) and backward extrusion (b) (Johnson & Mellor, 1962).

5.2.1 Design of a Typical Forward Extrusion Toolset

Figure 5.2 shows the assembly of the forward extrusion toolset. It consists of a top plate (1), a pressure plate (2), a punch (3), a die (4), a retaining ring (5), a workpiece (6), a distance plate (7), a base plate (8), another pressure plate (9), and an ejector (10).

During the process, the punch and die remain in contact with the external surface of the workpiece; therefore, both require suitable materials that can withstand the maximum contact pressure. They also need to be tough and wear resistant.

The retaining ring, or stress ring, is used to reinforce the die by generating a compressive hoop stress in the die. The distance plate is a thick block of material that supports either the punch or the die to spread the load during the process. The ejector functions to eject the extruded part from the die.

The factors to be considered before designing such a toolset include the geometry of the final product, the punch and die design, the estimated maximum load, and the operating conditions, whether at RT or elevated temperature.

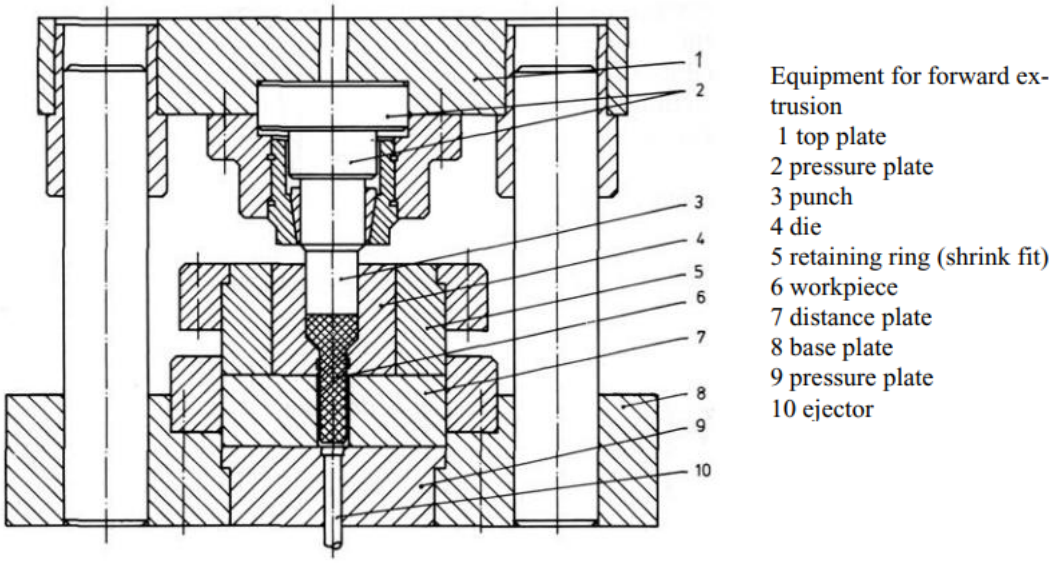

Figure 5.2: Forward extrusion toolset (Heinz, 2006).

5.2.2 Custom-Designed Backward Micro-Extrusion Toolset

The backward micro-extrusion toolset was developed specifically for this study. A photograph of the toolset and a sectional view of its design are shown in Figure 5.3 and Figure 5.4, respectively. The toolset consists of two main subassemblies: the upper assembly, which holds the punch and the lower assembly, which contains the die and the ejector.

Figure 5.3: Photograph of the backward micro-extrusion toolset.

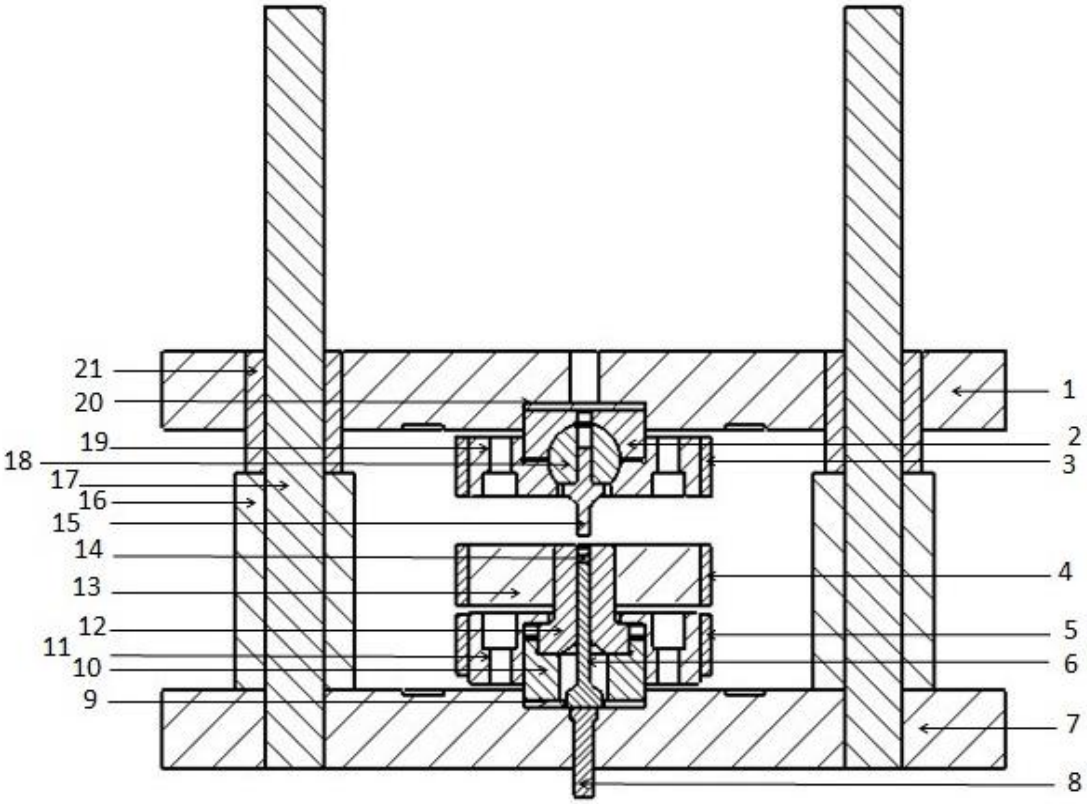

No.	Component	No.	Component
1	Upper plate	12	Die
2	Punch support	13	Die stress ring
3	Punch holder heater	14	Pellet
4	Die ring heater	15	Punch
5	Die holder heater	16	Spring stopper
6	Ejector	17	Guide pillar
7	Base plate	18	Punch swivel ball
8	Pin pusher	19	Punch holder
9	Ceramic plate	20	Ceramic plate
10	Die support	21	Guide bush
11	Die holder		

Figure 5.4: Sectional view of the backward micro-extrusion toolset with detailed components.

The details of the heating system are shown in Figure 5.5. Figure 5.6 shows the geometry of the die, including a small side through hole for inserting a thermocouple to measure the temperature near the deformation zone. A type K thermocouple (T1) was used for this purpose. The horizontal position of the thermocouple is approximately 1 mm from the top of the pellet, as shown in Figure 5.7. The temperature readings for both the punch holder and the die ring are taken from the inner surfaces of their respective heaters. These temperature measurements are obtained using thermocouples integrated into the heaters. The punch holder and die ring are heated with 850 W band heaters, while the power of the die holder band heater is 300 W. The temperature of the die holder heater was set at 100 °C during all experiments conducted at elevated temperatures to stabilise the temperature near the deformation zone. All heaters are manufactured by Watlow Ltd.

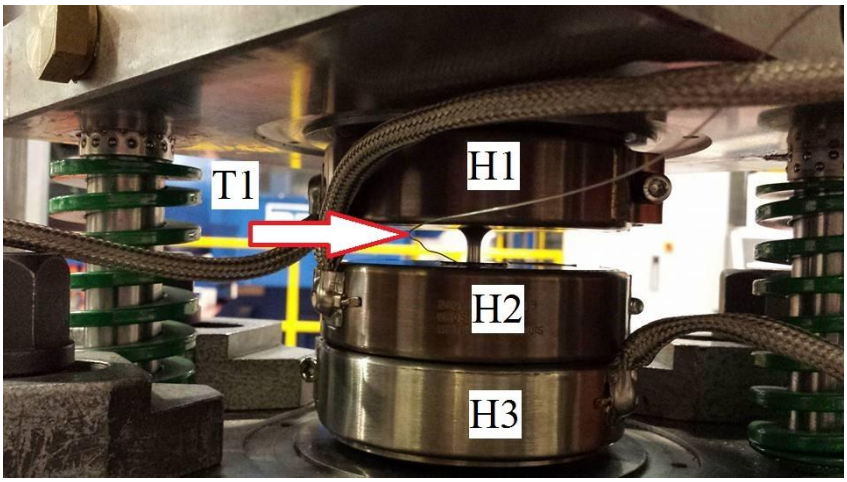

Figure 5.5: The heating elements for backward micro-extrusion toolset including punch holder heater (H1), die ring heater (H2), die holder heater (H3), and thermocouple (T1).

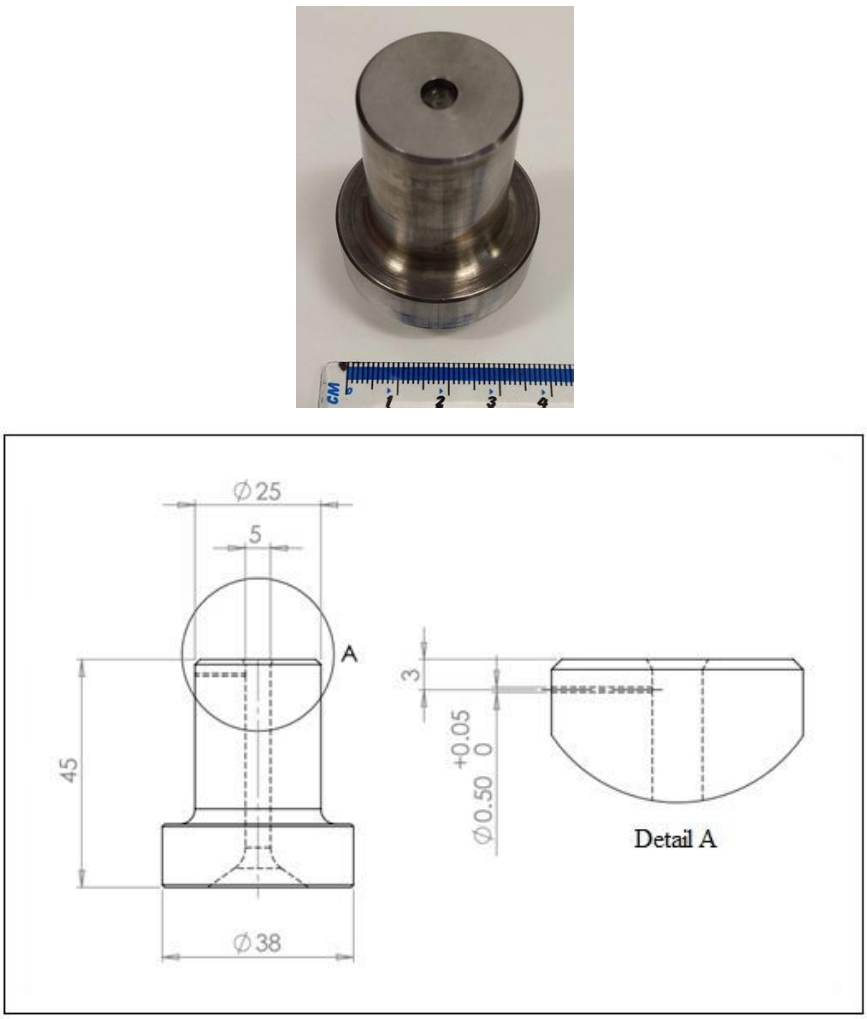

Figure 5.6: The die and the engineering drawing showing location of a thermocouple.

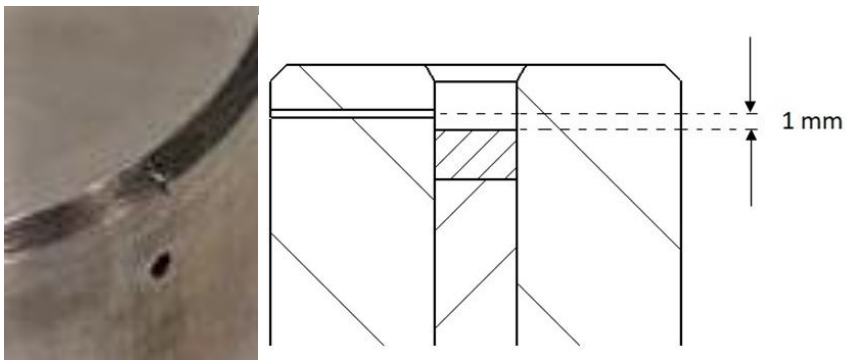

Figure 5.7: The distance between thermocouple position and top of the pellet is around 1 mm.

The pre-assembly of the backward micro-extrusion toolset is shown in Figure 5.8, where the upper and lower plates of a standard die set, supplied by Boneham & Turner Ltd, are guided diagonally by two pillars. The pillar springs are mainly used to prevent the upper plate from hitting the bottom toolset components during setup and experimentation. The die and ejector are fabricated from H13 tool steel with a hardness of 50-52 HRC. At RT, the yield strength of this material is approximately 1.5 GPa (www.matweb.com).

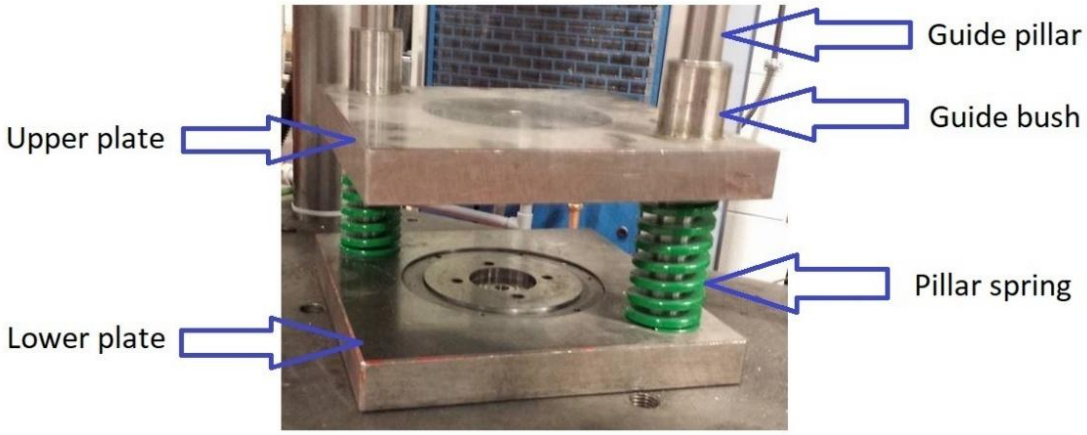

Figure 5.8: The pre-assembled backward micro-extrusion toolset provided by Boneham & Turner Ltd.

The ejector is shown in Figure 5.9. The pin pusher drives the ejector until the pellet is released from the die. The pin pusher was purchased as a standard part from Hasco company (www.hasco.com) with the product code T3040 (Z40/3 ×160). Figure 5.10 presents the detailed geometry and hardness of the pin pusher. Other components, such as the die support, die holder, die stress ring, punch holder, and punch support, are shown in Figure 5.11.

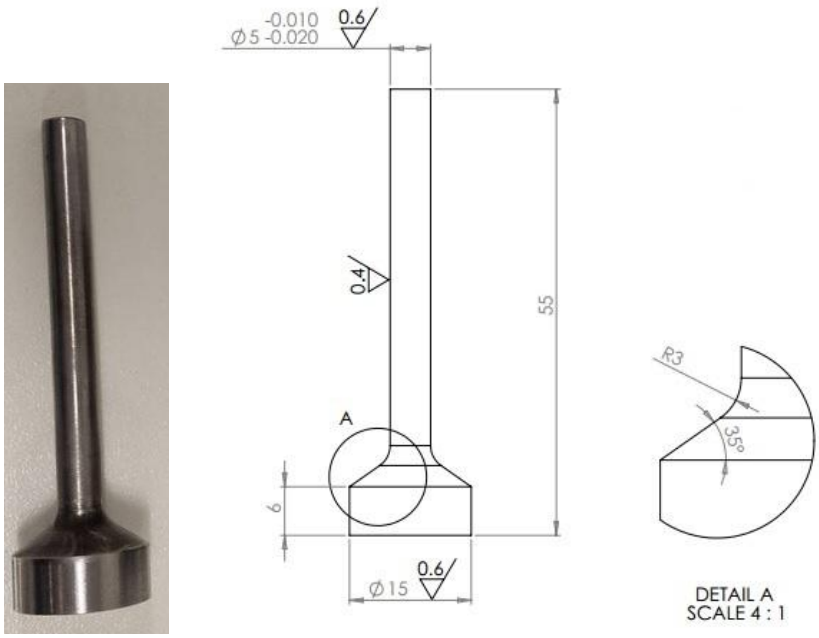

Figure 5.9: The ejector.

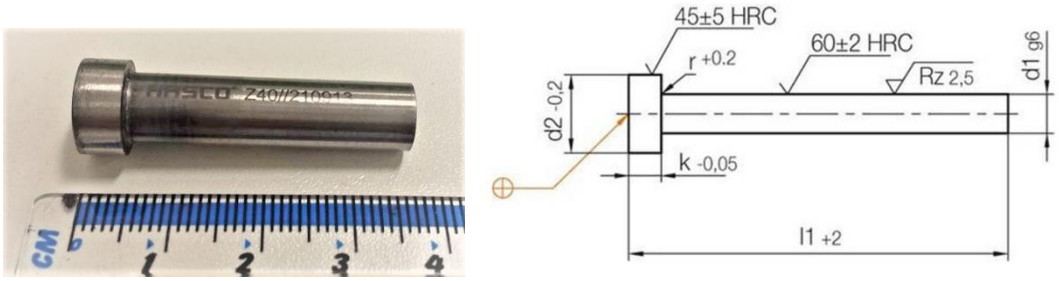

Figure 5.10: Standard pin pusher (Z40/3 ×160) from Hasco.

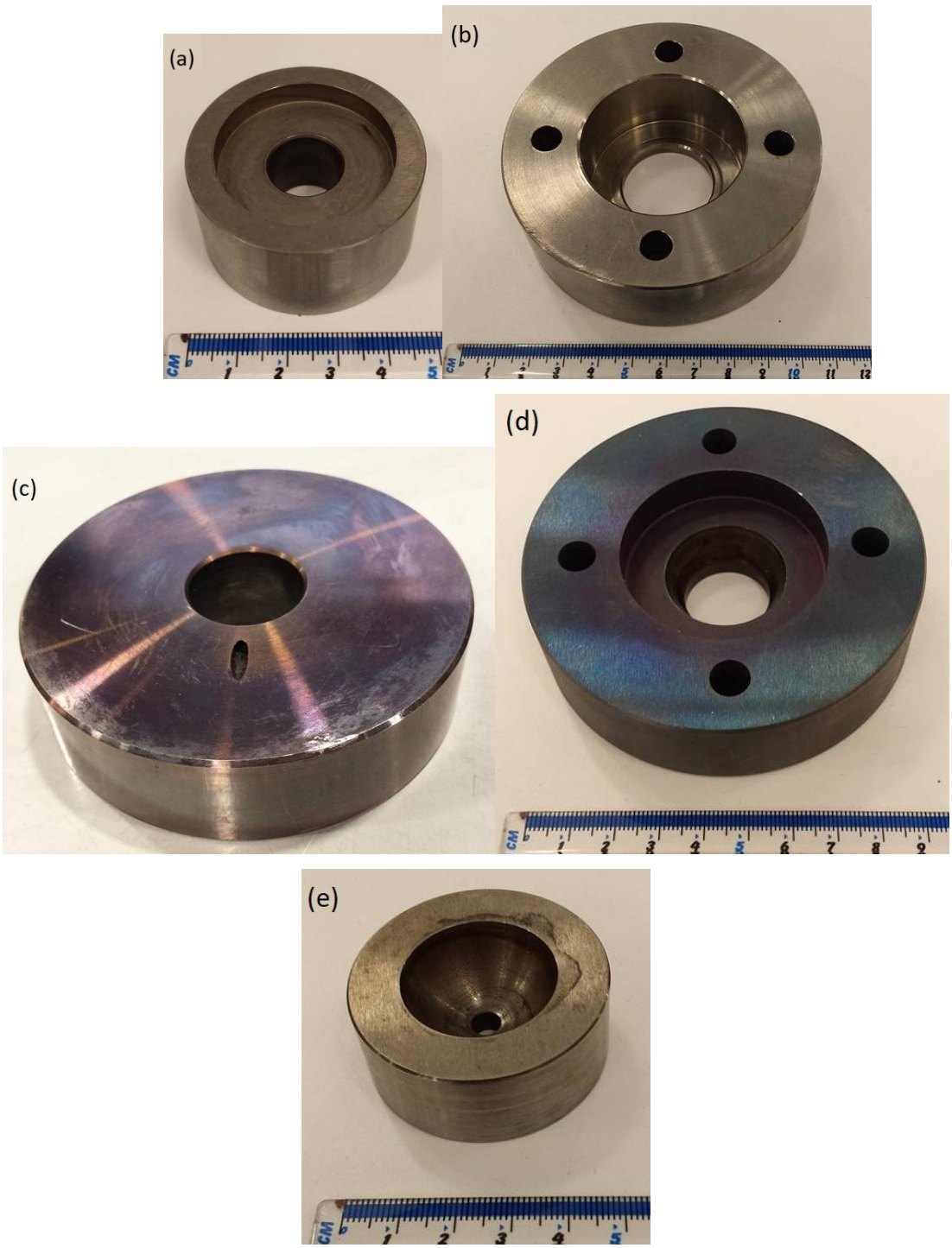

Figure 5.11: Die support (a), die holder (b), die stress ring (c), punch holder (d), and punch support (e).

Rosochowska et al. (2010) studied the process of micro-extrusion of an Al 1070 single conical pin using the finite element code ABAQUS/Explicit. Their study focused on the relationship between the conical pin cavity design and material flow. The proposed design is characterised in Figure 5.12 with the introduction of an angle 90º-α, called the pin angle. The results concluded that increasing the pin angle from 5˚ to 10˚ or 15˚ could reduce the extrusion force. Similar simulation results were published by Salamati and Rosochowski (2014) for the case with multi-pin cavities. A larger pin angle should also facilitate the removal of pins from the punch. Therefore, the geometry of the conical pin cavity is based on this research. The geometry of the punch is shown in Figure 5.13, as designed by Salamati (2018). The punch is made of Vanadis 23, a chromium-molybdenum-tungsten-vanadium alloyed high-speed steel. At a hardness of 55 HRC, the compressive yield strength at RT is approximately 1.6-1.8 GPa (www.matweb.com).

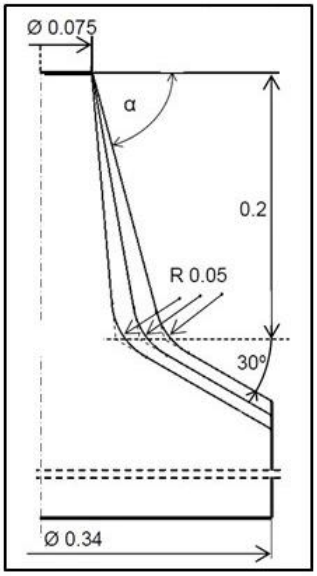

Figure 5.12: The proposed geometry of the conical pin cavity (Rosochowska et al., 2010).

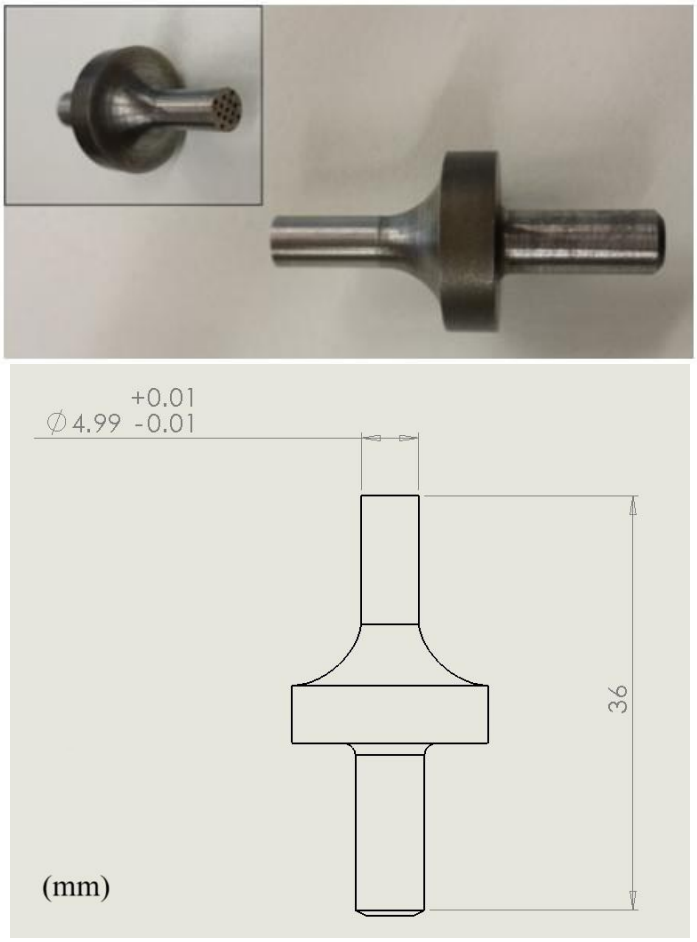

Figure 5.13: The geometry of conical pin punch (Salamati, 2018).

Punch swivel ball (Figure 5.14) is made of grade 100 hardened AISI 420 stainless steel ball bearings purchased from Simply Bearing Ltd Company (https://simplybearings.co.uk/shop/). The hardness and tensile strength are approximately 52-55 HRC and 1.9 GPa, respectively. Figure 5.15 shows the punch inserted into the swivel ball before being assembled with the punch holder. The purpose of the punch swivel ball is to ensure that the alignment angle between the punch and the die hole is correct by allowing a small degree of free movement of the punch during the toolset setup.

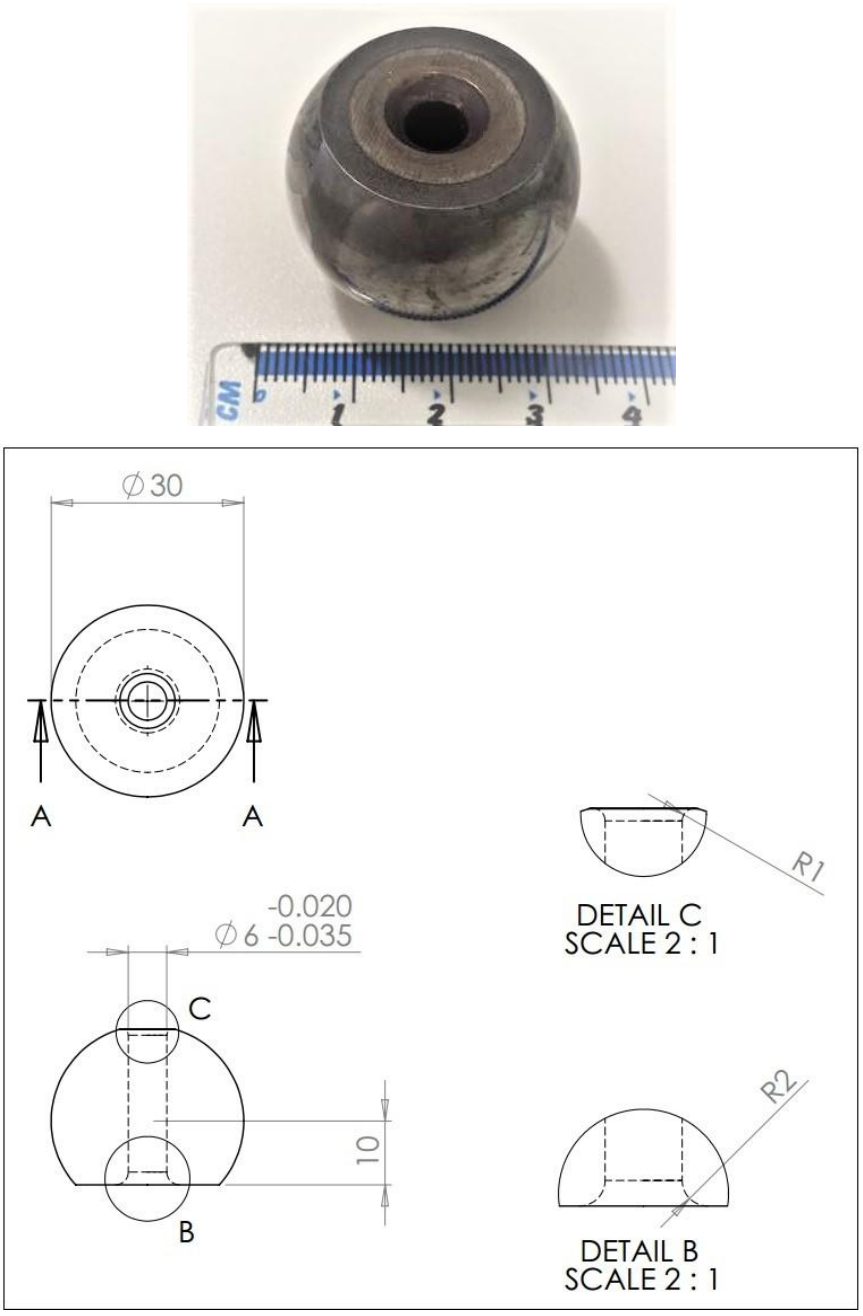

Figure 5.14: Punch swivel ball.

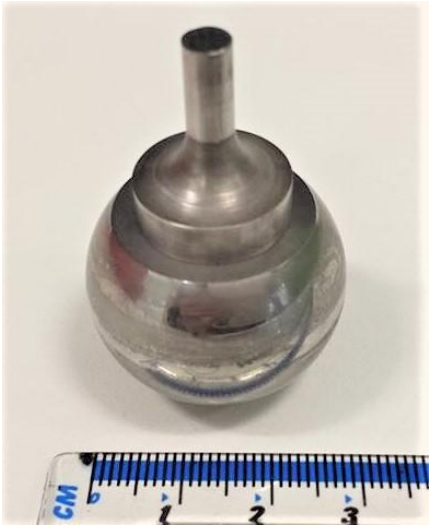

Figure 5.15: The punch inserted in the swivel ball.

Backward micro-extrusion was performed on a 25-ton laboratory press, where the movement of the punch is controlled by a hydraulic actuator attached to a fixed crosshead plate of the press, as shown in Figure 5.16. A schematic illustration of the control system for backward micro-extrusion is shown in Figure 5.17. The operation of backward micro-extrusion is controlled by the Cubus software from ZwickRoell, with Figure 5.18 showing the software's interface. The displacement transducer controls the movement of the hydraulic actuator through a signal received by the servo valve from the Cubus software. A load cell measures the force on the punch during the extrusion process.

The toolset consists of three zones for heating elements, namely the punch, the die, and the bottom clamping. The temperature controller is used to control the temperature in each zone. After completing the backward micro-extrusion experiment, the workpiece, in the form of a pellet (more information about the pellet is given in Subchapter 5.2.4), is ejected by a small hydraulic actuator located under the press table and manually controlled via a hydraulic pump.

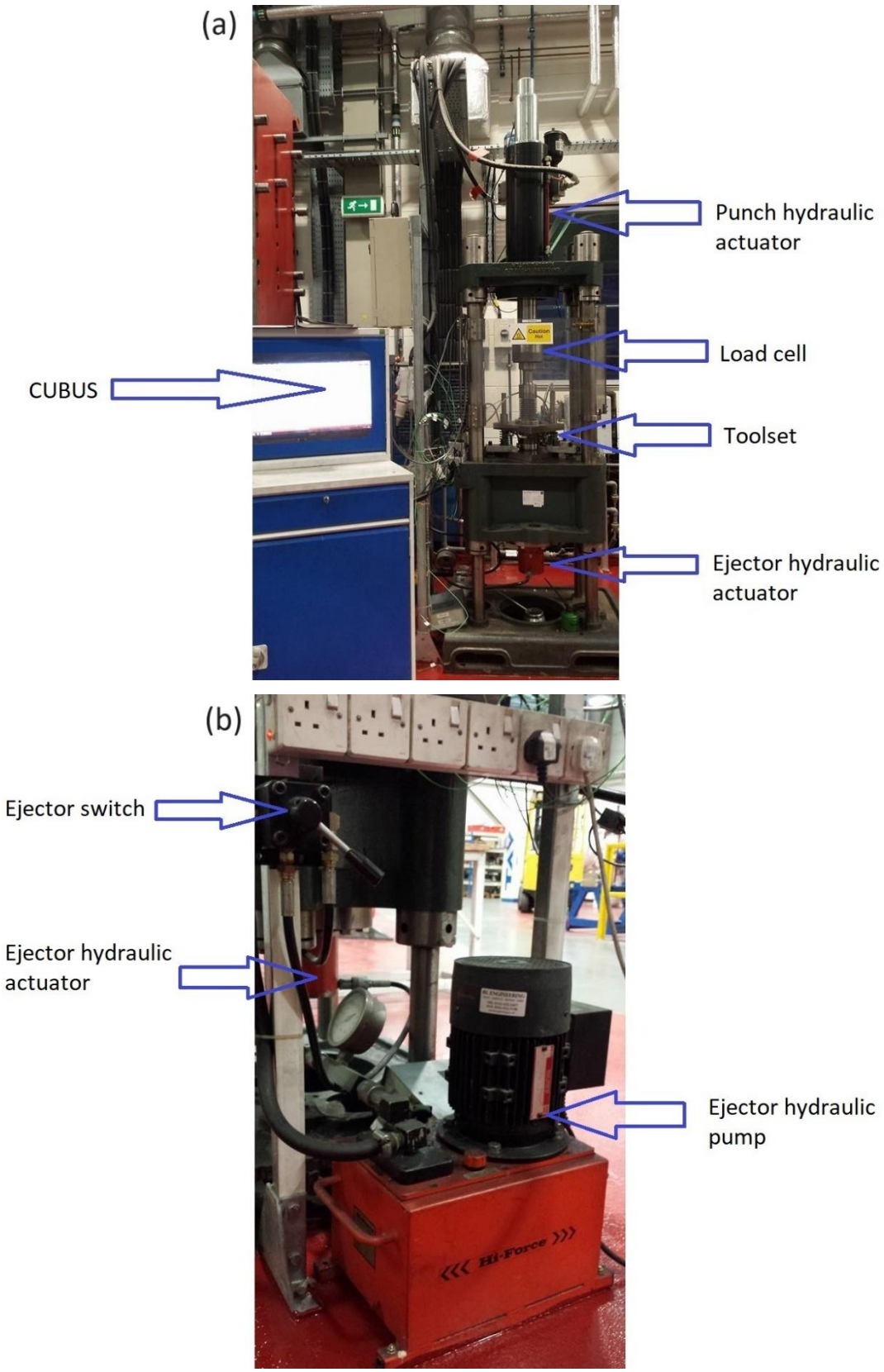

Figure 5.16: Backward micro-extrusion performed on the 25-ton hydraulic press. Front view (a), and left side view (b).

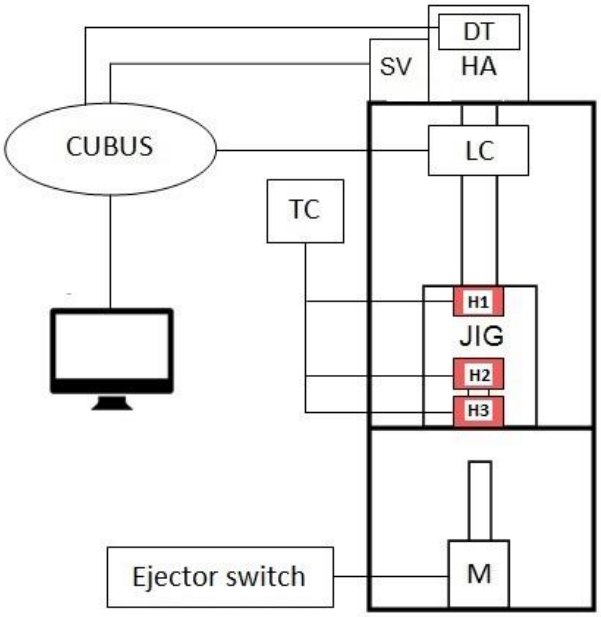

Symbol	Name
HA	Hydraulic actuator
LC	Load cell
TC	Temperature controller
M	Hydraulic pump
SV	Servo valve
DT	Displacement transducer
H1	Punch holder heater
H2	Die ring heater
H3	Die holder heater

Figure 5.17: Schematic of a control system for backward micro-extrusion.

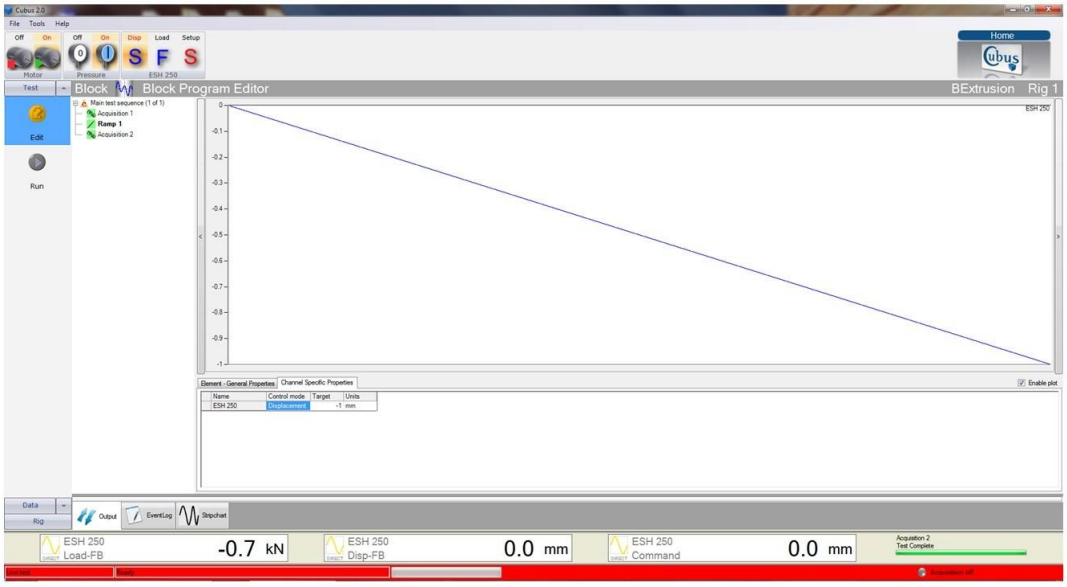

Figure 5.18: Cubus user interface, which controls the backward micro-extrusion process.

5.2.3 Conical Pin Cavity

The optical microscope (InfiniteFocus, Figure 5.19) used in this study is a non-contact measurement device that works on the principle of focus variation. It employs vertical scanning to capture surface data and generate a 3D model.

The microscope supports magnifications of up to 50×, with a vertical resolution of approximately 10 nm and a measurable roughness of 0.03 µm. The lowest magnification, 2.5×, was used to capture overall object images. During measurement, the specimen is placed on the stage and secured using Blu-Tack. The stage moves along the x- and y-axes, while the head holding the objective lens moves along the z-axis to scan and measure the regions of interest during an automatic scan. After a 3D image has been generated, the coordinate position is set by manually selecting three points to level the top surface of the object before measurement. This step ensures accuracy for each specimen. The microscope is calibrated monthly by a technician.

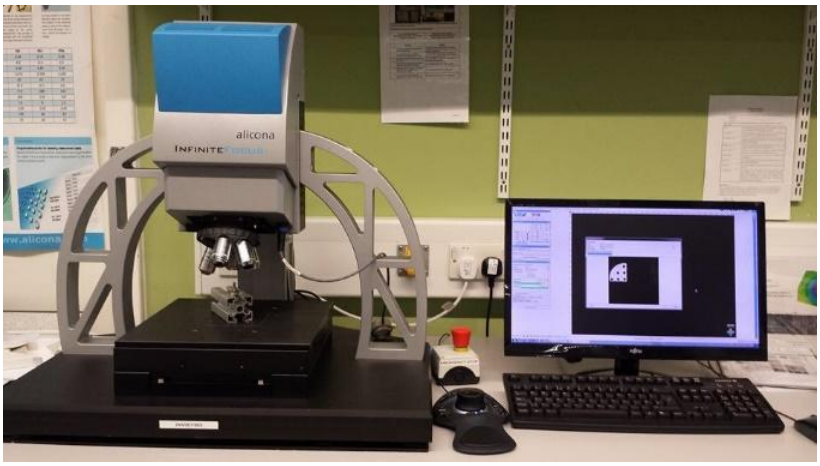

Figure 5.19: Non-contact optical microscope (InfiniteFocus).

Figure 5.20a shows a scanned image of the top surface of the pellet, with a red straight line crossing the selected conical pins. The corresponding profile results for the selected pins are illustrated in Figure 5.20b. The 3D scan image can also be displayed using a colour scheme, where the colour scale legend represents the surface topography, as shown in Figure 5.21 and Figure 5.22.

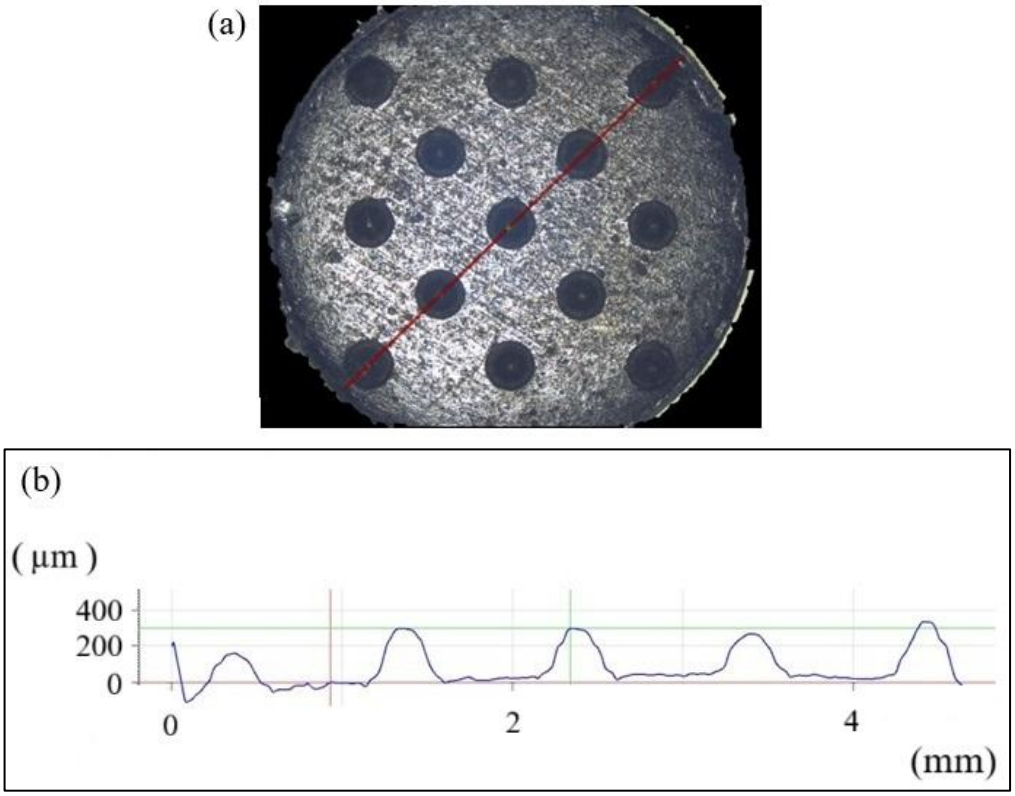

Figure 5.20: Microscope results: top view of conical pins with a red selection line (a), and profile of the selected conical pins (b).

The multipin conical cavities in the punch were fabricated using laser technology. A DMG Mori Lasertech 40 machine at Cardiff University (courtesy of Dr. Samuel Bigot) was used to create microcavities on the punch face. This machine employs a fibre laser source with an output of 20/50/100 W and is capable of producing a fine laser spot with diameters ranging from 0.03 mm to 0.04 mm. Figure 5.21 shows the punch face with microcavities produced by laser ablation, while Figure 5.22 presents the reverse view, which reveals the profile and depth of the individual pin cavities as captured and measured by the microscope.

There are 13 conical pin cavities arranged in five rows, based on a design by Salamati (2018). The details of each cavity profile and depth are shown in Figure 5.23 and 5.24, respectively. The base diameter of each cavity is approximately 0.4 mm, and the distance between their axes is about 1 mm. The laser process produced relatively rough cavity profiles. Microscope results revealed variations among the cavities, with cavity number five having the lowest depth. Accuracy and surface finishing of extrusion tools are common challenges in microforming. The rough surfaces of the pin cavities can affect the quality of the extruded pins, while variations in cavity depth make it impossible to study the effect of pin positioning on pin height.

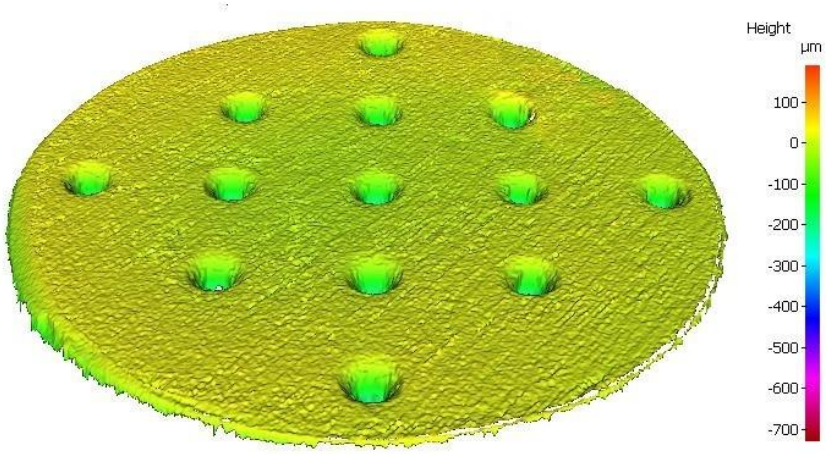

Figure 5.21: View of the punch face with conical pin cavities captured by microscope.

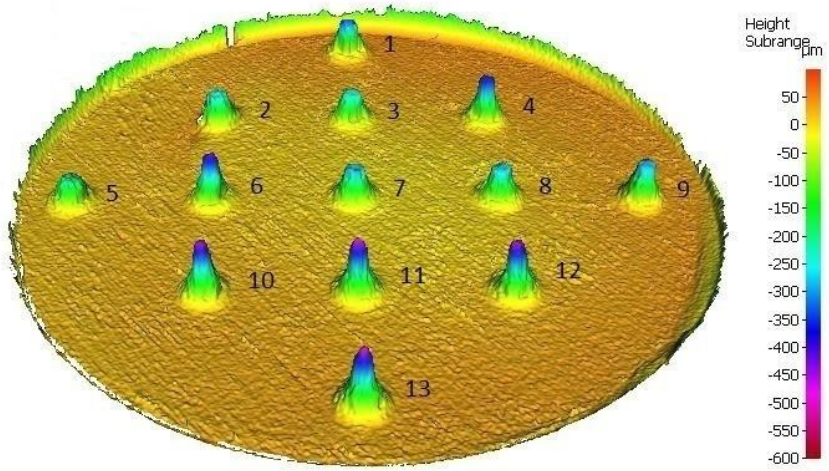

Figure 5.22: Reverse view of the punch face with conical pin cavities captured by microscope.

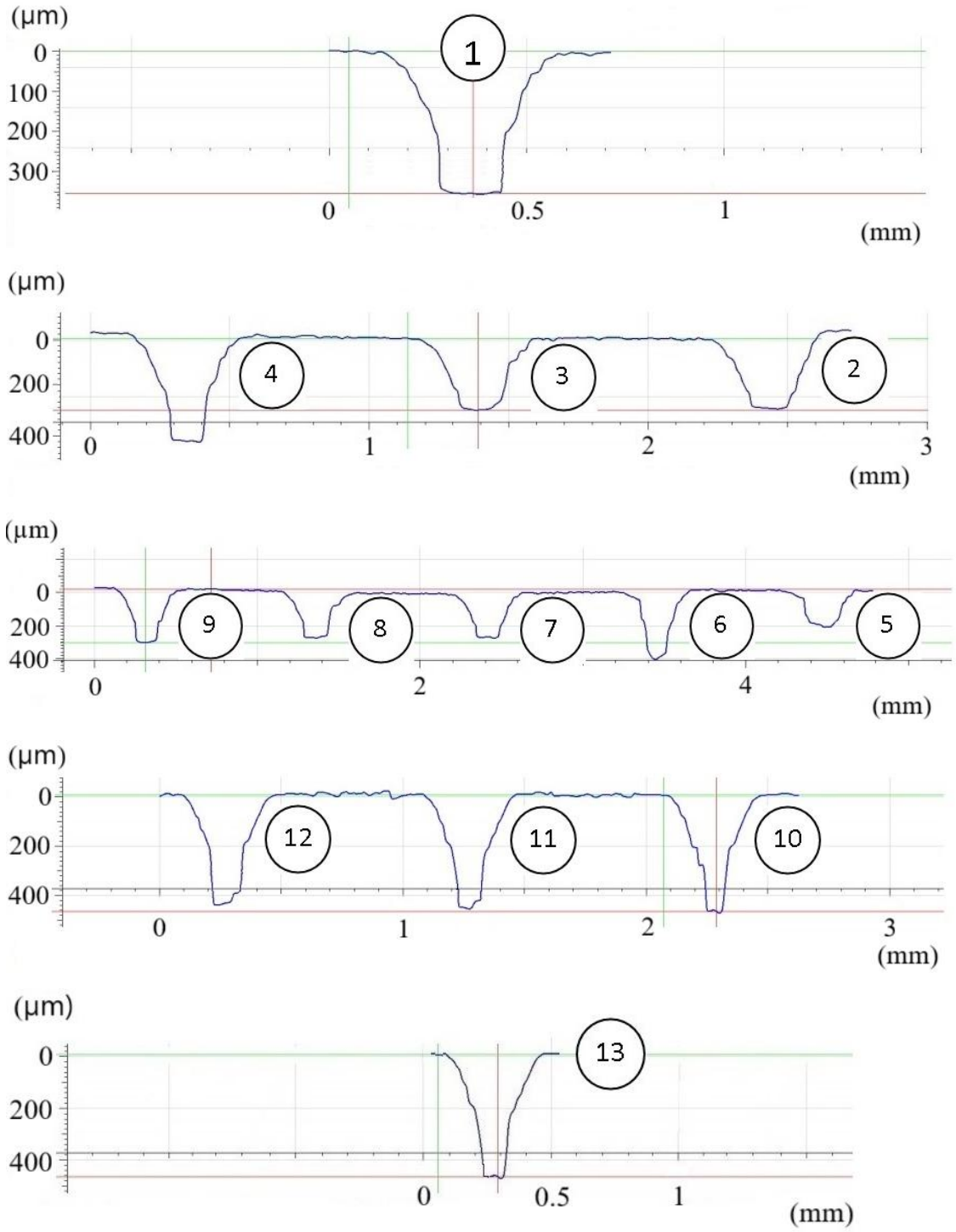

Figure 5.23: Cross-sectional profiles of all conical pin cavities measured using a microscope.

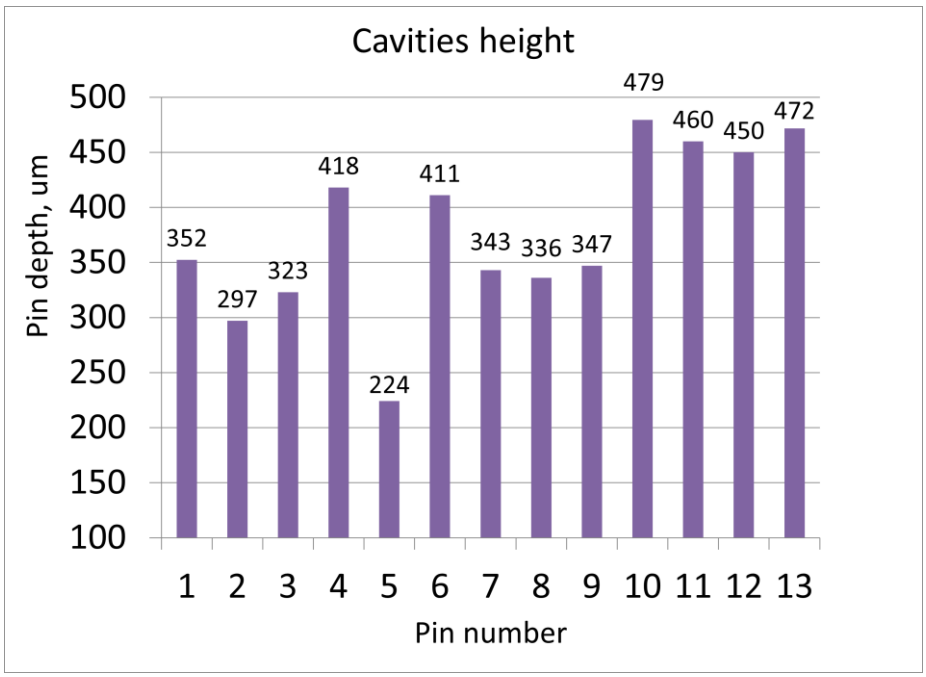

Figure 5.24: Measured depths of conical pin cavities.

5.2.4 Pellet

The final product in the form of a small array of miniature conical pins was produced using a small cylindrical part called a pellet. The material for the pellet is made of Aluminium 5083. Figure 5.25 shows the geometrical design of the pellet, 5 mm diameter and 3 mm height, with the pellet axis aligned with the rolling/extrusion direction as illustrated in Figure 5.26.

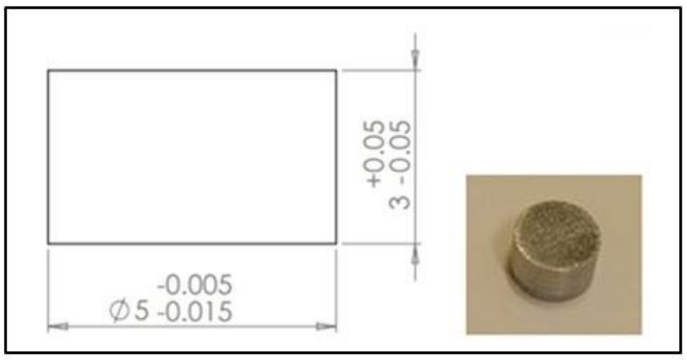

Figure 5.25: The geometrical design of the pellet and its real product.

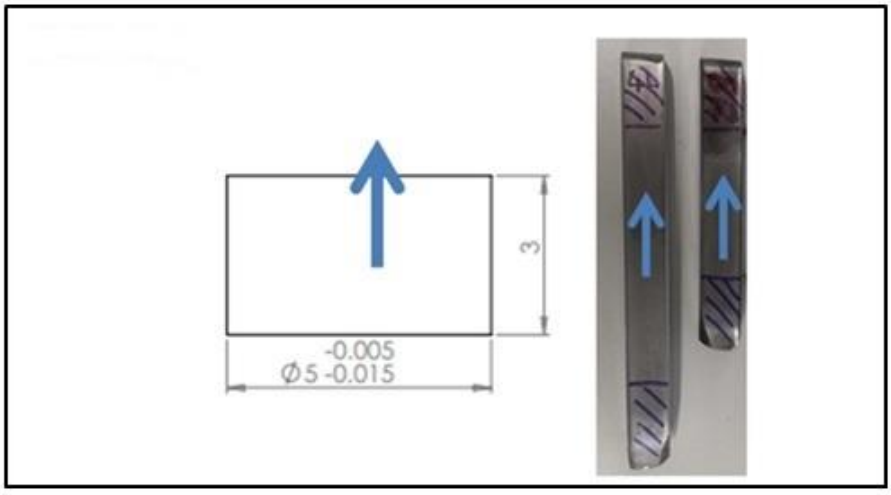

Figure 5.26: The pellet cut out along the rolling/extrusion direction.

5.2.5 Backward Micro-Extrusion Parameters

The process parameters for backward micro-extrusion are the die/punch temperature, punch displacement, and process duration. The punch displacement and the process duration were set using the Cubus software, as shown in Figure 5.27, with values of 1 mm and 200 s.

The displacement value of 1 mm was chosen with reference to the work of Salamati (2018), who successfully produced conical pins through backward micro-extrusion of UFG Al 1050 at room temperature using a displacement of 2 mm. In comparison, the yield strength of UFG Al 1050 after eight passes is approximately 200 MPa, whereas the compression yield strength of UFG Al 5083 after eight passes at 200 °C is about 130 MPa (Figure 4.24). Based on this comparison, a displacement of 1 mm was selected for the present trials.

To carry out the backward micro-extrusion experiment, the pellet was placed in the die and rested on top of the ejector. Lubricant was not used, as there was a risk it could become trapped in the punch cavities and block the flow of material. After the punch contacted the pellet, a waiting time of 10 minutes was applied to ensure uniform temperature distribution within the pellet by heat conduction from the die and the punch.

The initial experiments were intended for establishing a suitable punch displacement. They were performed for 8P material extruded at 250 °C, and the process duration was 300 s using two punch displacements, 0.5 mm and 1 mm.

The Quanta FEG 250, shown in Figure 5.28, is an SEM machine used to take images of the objects after the backward micro-extrusion experiment, as shown in Figure 5.29. This device can achieve a resolution of 1.4 nm with a maximum magnification of 1,000,000×.

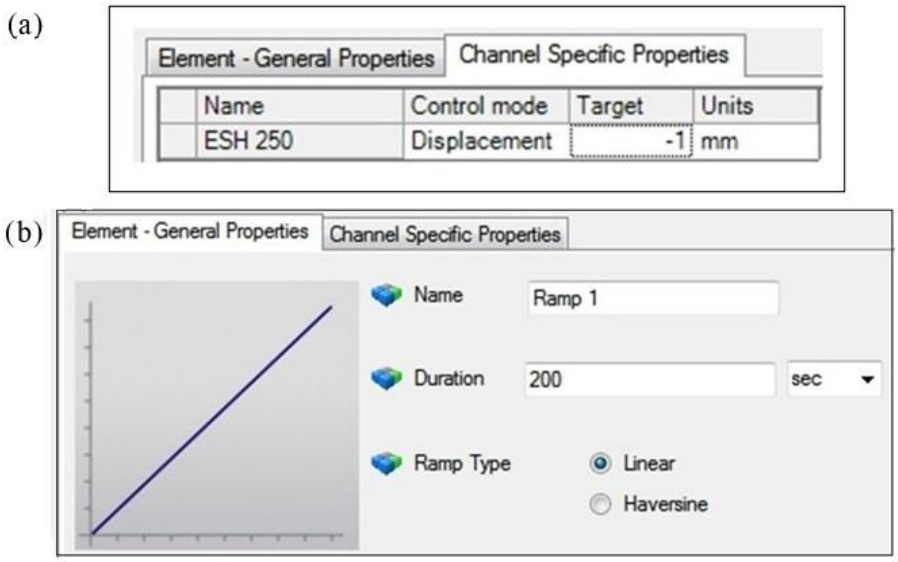

Figure 5.27: Examples of input values in the Cubus software for punch displacement (a), and process duration (b).

Figure 5.28: The Quanta FEG 250 SEM.

Figure 5.29 and 5.30 show the SEM and microscope results for these experiments, and Figure 5.31 shows the graph of the conical pin heights for each pin as compared to the pin cavity height. Not surprisingly, most of the conical pins for 1 mm punch displacement are higher than those obtained for 0.5 mm punch displacement, except for the pin number three and five, which have similar heights for both punch displacements. It is expected that most of the conical pins formed with a 1 mm punch displacement are taller than those produced with a 0.5 mm displacement. A greater punch movement pushes more material into the cavities, allowing the pins to fill deeper and reach a higher height. In comparison, the smaller 0.5 mm displacement does not provide enough material flow, leading to shorter pins.

The average conical pin height for the punch displacement of 0.5 mm was 257 μm. It reached a higher value of 328 μm for the punch displacement of 1 mm. The percentage increase in the average conical pin height was around 28% rather than 100%, which represents less than a proportional rise due to material "loss" caused by a larger flash created between the die and the punch for 1 mm displacement.

Despite the less efficient material flow for 1 mm punch displacement, the initial trial of 0.5 mm punch displacement was insufficient to fill the cavities and produce pins of adequate height. The researcher concluded, based on experimental evidence, that 0.5 mm punch displacement was not suitable. However, a punch displacement greater than 1 mm may result in significantly higher process force and tool contact pressure since many pins made with a 1 mm punch displacement reached heights that were near to the pin cavity height. Thus, the punch displacement of 1 mm was used in all further experiments. Figure 5.32 shows the top SEM view of pin number seven, obtained in the initial experiment described above; the pin base diameter was almost 0.5 mm, while the top diameter was 0.12 mm.

The states of the material formed, and the details of the process parameters are shown in Table 5.1. To determine the effect of process parameters on the height of the conical pins, experiments were performed at RT and at two elevated temperatures (200 °C and 250 °C), with the process duration reduced to 200 s to improve production time.

Table 5.1: Backward micro-extrusion process parameters.

State of material	Die/Punch temperature, °C	Punch displacement, mm	Process duration, seconds
CG, 4P, 8P	RT / 200 / 250	1.0	200

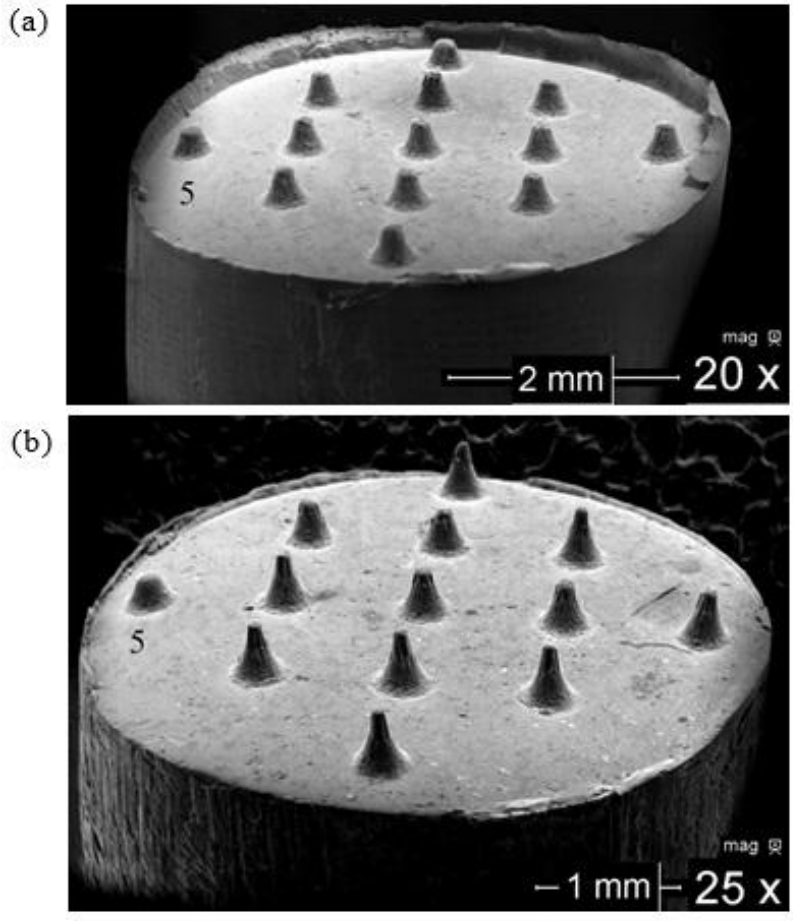

Figure 5.29: SEM images of 8P material extruded at 250 °C during 300 s using punch displacement of 0.5 mm (a), and 1 mm (b).

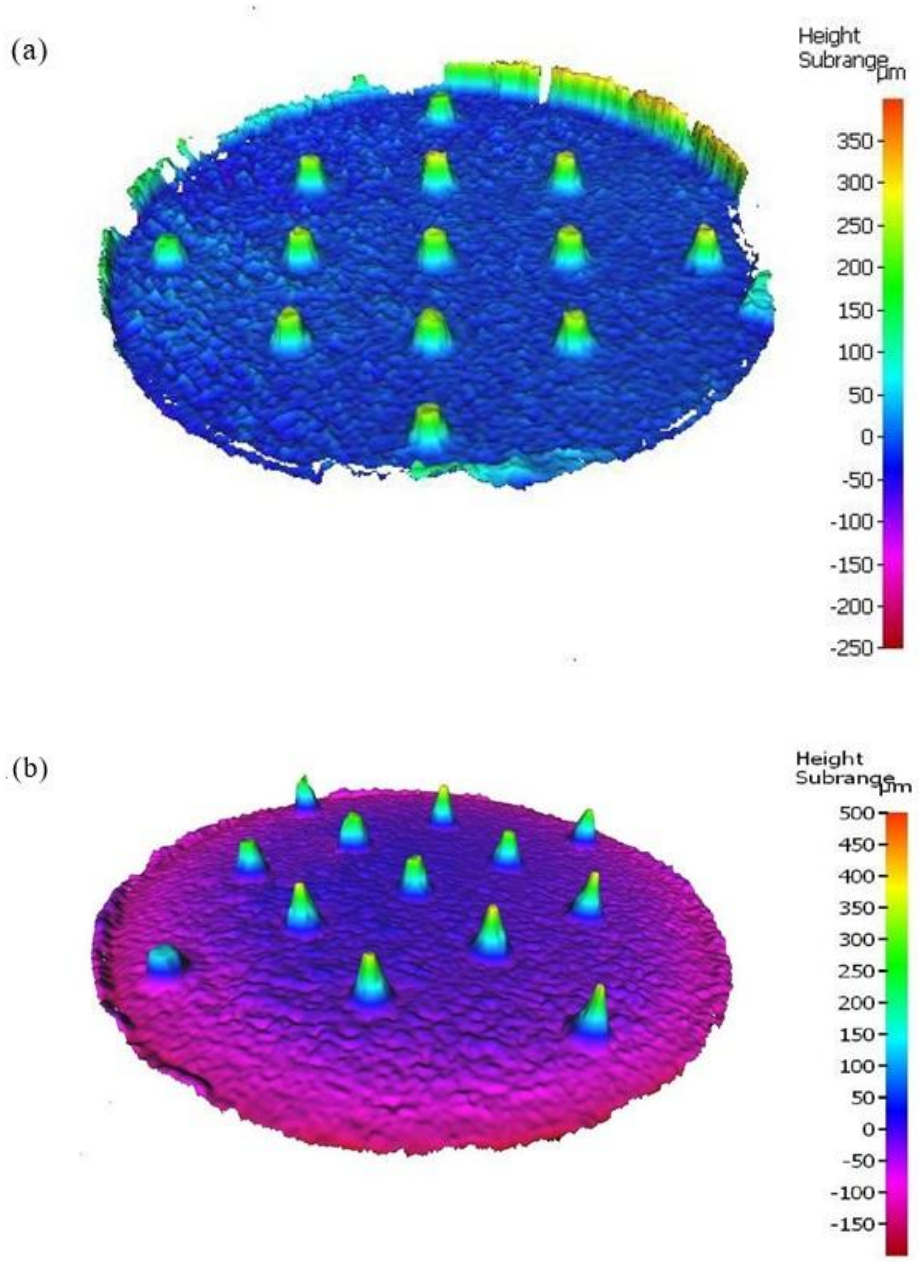

Figure 5.30: Microscope images of 8P material extruded at 250 °C during 300 s using punch displacement of 0.5 mm (a), and 1 mm (b).

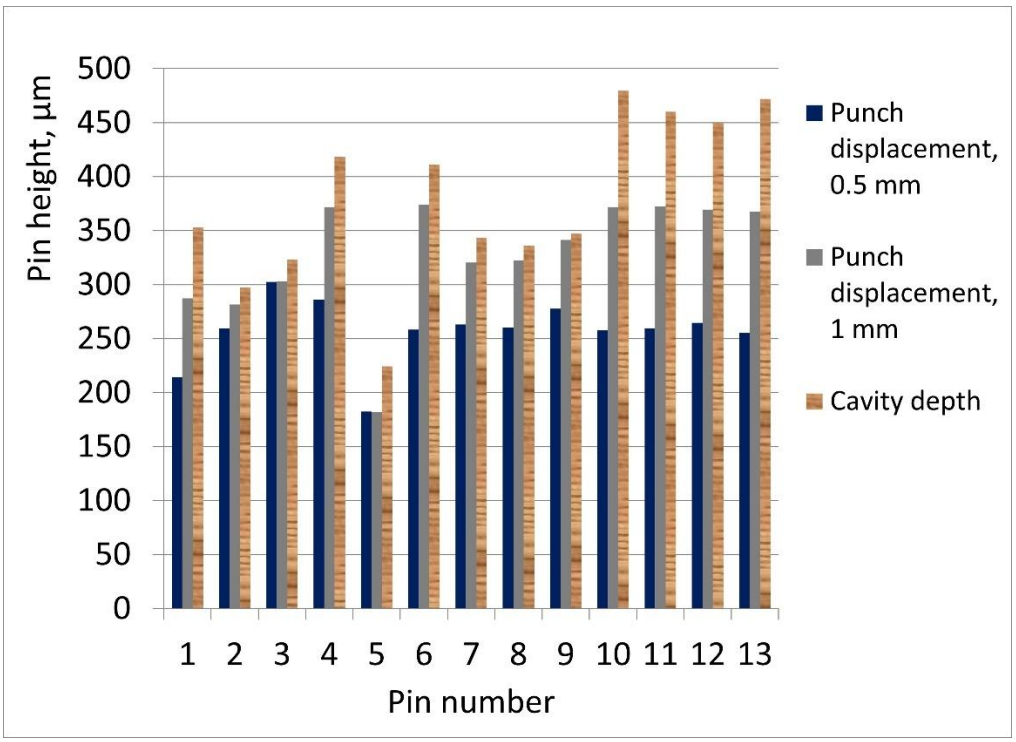

Figure 5.31: Comparison of cavity heights to pin heights attained using backward micro-extrusion of 8P material at 250 °C over 300 seconds for punch displacements of 0.5 mm and 1 mm.

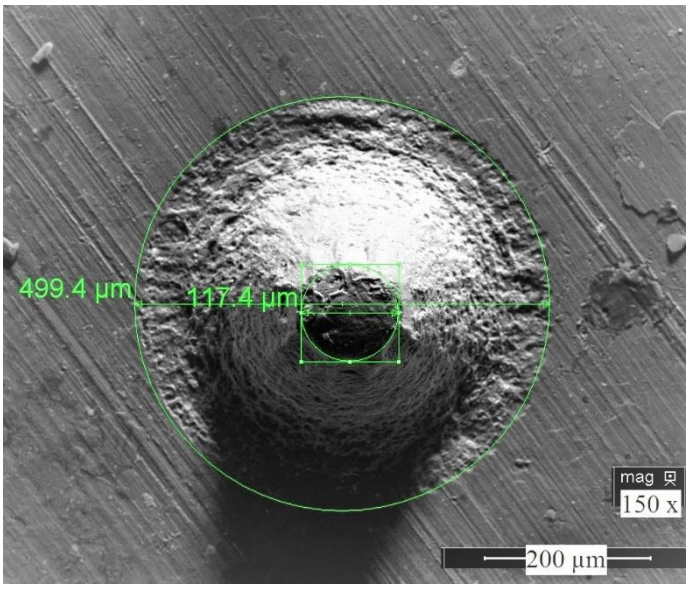

Figure 5.32: The top SEM view of pin number seven obtained by 1 mm punch displacement backward micro-extrusion of 8P material at 250 °C for 300 seconds.

5.3 Results of Backward Micro-Extrusion Experiment

5.3.1 Height of Conical Pins at RT

All the experimental results reported hereafter were obtained for the backward micro-extrusion process with a nominal punch displacement of 1 mm and a process duration of 200 s. Using these conditions and at RT for all three materials (CG, 4P, and 8P) resulted in forming only short protrusions rather than fully developed conical pins, as shown in Figure 5.33. Figure 5.34 shows the results of Microscope surface measurements using colour topography to visualise the pin height variations. Based on these results, a bar chart in Figure 5.35 was plotted for each type of material. For the CG material, the pin's height ranged from 120 μm to 175 μm; for the 4P material, it was between 50 μm and 120 μm; and for the 8P material, it was 45 μm to 105 μm. The experimental average pin heights for CG, 4P, and 8P were 147.5, 85, and 75, respectively (Table 5.2).

The CG material resulted in producing higher pins than in the case of 4P and 8P material because the yield strengths for 4P and 8P materials at RT are higher compared to CG material, making them more resistant to plastic deformation. This condition led to more deflection of the tools and reduced real punch displacement. As a result, limiting material flow into the pin cavities and leading to shorter pin formation.

Additionally, all specimens created a flash during the backward micro-extrusion. The height of the flash and pin is correlated; a shorter flash accompanies the shorter pins.

Table 5.2 : The experimental average pin heights for CG, 4P, and 8P at RT.

Material	Pin height range (μm)	Average pin height (μm)
CG	120 – 175	147.5
4P	50 – 120	85
8P	45 – 105	75

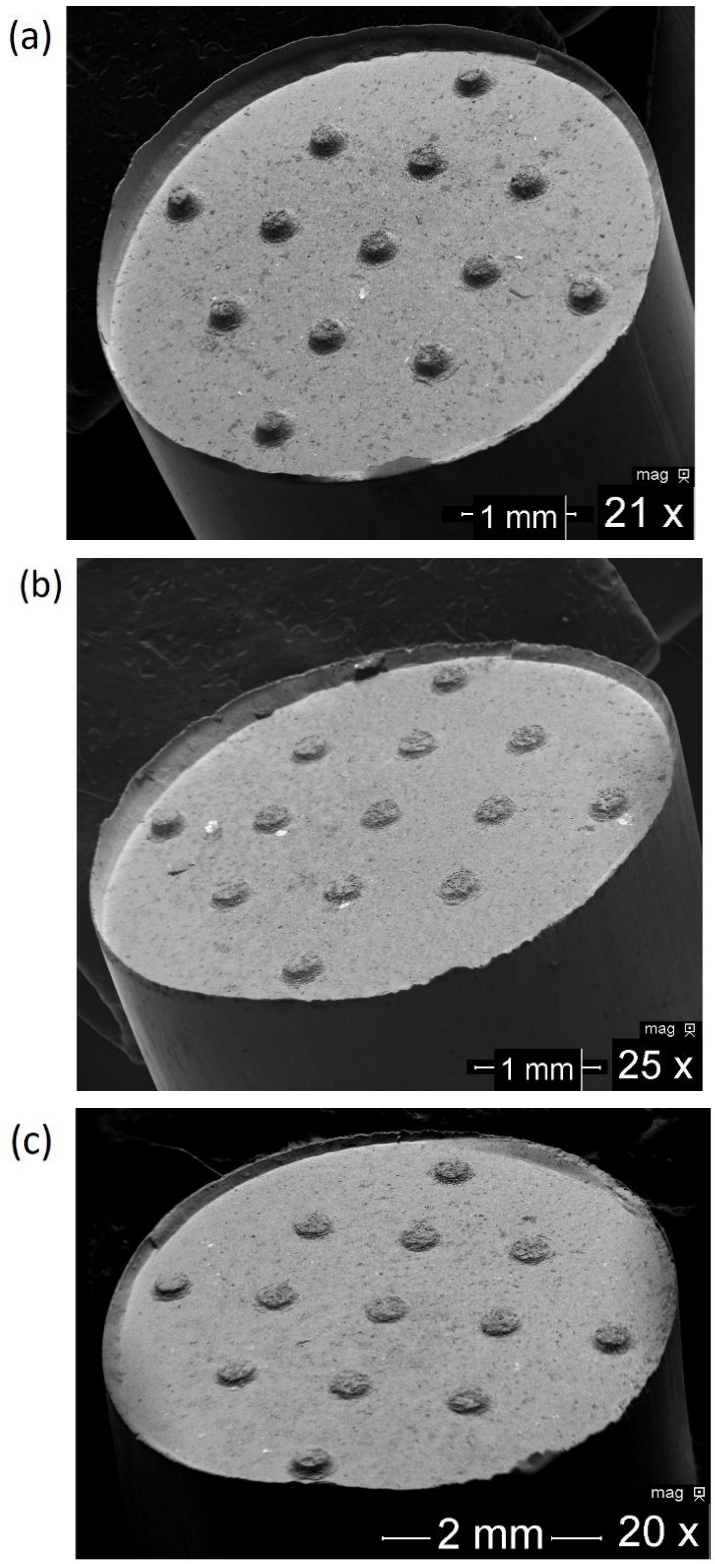

Figure 5.33: SEM images for pins extruded at RT for CG (a), 4P (b), and 8P (c) material.

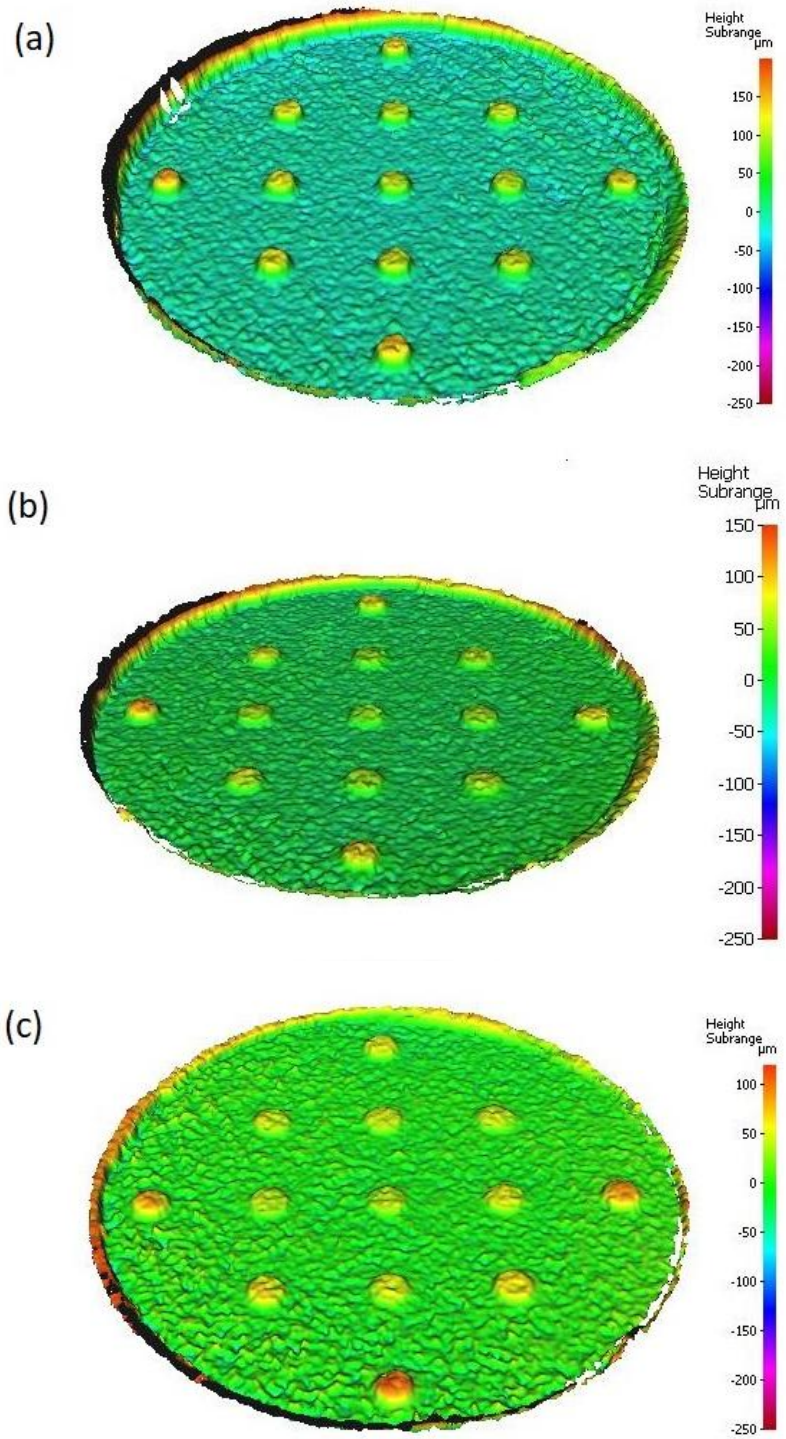

Figure 5.34: Microscope images for pins extruded at RT for CG (a), 4P (b), and 8P (c) material.

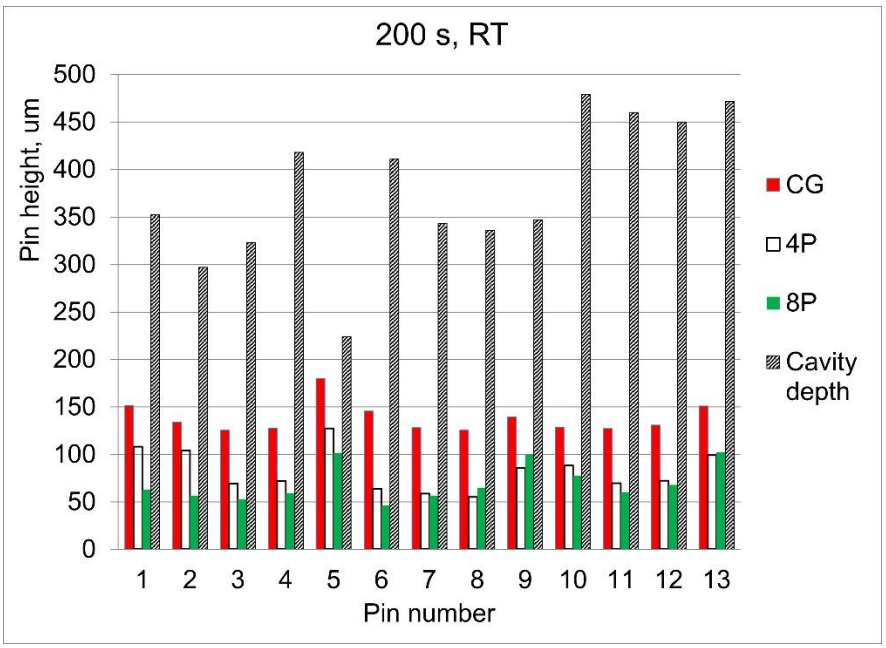

Figure 5.35: Chart of pin heights at RT for CG, 4P, and 8P materials.

5.3.2 Height of Conical Pins at 200 °C

At 200 °C, extrusion of all three materials (CG, 4P, and 8P) led to the creation of a substantial flash, as shown in Figure 5.36. This formation of flash involves several factors, including tool design precision, thermal expansion of the tool and material, and elastic deformation of tooling components during the forming process. Nevertheless, the pins formed at 200 °C are significantly higher than those formed at RT conditions. As illustrated in Figure 5.37 and the bar chart in Figure 5.38, the pin height ranges were 185 µm to 271 µm for CG, 205 µm to 288 µm for 4P, and 213 µm to 325 µm for 8P. The average pin heights at 200 °C for CG, 4P, and 8P are 228 µm, 246.5 µm, and 269 µm, respectively, as shown in Table 5.3. As summarised in Table 5.4, these results indicate a significant increase in pin height compared to the RT condition: roughly 1.6 times for CG, 2.9 times for 4P, and 3.6 times for 8P.

Unlike at RT, both 4P and 8P materials achieved higher pin heights compared to the CG material because the yield strengths for 4P and 8P materials at elevated temperatures are lower compared to CG material. As a result, the lower yield strength material allowed the punch to easily move downwards, increasing real punch displacement and resulting in higher pins.

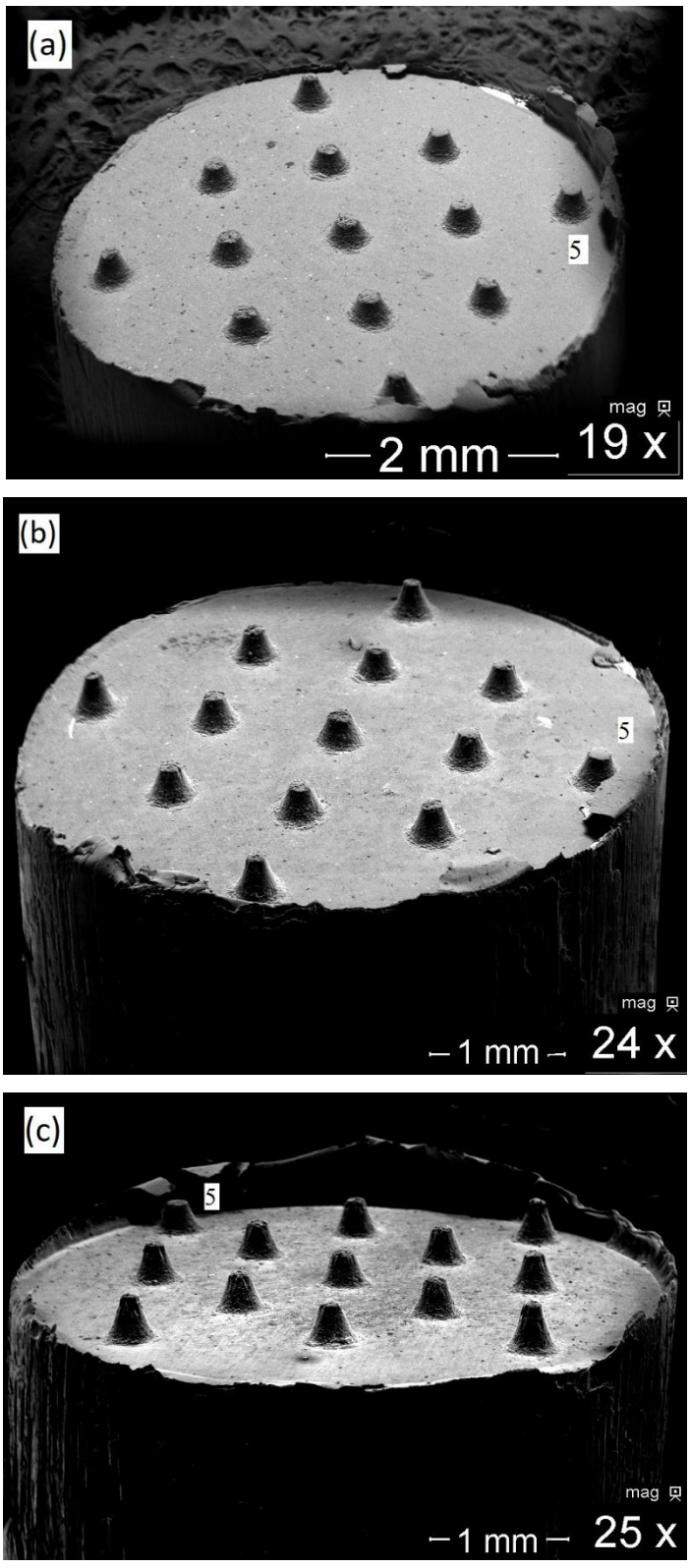

Figure 5.36: SEM images of pins extruded at 200 °C for CG (a), 4P (b), and 8P (c) material.

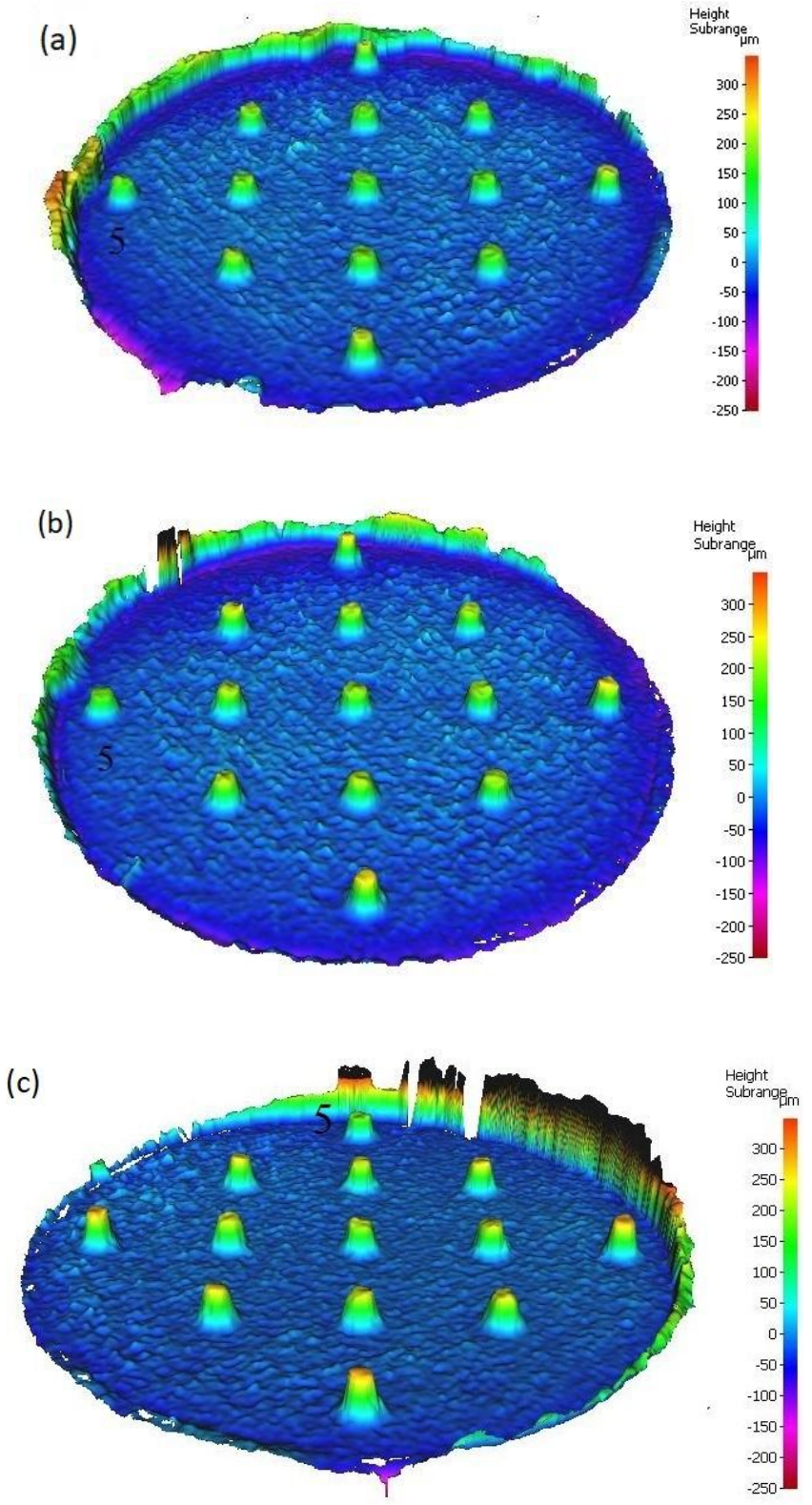

Figure 5.37: Microscope images of pins extruded at 200 °C for CG (a), 4P (b), and 8P (c) material.

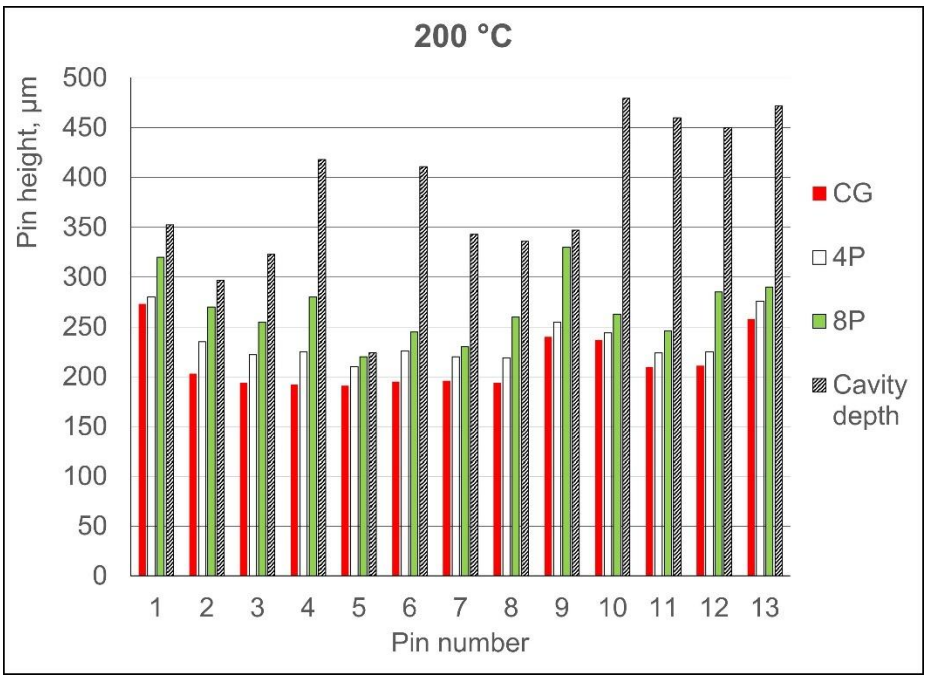

Figure 5.38: Chart of pin heights at 200 °C for CG, 4P, and 8P materials.

Table 5.3 : The experimental average pin heights for CG, 4P, and 8P at 200 °C.

Material	Pin height range (µm)	Average pin height (µm)
CG	185 – 271	228
4P	205 – 288	246.5
8P	213 – 325	269

Table 5.4 : Pin height improvement from RT to 200 °C.

Material	Average pin height at RT (µm)	Average pin height at 200 °C (µm)	Times better
CG	147.5	228	1.6x
4P	85	246.5	2.9x
8P	75	269	3.6x

5.3.3 Height of Conical Pins at 250 °C

Referring to Figure 5.39, at 250 °C, the pellets for the 4P and 8P materials were produced almost without flash, while the CG material showed an irregular flash. Clearly, the tolerance between the die, punch, and pellet has a significant effect on flash formation. Table 5.5 shows the thermal expansion coefficient for the die, punch, and pellet. Among these three components, the pellet has the highest value. This condition is related to tool expansion at elevated temperatures, which reduces the gap between the material, die, and tool diameter; therefore, it enables the control of flash shaping.

Microscope images in Figure 5.40 and the graph plotted in Figure 5.41 represent the conical pin heights for all CG, 4P, and 8P materials at 250 °C. The pin heights ranged from 285 µm to 434 µm, 299 µm to 421 µm, and 289 µm to 445 µm for CG, 4P, and 8P materials, respectively, excluding the very short cavity number five. The experimental average pin heights are 359.5 µm for CG, 360 µm for 4P, and 367 µm for 8P, as shown in Table 5.6.

The results improved by 1.6 times for CG, 1.5 times for 4P, and 1.4 times for 8P compared to the condition at 200 °C. Most pins achieved almost the full depth of their respective cavities, ranging from 80% to 100%, as shown in Table 5.8.

Table 5.5 : Thermal expansion coefficient for the die, punch, and pellet materials (www.theworldmaterial.com, www.matweb.com).

Material (Component)	Thermal Expansion Coefficient ($\times 10^{-6}$ /°C)	Temperature Range (°C)
H13 tool steel (Die)	12.2	20-425
Vanadis 23 (Punch)	11.8	20-400
Al 5083 (Pellet)	26.0	20-300

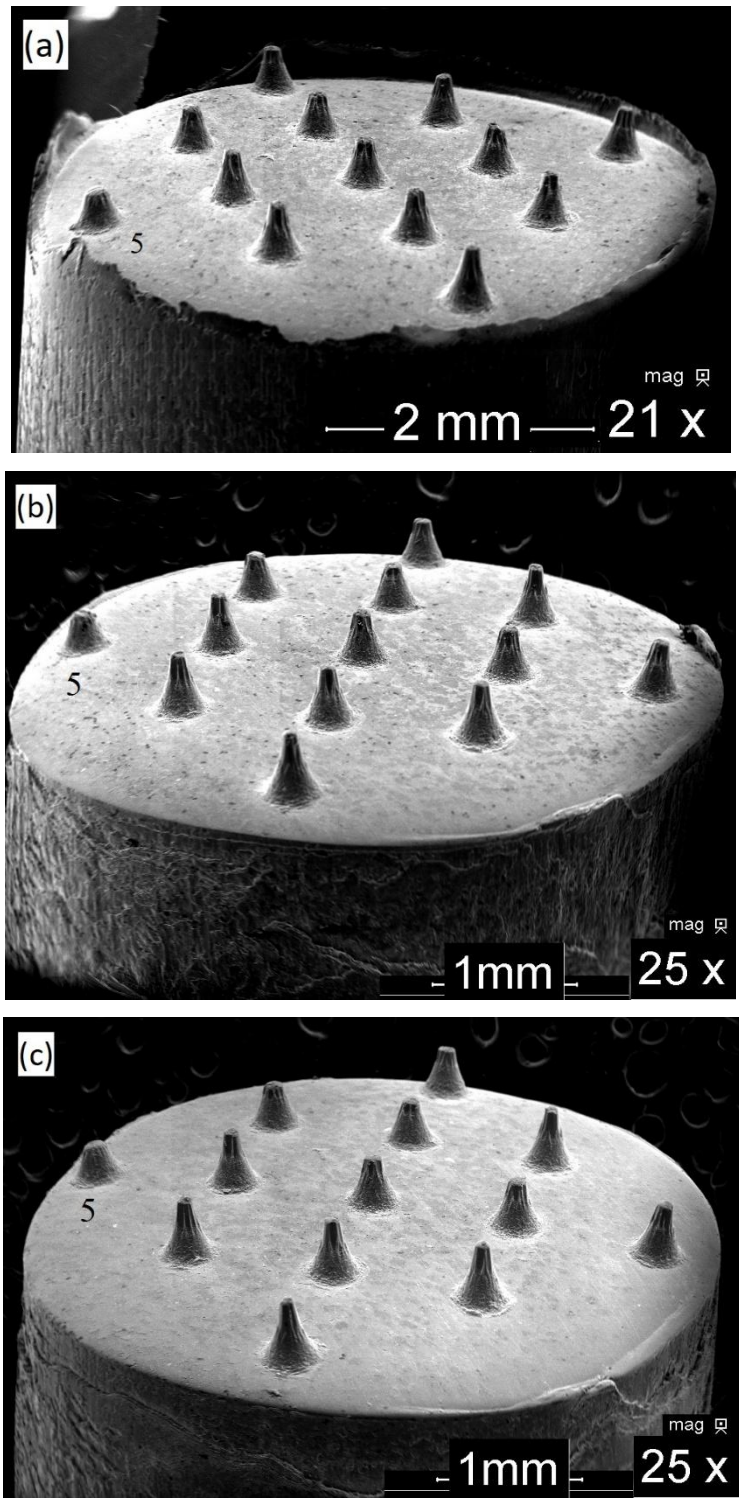

Figure 5.39: SEM images at 250 °C for CG (a), 4P (b), and 8P (c) materials.

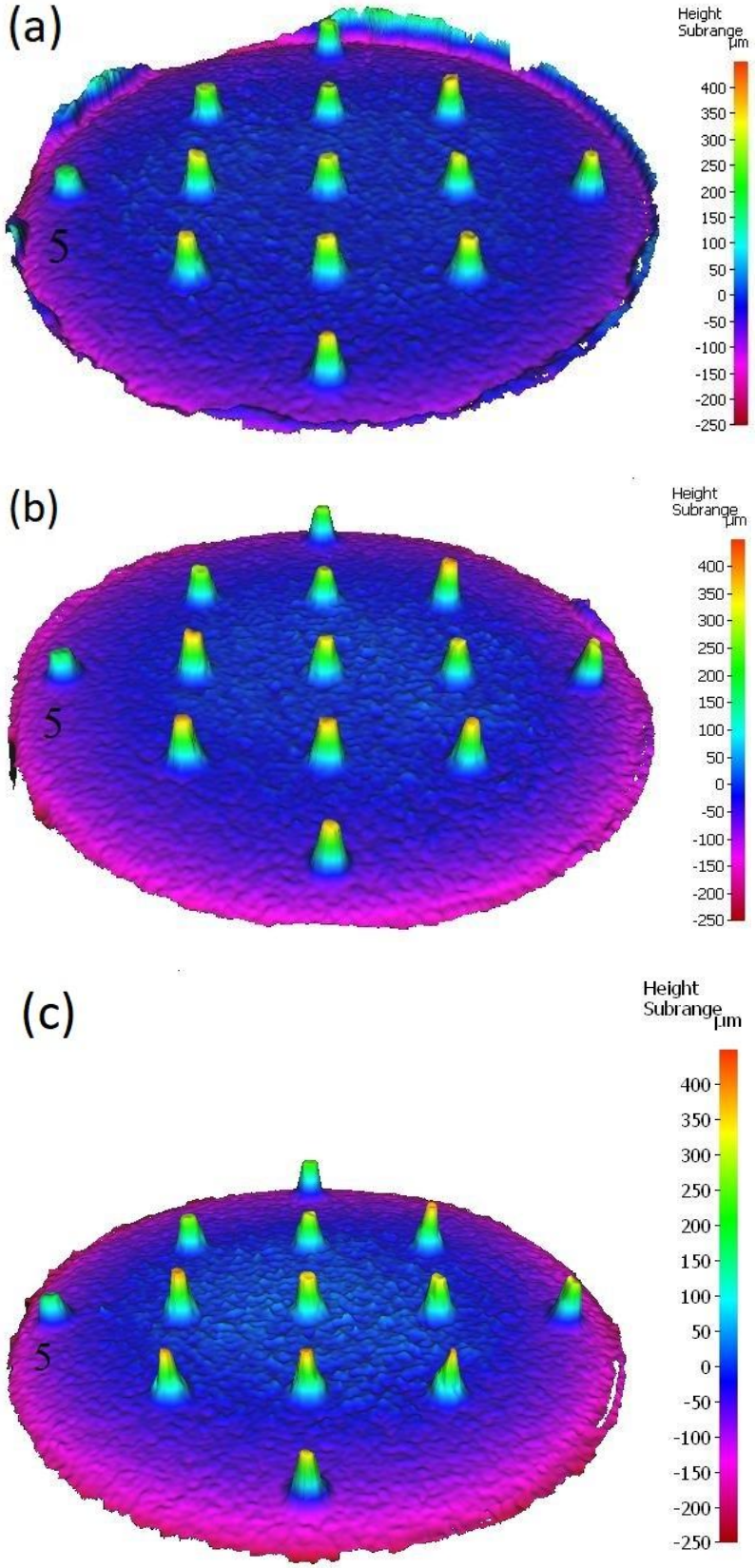

Figure 5.40: Microscope images at 250 °C for CG (a), 4P (b), and 8P (c) materials.

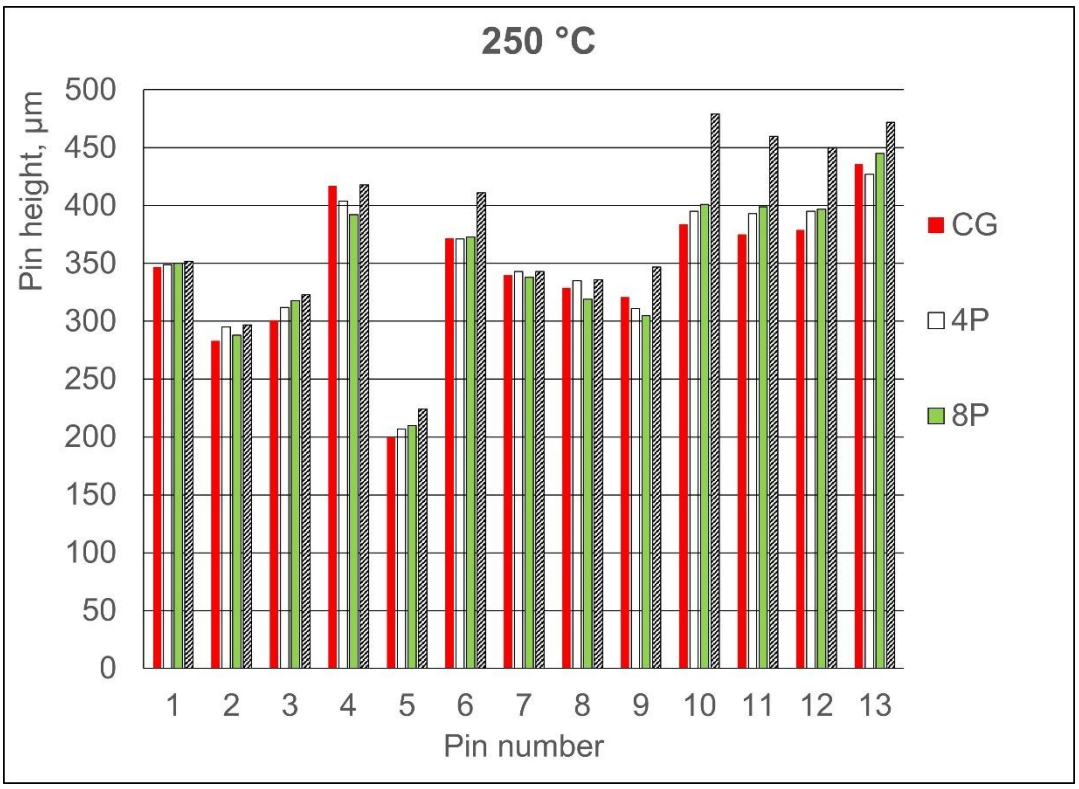

Figure 5.41: Chart of pin heights at 250 °C for CG, 4P, and 8P materials.

Table 5.6 : The experimental average pin heights for CG, 4P, and 8P at 250 °C.

Material	Pin height range (µm)	Average pin height (µm)
CG	285 – 434	359.5
4P	299 – 421	360
8P	289 – 445	367

Table 5.7 : Pin height improvement from 200 °C to 250 °C.

Material	Average pin height at 200 °C (µm)	Average pin height at 250 °C (µm)	Times better
CG	228	359.5	1.6x
4P	246.5	360	1.5x
8P	269	367	1.4x

Table 5.8 : Percentage of cavity filled by conical pins at 250 °C for CG, 4P, and 8P materials.

Pin number	Pin height (μm)			Cavity depth (μm)	% filled		
	CG	4P	8P		CG	4P	8P
1	347	349	350	352	98.58	99.15	99.43
2	283	295	288	297	95.29	99.33	96.97
3	301	312	318	323	93.19	96.59	98.45
4	417	404	392	418	99.76	96.65	93.78
5	200	207	210	224	89.29	92.41	93.75
6	372	371	373	411	90.51	90.27	90.75
7	340	343	338	343	99.13	100.00	98.54
8	329	335	319	336	97.92	99.70	94.94
9	321	311	305	347	92.51	89.63	87.90
10	384	395	401	479	80.17	82.46	83.72
11	375	393	399	460	81.52	85.43	86.74
12	379	395	397	450	84.22	87.78	88.22
13	436	427	445	472	92.37	90.47	94.28

5.3.4 Punch Force-Displacement Curve

During the process of backward micro-extrusion of conical pins, the flow of material into pin cavities is caused by the movement of the punch. This is accompanied by the material reaction force acting on the punch. Thus, the relationship between punch force and punch displacement can be treated as a process signature. The punch force-displacement curves were recorded at three different temperatures, RT, 200 °C, and 250 °C, as shown in Figure 5.42, Figure 5.43, and Figure 5.44, respectively. The maximum punch force values for each material at different temperatures are shown in Table 5.9. As the temperature increases, the maximum punch force also increases, although it remains nearly identical for each material at the same temperature.

All conditions produced a linear response, except the RT process, which resulted in a gradual increase of the response slope in the initial stage of the process. At RT, the impeded material flow at the beginning of the process for all types of material occurs up to around 0.25 mm displacement. This is because the atomic bonding is stronger at RT than at higher temperatures.

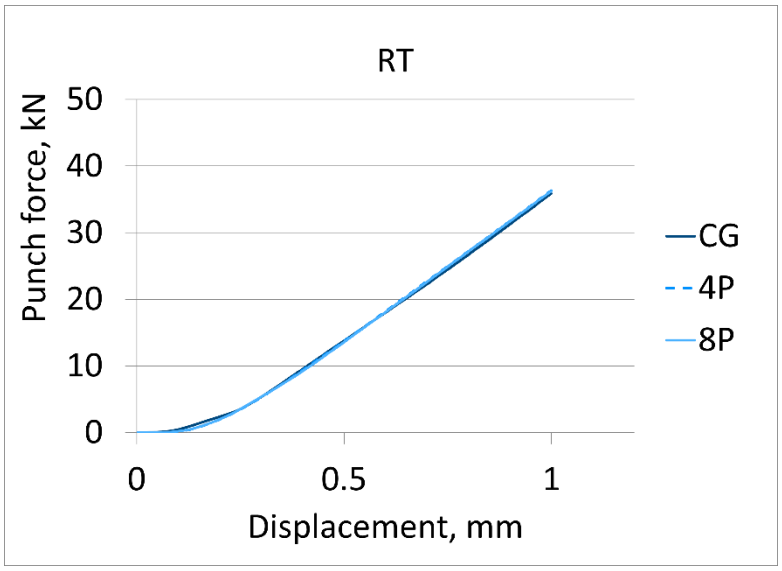

Figure 5.42: The punch force-displacement graph for CG, 4P, and 8P materials at RT.

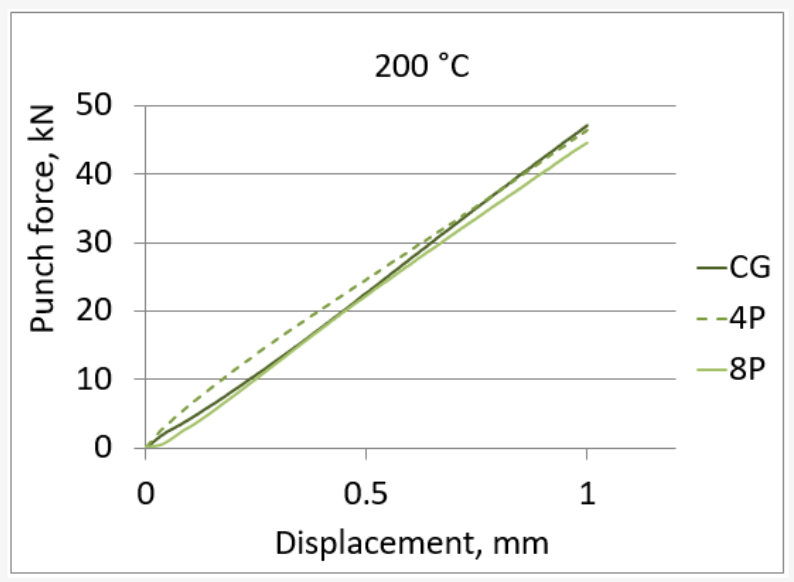

Figure 5.43: The punch force-displacement graph for CG, 4P, and 8P materials at 200 °C.

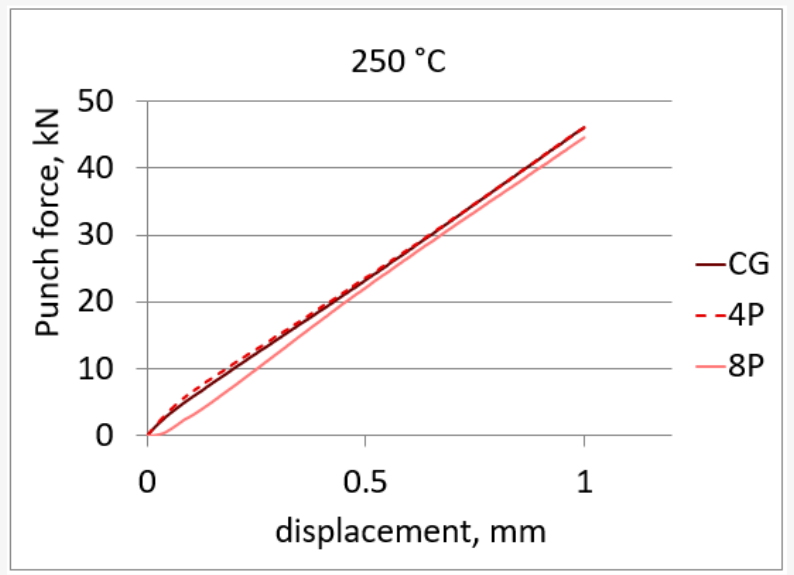

Figure 5.44: The punch force-displacement graph for CG, 4P, and 8P materials at 250 °C.

Table 5.9 : Comparison of maximum punch force at difference temperature for CG, 4P, and 8P materials for experimental.

Material	RT	200 °C	250 °C
CG, kN	35.87	47.15	46.94
4P, kN	36.33	47.39	45.16
8P, kN	34.67	43.22	43.22

5.4 Finite Element Simulation

The finite element simulation of backward micro-extrusion was conducted on 3D models using Abaqus/Explicit 2018. The material properties for the simulation were obtained from compression testing in Subchapter 4.4. The Young's modulus was defined as 70 GPa, and the Poisson's ratio was set to 0.33 (Javidikia & Hashemi, 2017). The friction factor applied between the punch and the pellet was set to 0.8 under dry conditions (Salamati & Rosochowski, 2014). The units used for the finite element simulation were millimetres (mm), Newton (N), and seconds (s).

Figure 5.45 shows the 3D FE model of the backward micro-extrusion process. The pellet was modelled as a deformable body using CAX4T elements, while analytically rigid surfaces were assigned to both the punch and the die. Surface-to-surface contact interactions were defined for both the die-pellet and punch-pellet interfaces. The mesh size was chosen according to the model geometry. Since the gap between the punch, pellet, and die was 0.05 mm, a slightly finer mesh of 0.04 mm was used for the pellet. Proper mesh sizing is essential to prevent element distortion during the simulation. The detailed dimensions are shown in Figure 5.46.

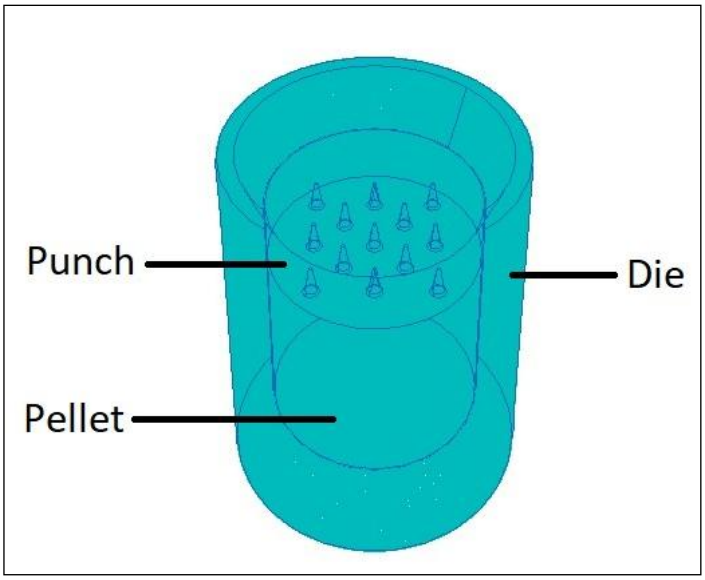

Figure 5.45: 3D FE model of backward micro-extrusion for conical pins.

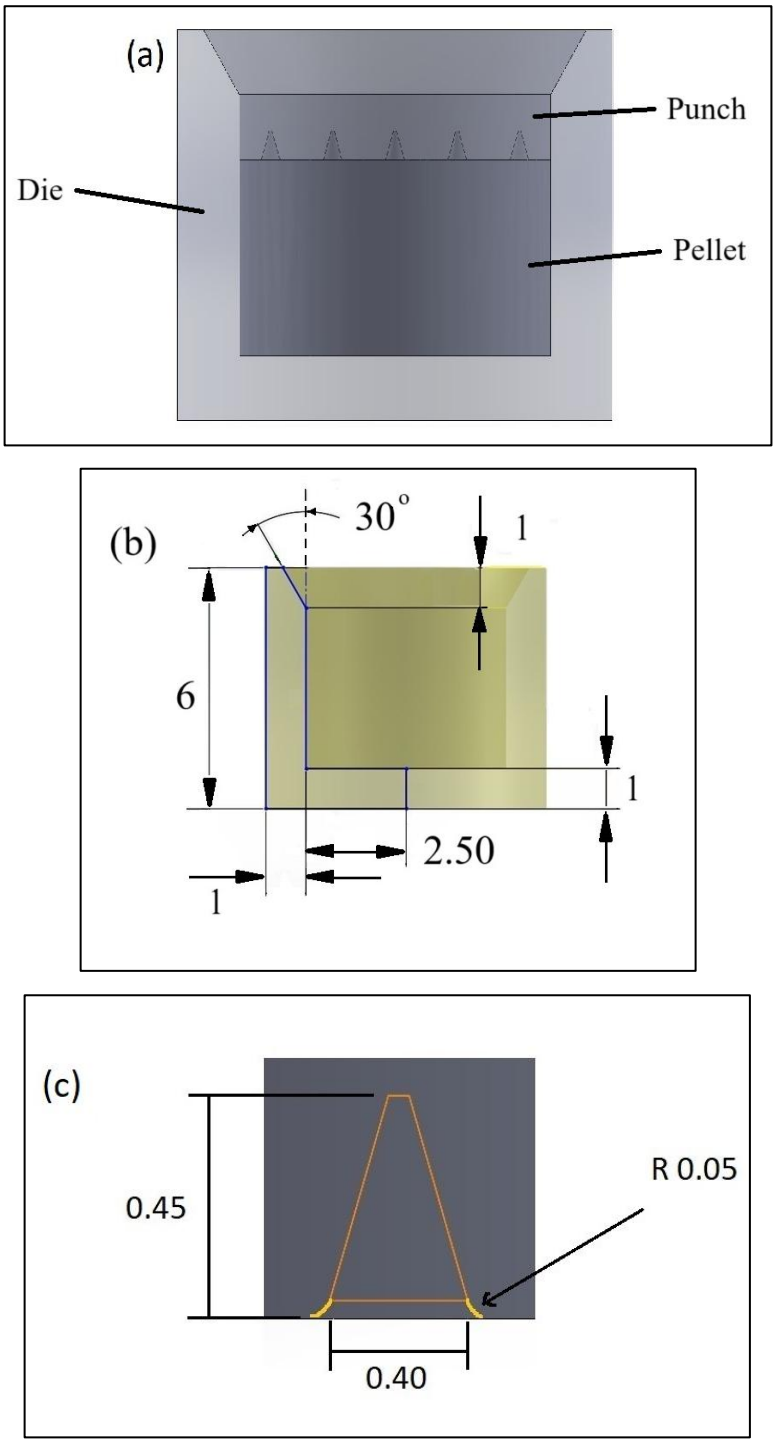

Figure 5.46: Simulation model showing: the 2D model including the punch, pellet and die (a), the detail geometry (b), and the pin cavity geometry (c).

At the beginning of the study, the simulation aimed to determine the optimal punch displacement. Preliminary software-based trials indicated that a displacement of 0.08 mm was sufficient for the pellet to fully fill the pin cavity without causing too much deformation or numerical errors in the simulation. Therefore, this value was used as the reference for the following simulations.

At the microscale, simulating such large values would require extremely small calculation steps, leading to impractically long processing times. Due to limited computing resources, the simulation inputs were scaled down to 0.08 mm punch displacement and 1 second of process duration. This alteration allowed the analysis to be completed in approximately 50 hours on the available computer (Intel Celeron CPU B815, 1.60 GHz, 8 GB RAM). As a result, the full experimental conditions (1 mm displacement and 200 s duration) could not be simulated, and scaled-down parameters were used to keep the analysis practical and representative.

Figure 5.47 presents the simulation results for a process duration of 1 second, using the 8P material properties from Figure 4.20(a). The simulated pin height ranged from 387 µm to 426 µm, nearly filling the pin cavity height of 450 µm.

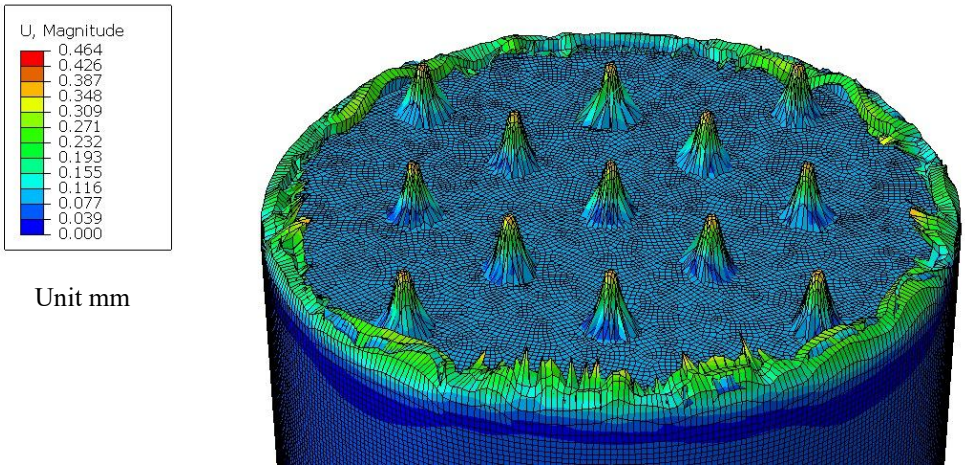

Figure 5.47: Abaqus images of pins extruded at 200 °C for 8P material with 0.08 mm punch displacement and 1-second process duration.

5.4.1 Simulation Pin Height at RT

The simulated pin heights at RT for CG, 4P, and 8P materials are presented in Figure 5.48(a), (b), and (c), respectively. The conical pin heights for all specimens fall within a narrow range of approximately 60-74 μm. In contrast, the experimental results shown in Figure 5.35 indicate a broader variation in pin height, ranging from 45-175 μm. Nevertheless, simulation results for all materials present a similar pattern to experimental results, which produce only a brief bulge of conical pins.

In the finite element model, material behaviour is defined based on flow stress curves obtained from the compression testing. These curves, when input into the simulation software (Abaqus), describe how the material responds to strain under specific conditions.

The simulation assumes ideal conditions where the material properties are constant, the temperature is isothermal, and the friction contact between the tool and the billet is also consistent along the extrusion process. Whereas, during the experiment, all those parameters are kept changing throughout the process. As a result, there are differences in pin height between simulation and experiment.

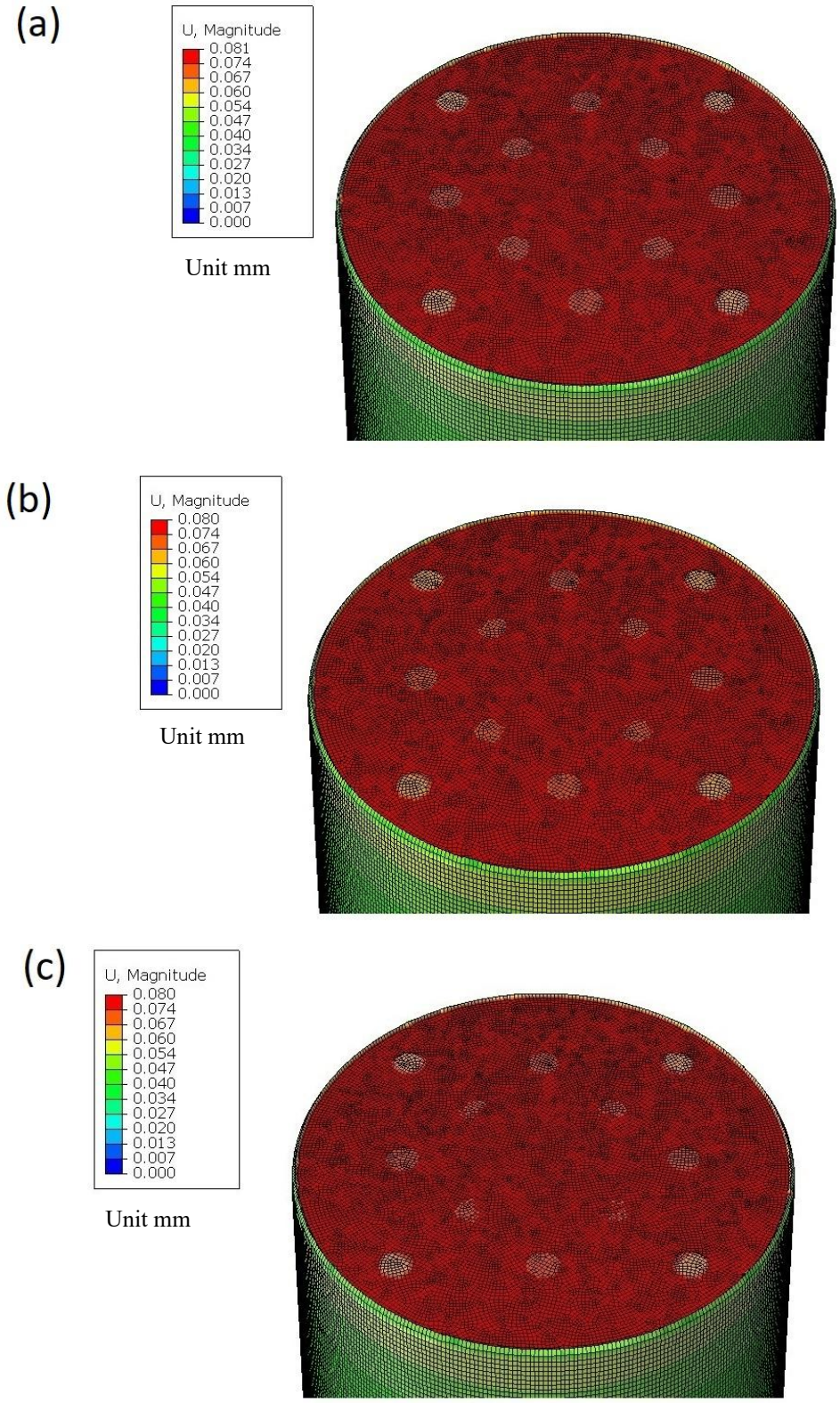

Figure 5.48: Simulation pin height at RT for CG (a), 4P (b), and 8P (c) materials.

5.4.2 Simulation Pin Height at 200 °C

Figure 5.49(a), (b), and (c) show the simulated pin heights of the pellet for the CG, 4P, and 8P materials at 200 °C, respectively. The pin height for the CG material ranges from approximately 131-157 µm, while the experimental range (Figure 5.38) is 185-271 µm. For the 4P material, the simulated pin height ranges from 129-172 µm, compared to the experimental range of 205-288 µm. In the case of the 8P material, the simulated pin heights vary from 169-226 µm, whereas the experimental range is 213-325 µm.

These comparisons show that for all material types, the simulation gives lower pin height values than the experiment. There is a clear difference between the simulation results and the actual behaviour of the material, with an average variation of around 27-39% between the simulated and experimental data, as shown in Table 5.10.

Overall, the simulated pin height results show a similar trend to the experimental data, where the pin height range increases progressively from the CG to the 4P and then to the 8P materials.

Table 5.10 : Comparison of simulated and experimental pin heights at 200 °C.

Material	Simulated Range (µm)	Average Sim. (µm)	Experimental Range (µm)	Average Exp. (µm)	% Difference
CG	131 - 157	144	185 - 271	228	37
4P	129 - 172	150.5	205 - 288	246.5	39
8P	169 - 226	197.5	213 - 325	269	27

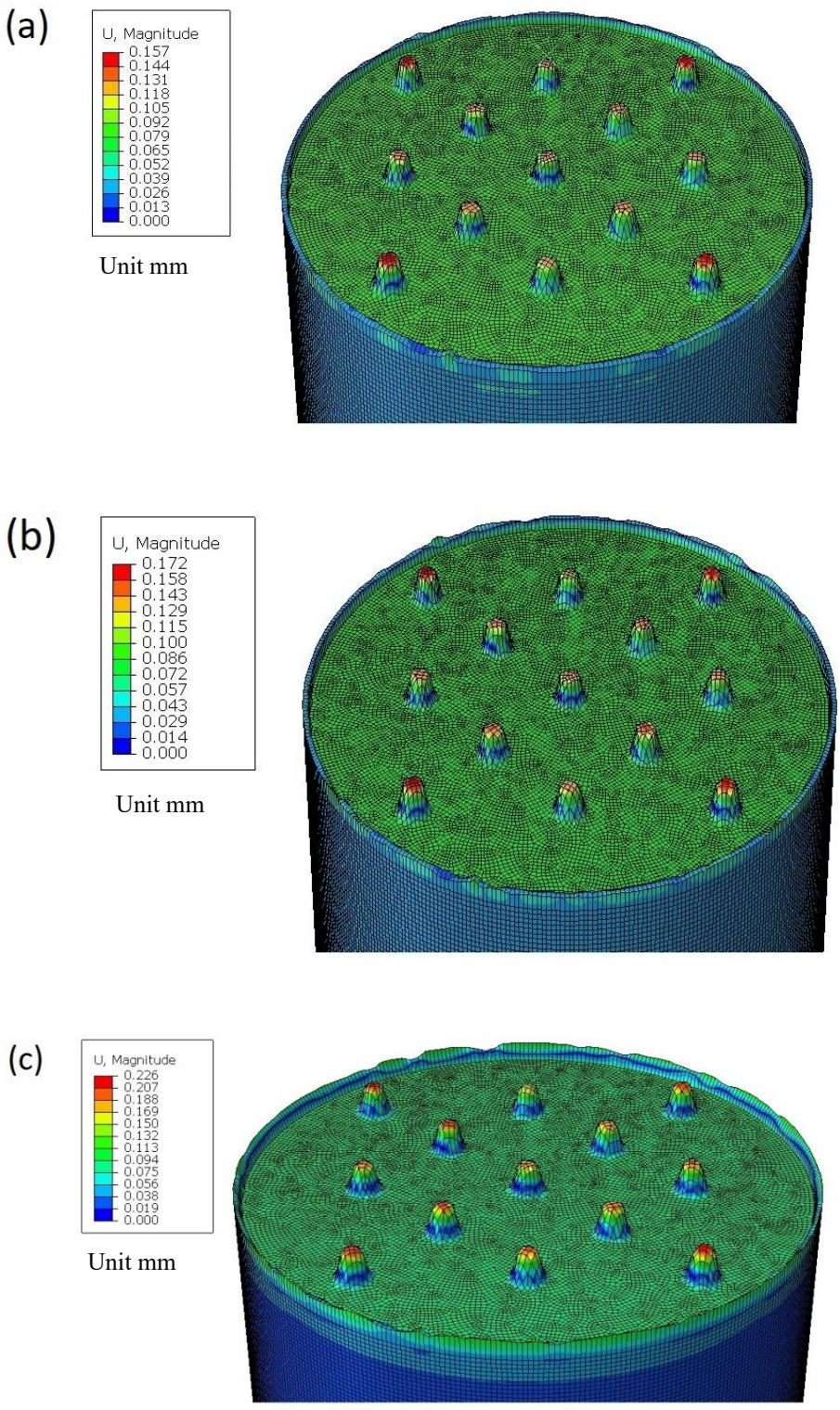

Figure 5.49: Simulation pin height at 200 °C for CG (a), 4P (b) and 8P (c) materials.

5.4.3 Simulation Pin Height at 250 °C

Figure 5.50(a), (b), and (c) show the simulated pin heights of the pellet for the CG, 4P, and 8P materials at an elevated temperature of 250 °C. The simulated pin height ranges for the CG, 4P, and 8P materials are 264-317 µm, 324-389 µm, and 323-387 µm, respectively. Compared to the simulated results at 200 °C, all specimens show a clear increase in pin height, with average percentage increases of 102%, 137%, and 80% for CG, 4P, and 8P materials, respectively (Table 5.11).

Comparing the simulation and experimental results at 250 °C, as shown in Table 5.12, the average difference in pin height for the CG material is approximately 19%. In contrast, the 4P and 8P materials show much smaller difference of about 1-3%, showing that the simulation matches the experimental results for the UFG materials.

This good agreement suggests that the finite element model can closely predict the flow of UFG materials. The input parameter, such as the friction factor, is suitable for simulating UFG materials but not for the CG type.

Table 5.11: Comparison of average simulated pin height at 200 °C and 250 °C with percentage increase.

Material	Pin height at 200 °C		Pin height at 250 °C		% Increase
	Range (µm)	Average (µm)	Range (µm)	Average (µm)	
CG	131 – 157	144	264 – 317	290.5	102
4P	129 – 172	150.5	324 – 389	356.5	137
8P	169 – 226	197.5	323 – 387	355	80

Table 5.12 : Comparison of simulated and experimental pin heights at 250 °C.

Material	Simulated Range (µm)	Average Sim. (µm)	Experimental Range (µm)	Average Exp. (µm)	% Difference
CG	264 – 317	290.5	285 – 434	359.5	19
4P	324 – 389	356.5	299 – 421	360.0	1
8P	323 – 387	355.0	289 – 445	367.0	3

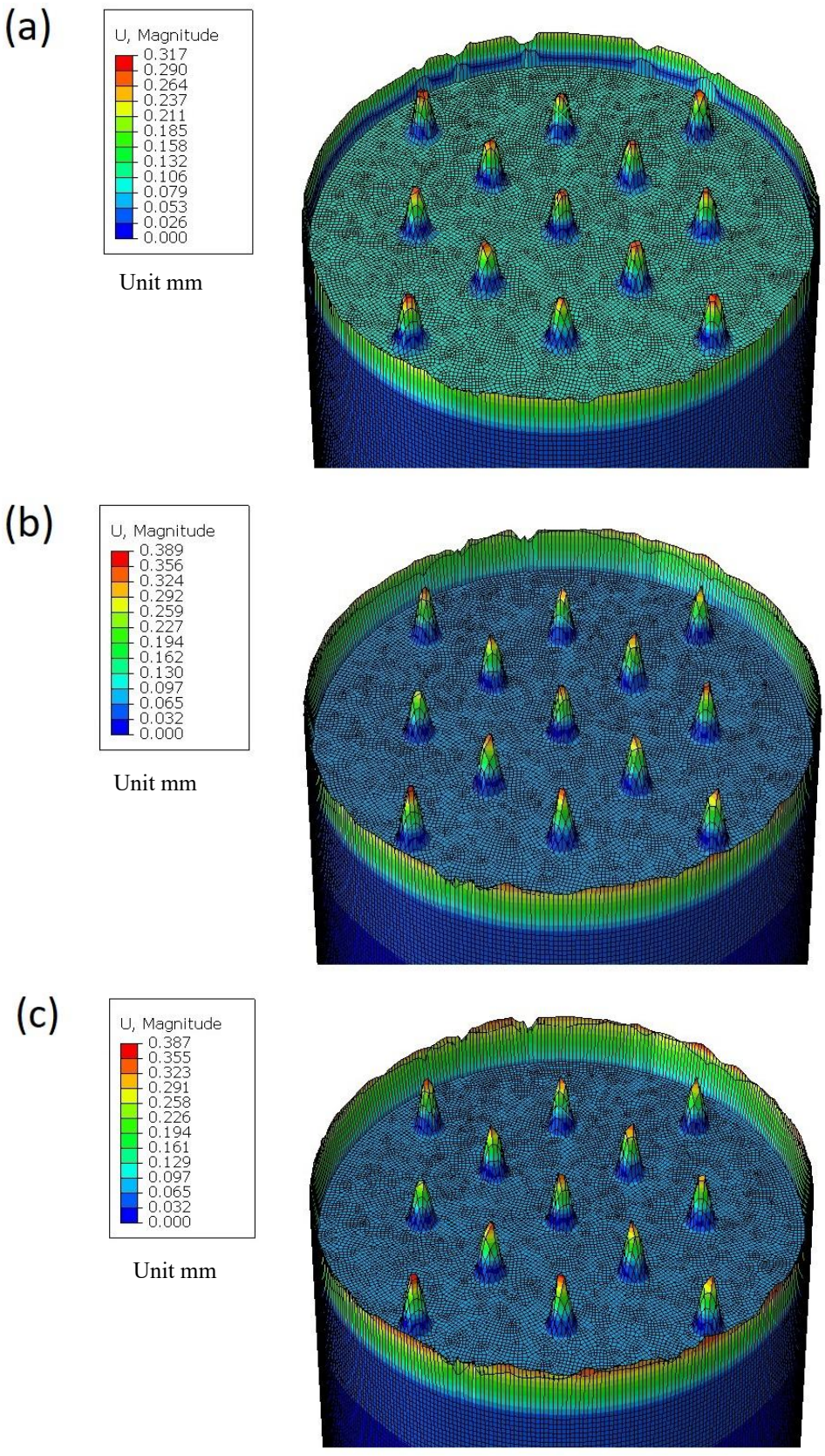

Figure 5.50: Simulation pin height at 250 °C for CG (a), 4P (b) and 8P (c) materials.

5.4.4 Simulation Graph Punch Force-Displacement at RT

Figure 5.51 shows a graph of punch force versus displacement at RT derived from simulation results for CG, 4P, and 8P materials. The curves for all materials exhibit a typical backward extrusion profile, like the reference pattern shown in Figure 5.1. During the coining phase, the punch force for all materials increases sharply, then slightly oscillates but remains almost flat in the steady state and finally increases sharply during the unsteady-state phases.

The 4P and 8P materials have the largest punch force, showing greater resistance to deformation than CG. This result aligns with the material properties defined in the simulation model. The maximum punch forces from the simulation were 20.1 kN for CG, 21.2 kN for 4P, and 21.5 kN for 8P. The percentage differences between the simulation and experimental results (Figure 5.42) are 44% for CG, 42% for 4P, and 38% for 8P, according to Table 5.13.

These differences between the simulation and experimental results show that the input parameters for the finite element model must consider a corrected friction factor during the simulation process. It is important to identify this parameter to bring the punch force curve simulation results closer to the experimental data.

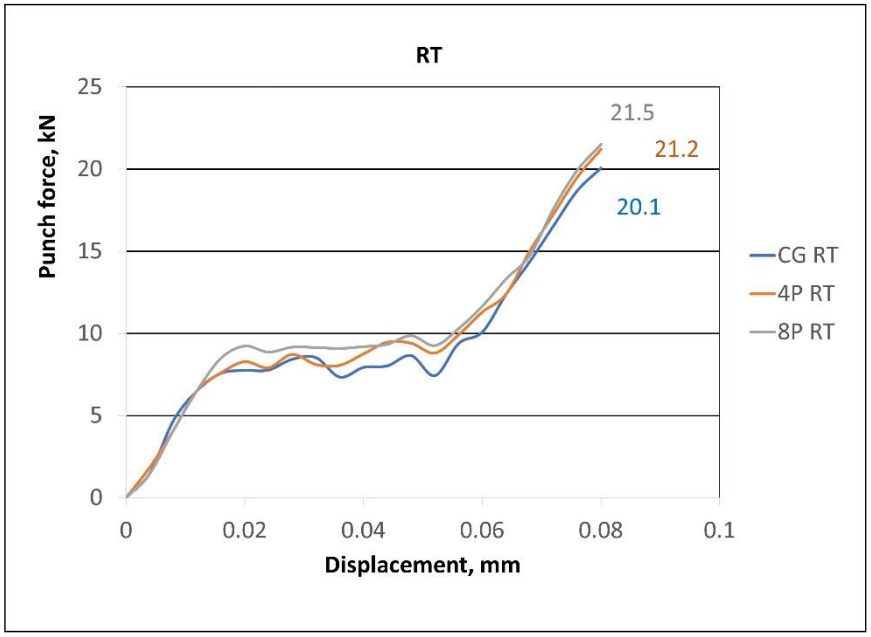

Figure 5.51: Punch force-displacement graph simulation at RT.

Table 5.13 : Comparison of simulation and experimental punch force at RT with percentage differences.

Material	Experimental (kN)	Simulation (kN)	Percentage Difference (%)
CG	35.87	20.1	44
4P	36.33	21.2	42
8P	34.67	21.5	38

5.4.5 Simulation Graph Punch Force-Displacement at 200 °C

Figure 5.52 presents the punch force-displacement curves from the simulation results at 200 °C. All specimens display the typical pattern of a backward extrusion curve. The punch force for all materials during the unsteady state at 200 °C is lower than at RT (Figure 5.51), remaining below 5 kN. This is in line with the material properties at elevated temperature, where the yield strength decreases as the processing temperature increases.

According to Table 5.14, the percentages differences for CG, 4P, and 8P are 32.4%, 35.2%, and 32.7%, respectively. Since the percentage differences are still high, the finite element model needs to be modified to better match the experimental results.

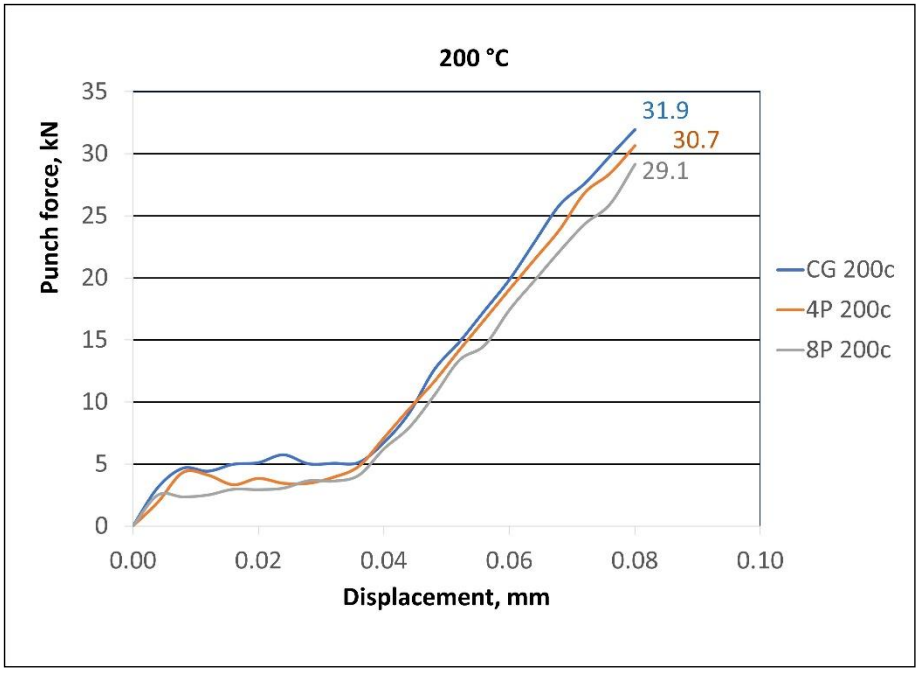

Figure 5.52: Punch force-displacement graph simulation at 200 °C.

Table 5.14 : Comparison of simulation and experimental punch force at 200 °C with percentage differences.

Material	Experimental (kN)	Simulation (kN)	Percentage Difference (%)
CG	47.15	31.9	32.4
4P	47.39	30.7	35.2
8P	43.22	29.1	32.7

5.4.6 Simulation Graph Punch Force-Displacement at 250 °C

The punch force-displacement results from the simulation at a processing temperature of 250 °C are shown in Figure 5.53. The punch force-displacement curve does not follow the typical trend of backward extrusion, with the linear portion of the coining phase becoming almost indistinguishable. Additionally, the punch force during the unsteady phase decreases.

The maximum simulated punch forces are 37.2 kN for the CG, 31.8 kN for the 4P, and 31.0 kN for the 8P materials. The lower maximum punch force for the UFG materials (4P and 8P) compared to the CG material is attributed to their material properties at elevated temperature (Figure 4.20 and Figure 4.22).

According to Table 5.15, the percentage differences between the simulation and experiment at 250 °C are 20.8% for CG, 29.6% for 4P, and 28.3% for 8P. These values show that the differences are quite large. Therefore, the finite element model at 250 °C needs to be improved to achieve more accurate results.

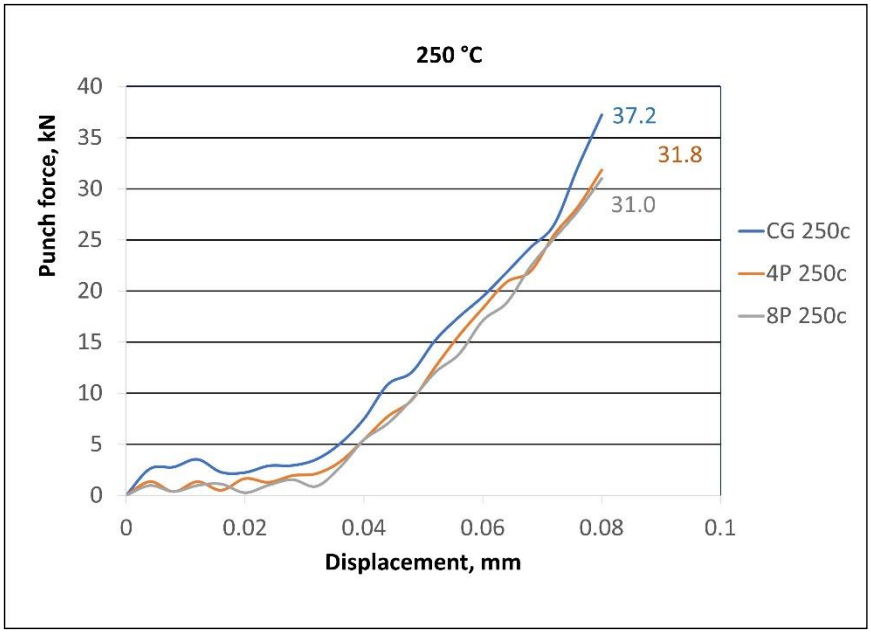

Figure 5.53: Punch force-displacement graph simulation at 250 °C.

Table 5.15 : Comparison of simulation and experimental punch force at 250 °C with percentage differences.

Material	Experimental (kN)	Simulation (kN)	Percentage Difference (%)
CG	46.94	37.2	20.8
4P	45.16	31.8	29.6
8P	43.22	31.0	28.3

5.5 Analysis and Discussion

This section examines the findings of the experiment and simulation for backward micro-extrusion. The results focus on the height of the conical pin and the punch force-displacement curve for both the experiment and the simulation at RT and at elevated temperatures of 200 °C and 250 °C, respectively.

Experimental Results: Height of the Conical Pin

1. The conical pin was not successfully produced for all materials at RT due to the material being unsuitable to flow smoothly. This is related to its material properties, which have higher yield strength and lower ductility at RT.
2. At elevated temperatures, the conical pin was successfully formed because the materials became more ductile and softer, resulting in their deforming easily and creating better shape filling of the cavity.
3. At 200 °C, the pin height improved significantly by 1.6 to 3.6 times compared with RT. Despite this enhancement, it reached only about 60% to 70% of the total cavity depth. At this temperature, UFG materials showed higher pin heights, probably due to finer grains that allow the material to flow more effectively.
4. At 250 °C, the pin height achieved approximately 80% to 100% of the cavity depth, with all materials producing almost similar pin heights. At this stage, UFG and CG materials obtained very similar pin heights.

Experimental Results: Punch Force-Displacement

1. At elevated temperatures, all materials produced nearly linear curves, indicating that the material deformed uniformly towards the end of the displacement setting.
2. At RT, the curve shows a slightly shallow rise during the early stage of deformation before continuing in a linear line trend towards the end of the process for all materials. This suggests that the material encountered initial resistance to deformation at the beginning of the process.
3. At both RT and elevated temperatures, all curves were noticeably plotted without following the typical trend of the punch force-displacement curve, as shown in Figure 5.1. Specifically, there are no flat regions, which usually represent steady-

state conditions. One possible reason is the tiny size of the specimen, which made the system unable to record accurately the steady-state condition. Another factor could be tool deflection during extrusion, which prevented the punch force from achieving a steady state and the plateau region from appearing.

4. The maximum punch force in the experiment for all materials at 200 °C and 250 °C was nearly identical, with values ranging between 43 kN and 47 kN. This shows that factors like specimen size and tool deflection affected the experimental results, preventing the typical trend shown in Figure 5.1from being observed.

Rationale for Conducting Experiments Before Simulation

1. For this study, experiments were performed before simulations for two main reasons:
    i. Uncertainties in microscale extrusion: The success of the backward micro-extrusion process at the microscale depends on several factors, such as friction and tool interaction. The material flow is difficult to predict accurately without any reference data. Therefore, the initial experiments were carried out to provide baseline observations to confirm the feasibility of the process and to give insight into actual material behaviour.
    ii. Need for accurate input parameters: The simulation requires accurate data, such as flow stress curves, friction, and boundary conditions. Since this information is not available for UFG Al5083, experiments were done to gather the needed data.
2. From the experiments, data such as pin height and punch force-displacement were collected and compared with the simulation results.
3. The simulation inputs were adjusted until they matched the experimental results, which made the models more accurate.
4. The experiment served as a basis for the simulations, allowing other process conditions to be investigated without the cost and effort of additional trial runs.

Simulation Results

The finite element modelling was verified using experimental data for pin height and punch force-displacement graphs at various temperatures for all materials.

1. At RT, the simulated pin heights were about 39% lower than the average experimental values. At 200 °C, the difference in pin height between the simulation and experiment was still quite large, approximately 27% to 39%. At 250 °C, the simulation matched the experiments very well for 4P and 8P, with only 1% and 3% differences, respectively. For the CG material, the difference was a bit larger at 19%. Overall, the model predicted the UFG material behaviour accurately at higher temperatures, but it underestimated the pin heights for CG and for all materials at lower temperatures, highlighting the need to consider correct friction values, especially at lower temperatures.
2. The simulated punch force-displacement curve followed a similar trend to macro extrusion but differed from the experimental results. For the maximum punch forces, the simulated values increased with temperature, and the gap with the experiments remained large, approximately 38-44% at RT, 32-35% at 200 °C, and 21-29% at 250 °C. Therefore, the model should include factors such as tool deflection to make the results more accurate.

5.6 Summary

Backward micro-extrusion experiments on CG and UFG Al5083 were carried out at RT, 200 °C, and 250 °C. At RT, the conical pins did not form completely because the material was very hard and had low ductility. Increasing the temperature improved material flow, with pin heights reaching approximately 80-100% of the cavity depth at 250 °C.

The temperature of 250 °C was identified as the optimal deformation condition for producing miniature conical pins using Al5083, with a punch displacement of 1.0 mm and a process duration of 200 s. At this temperature, the conical pins reached the full cavity depth. These results confirm that better product quality depends on an appropriate processing temperature. Furthermore, UFG materials at 250 °C showed the lowest punch force, which helps reduce tool wear and extend die life during the backward micro-extrusion process.

Finite element simulations captured the general trends of pin height, with the best agreement observed for UFG materials at 250 °C. However, the simulated results differed slightly from the experimental data, particularly at lower temperatures, where pin heights were underestimated. This indicates that the simulation model needs improvement, especially in incorporating temperature-dependent material behaviour and correct friction factor input parameters. The simulated punch force–displacement curves showed a similar trend to macro extrusion but were still quite different from the experiments. The simulated forces were higher, with noticeable gaps that suggest factors like tool deflection should be included to improve accuracy.

Overall, the combination of experimental and simulation approaches provided a comprehensive understanding of micro-extrusion behaviour. The study highlights the critical roles of temperature, grain size, and process parameters in achieving high-quality miniature pins while optimising tool performance.

CHAPTER 6
CONCLUSIONS AND RECOMMENDATIONS

6.1 Conclusions

The important conclusions from this study are summarised below.

1. UFG Al 5083 Produced by Double-Billet I-ECAP
   The double-billet I-ECAP method successfully reduced the grain size of Al 5083, producing a UFG microstructure after four (4P) and eight (8P) passes. Compared to the CG material, the grain size decreased by 97.6% for the 4P material and 97.8% for the 8P material. The average grain sizes for the CG, 4P and 8P materials are 20, 0.44, and 0.49 μm, respectively. The 8P material exhibits a more uniform grain distribution and a higher fraction of HAGB.

2. Improved Mechanical Properties After I-ECAP
   The mechanical properties and hardness of Al 5083 improved after grain refinement by I-ECAP. The yield strength increased from 290 MPa (CG) to 300 MPa (4P) and 350 MPa (8P), while the UTS also increased from 340 MPa (CG) to 350 MPa (4P) and 390 MPa (8P). The elongation to failure showed inconsistency as the grain size decreased, increasing from 10% (CG) to 24% (4P) but slightly dropping to 18% (8P). However, the hardness kept increasing from 100 HV (CG) to 118 HV (4P) and 122 HV (8P), was better by about 18-22%. Overall, the 4P material is considered the optimal billet due to its good balance between strength and ductility.

3. Impact of Processing on Deformation

   Compression tests showed that increasing the processing temperature or reducing the strain rate lowered the true stress-true strain curves for all materials, indicating that the materials became softer.

4. Backward Micro-extrusion Results

   Conical pins were formed only at elevated temperatures. Increasing the temperature to 250 °C improved material flow, allowing the cavity to be almost filled. The results showed that pin height increased with processing temperature. Raising the temperature from 200 °C to 250 °C enhanced material flow inside the pin cavity. As a result, the heights of the conical pins achieved ranged from 80% to 100% of the cavity height for all specimens. Processing the UFG material at elevated temperatures also reduced the punch force, contributing to a longer toolset lifespan and reduced manufacturing costs.

5. Optimal Microforming Conditions

   The optimal process parameters for backward micro-extrusion were 250 °C, a punch displacement of 1.0 mm, and a process time of 200 s. Under these conditions, the pin heights for all specimen types were nearly the same. These findings suggest a minimum grain size for CG material that can produce the same pin height as UFG material at elevated temperatures.

6. Finite Element Simulation Validation

   The finite element model successfully predicted the general trends of pin height and punch force-displacement behaviour, with good agreement observed at higher temperatures. At 250 °C, simulated results for 4P and 8P billets were within 1–3% of the experimental values. However, discrepancies at lower temperatures indicated the need for refinement of friction coefficients and temperature-dependent material data.

The findings of this study can be generalised to other products manufactured through backward micro-extrusion using UFG materials. One potential application is the production of axisymmetric miniature components, provided that a suitable jig and tool are developed for this purpose. The process parameters identified in this work are also relevant to the fabrication of other micro-products that rely on controlled flow within constrained dies. The successful production of high-quality parts is promising, as the knowledge gained from this study contributes to a broader understanding of material behaviour in micro-manufacturing environments.

However, such generalisation should be made with care. Products with significantly different geometries may respond differently during deformation. Preliminary software simulation may provide an early overview of material flow, particularly punch force, which can serve as a useful reference when selecting suitable experimental parameters.

6.2 Contributions

This study successfully produced miniature conical pins using backward micro-extrusion of UFG Al 5083. The formability of the conical pin height was studied under different temperature conditions to determine the optimal processing parameters for backward micro-extrusion.

The main contributions and new knowledge generated from this research are summarised below.

1. Material Preparation and Processing

   Proved that the I-ECAP process at 200 °C successfully achieved UFG material without any crack. Introduced a novel billet preparation method that was able to reduce friction during I-ECAP.

2. Tool and Process Development

   Developed a reliable backward micro-extrusion jig capable of forming miniature conical pins with precise control of temperature, punch displacement, and processing time.

3. Forming Parameter Optimisation

   Developed a novel process flow to identify the optimal parameters for backward micro-extrusion.

4. Characterisation and Data Analysis

   Developed a reliable flow stress curve that can serve as reference data for future process modeling and FEM simulations.

5. Practical and Industrial Implications

   Application of UFG materials in backward micro-extrusion clearly reduces punch force, significantly extends tool life, and lowers production costs. This study provides guidelines for the microforming industry on UFG material preparation and tool design to improve process efficiency.

In summary, this study has improved the understanding of microforming behaviour in Al 5083 processed by I-ECAP and identified the optimal conditions for backward micro-extrusion of miniature conical pins. The experimental findings, tool development, and material characterisation provide valuable knowledge for enhancing formability, reducing tool load, and improving the overall efficiency of microforming processes.

6.3 Recommendations for Future Work

Based on the findings and limitations of this study, several areas are recommended for future research:

1. Improved Material Modelling

   Accurate finite element models are necessary to simulate microforming behaviour. These models require temperature and strain-rate dependent material data, as well as realistic friction factor conditions.

2. Effect of Different Temperatures and Passes in I-ECAP

   Processing Al 5083 via I-ECAP at different temperatures and with varying numbers of passes resulted in significant changes in material properties. Future studies could further explore these variations, including the effects of different processing routes and combinations of temperatures and passes.

3. Tool Design and Surface Engineering

   A new punch design that allows the use of lubricants in backward micro-extrusion could be proposed. Future studies could also investigate the effects of tool surface texture, suitable coatings, and lubrication conditions. Considering these factors could lead to improved product quality, better dimensional accuracy, and longer tool life.

4. Extended Material Studies

   The double-billet I-ECAP and backward micro-extrusion methods could be applied to other materials, such as titanium, stainless steel, cobalt-chromium alloys, and nitinol, which are widely used in medical applications.

5. Precision Tool Fabrication for Microforming

   Fabricating precision tools for microforming remains challenging, and many manufacturing technologies still face these limitations. Tools for micromanufacturing require very high accuracy, superior surface quality, and precision, which are difficult to achieve. Therefore, improving fabrication technologies is essential to meet these demands.

6. Improving Process Chains

   The future of manufacturing is moving towards Industry 4.0 (IR4.0), which involves digital monitoring, smart sensors, and data-driven processes to enhance process integration, accuracy, and high productivity. In microforming, combining the SPD process with a continuous microforming process could help achieve this concept. Together with automation and flexible production, these developments can further improve efficiency and make microforming more practical for industrial applications.

6.4 Limitations of the Study

The findings from this study could be used as a reference for applications on other materials. In producing UFG materials via I-ECAP, the optimum process parameters can be determined by following the procedures outlined in this study. Similar to the experimental work, the important aspects to consider have already been highlighted in the methodology and experimental chapters.

However, this study focused only on the Al 5083 and miniature conical pins as final products. Therefore, the results may not directly apply to other alloys or geometries. In the I-ECAP process, the tools surface was not measured, making it unclear exactly what occurred during the processing. Similarly, for each pin cavity on the punch during backward micro-extrusion, the friction factor is unknown, which may limit the accuracy of the results. The simulation model did not account for tool deflection or variations in friction at different temperatures, reducing the accuracy of predictions. Additionally, grain growth was assumed to be stable throughout the process, which may not reflect real conditions.

REFERENCES

Azushima, A., Kopp, R., Korhonen, A., Yang, D. Y., Micari, F., Lahoti, G. D., Groche, P., Yanagimoto, J., Tsuji, N., Rosochowski, A., Yanagida, A. (2008). Severe plastic deformation (SPD) processes for metals. *CIRP Annals, 57*(2), 716-735. https://doi.org/10.1016/j.cirp.2008.09.005

Barnes, A. J. (2007). Superplastic forming 40 years and still growing. *Journal of Materials Engineering and Performance*, *16*(4), 440-454. https://doi.org/10.1007/s11665-007-9076-5

Benedyk, J. C. (2010). International temper designation systems for wrought aluminum alloys. *Light metal age, 67*, 3-6.

Beygelzimer, Y., Varyukhin, V., Synkov, S., & Orlov, D. (2009). Useful properties of twist extrusion. *Materials Science and Engineering: A, 503*(1), 14-17. https://doi.org/10.1016/j.msea.2007.12.055

Bhovi, P. M., Patil, D. C., Kori, S. A., Venkateswarlu, K., Huang, Y., & Langdon, T. G. (2016). A comparison of repetitive corrugation and straightening and high-pressure torsion using an Al-Mg-Sc alloy. *Journal of Materials Research and Technology, 5*(4), 353-359. https://doi:10.1016/j.jmrt.2016.03.009

Bridgman, P. W. (1943). On torsion combined with compression. *Journal of Applied Physics, 14*(6), 273-283. https://doi.org/10.1063/1.1714987

Chan, W. L., Fu, M. W., & Yang, B. (2011). Study of size effect in micro-extrusion process of pure copper. *Materials & Design*, *32*(7), 3772-3782. https://doi.org/10.1016/j.matdes.2011.03.045

Chang, C. C., & Wang, T. C. (2010). Effects of grain size on micro backward extrusion of copper. *Advanced Materials Research*, *83*, 1092-1098. https://doi.org/10.4028/www.scientific.net/AMR.83-86.1092

Chang, S. Y., Lee, J. G., Park, K. T., & Shin, D. H. (2001). Microstructures and mechanical properties of equal channel angular pressed 5083 Al alloy. *MATERIALS TRANSACTIONS, 42*(6), 1074-1080. https://doi.org/10.2320/matertrans.42.1074

Chang, S. Y., Ahn, B. D., Hong, S. K., Kamado, S., Kojima, Y., & Shin, D. H. (2005). Tensile deformation characteristics of a nano-structured 5083 Al alloy. *Journal of Alloys and Compounds, 386*(1), 197-201. https://doi.org/10.1016/j.jallcom.2004.03.148

Cheung, C., Djuanda, F., Erb, U., & Palumbo, G. (1995). Electrodeposition of nanocrystalline Ni-Fe alloys. *Nanostructured Materials, 5*(5), 513-523. https://doi.org/10.1016/0965-9773(95)00264-F

Comley, P. N. (2004). Manufacturing advantages of superplastically formed fine-grain Ti-6Al-4V alloy. *Journal of Materials Engineering and Performance, 13*(6), 660-664. https://doi.org/10.1361/10599490421259

Ding, S., Khan, S. A., & Yanagimoto, J. (2020). Flow behavior and dynamic recrystallization mechanism of A5083 aluminum alloys with different initial microstructures during hot compression. *Materials Science and Engineering: A, 787*, 139522. https://doi.org/10.1016/j.msea.2020.139522

Dupuy, L., Blandin, J. J., & Rauch, E. F. (2000). Structural and mechanical properties in AA 5083 processed by ECAE. *Materials science and technology, 16*(11-12), 1256-1258. https://doi.org/10.1179/026708300101507424

Edalati, K., Bachmaier, A., Beloshenko, V. A., Beygelzimer, Y., Blank, V. D., Botta, W. J., Bryła, K., Čížek, J., Divinski, S., Enikeev, N. A., Estrin, Y., Faraji, G., Figueiredo, R. B., Fuji, M., Furuta, T., Grosdidier, T., Gubicza, J., Hohenwarter, A., Horita, Z., ... Zhu, X. (2022). Nanomaterials by severe plastic deformation: review of historical developments and recent advances. *Materials Research Letters*, *10*(4), 163-256. https://doi.org/10.1080/21663831.2022.2029779

Edalati, K., Ahmed, A. Q., Akrami, S., Ameyama, K., Aptukov, V., Asfandiyarov, R. N., ... & Zhu, Y. T. (2024). Severe plastic deformation for producing superfunctional ultrafine-grained and heterostructured materials: an interdisciplinary review. *Journal of Alloys and Compounds*, *1002*, 174667. https://doi.org/10.1016/j.jallcom.2024.174667

Eichenhueller, B., Egerer, E., & Engel, U. (2007). Microforming at elevated temperature-forming and material behaviour. *The International Journal of Advanced Manufacturing Technology, 33*(1), 119-124. https://doi.org/10.1007/s00170-006-0731-z

Engel, U., & Eckstein, R. (2002). Microforming—from basic research to its realization. *Journal of Materials Processing Technology, 125-126*, 35-44. https://doi.org/10.1016/S0924-0136(02)00415-6

Fang, Z. Z., Wang, X., Ryu, T., Hwang, K. S., & Sohn, H. Y. (2009). Synthesis, sintering, and mechanical properties of nanocrystalline cemented tungsten carbide – A review. *International Journal of Refractory Metals and Hard Materials, 27*(2), 288-299. https://doi.org/10.1016/j.ijrmhm.2008.07.011

Ferrasse, S., Segal, V. M., Alford, F., Kardokus, J., & Strothers, S. (2008). Scale up and application of equal-channel angular extrusion for the electronics and aerospace industries. *Materials Science and Engineering: A, 493*(1), 130-140. https://doi.org/10.1016/j.msea.2007.04.133

Frint, S., Hockauf, M., Frint, P., & Wagner, M. F. X. (2016). Scaling up Segal's principle of Equal-Channel Angular Pressing. *Materials & Design, 97*, 502-511. https://doi.org/10.1016/j.matdes.2016.02.067

Funazuka, T., Dohda, K., Shiratori, T., Horiuchi, S., & Watanabe, I. (2022). Effect of Punch Surface Microtexture on the Microextrudability of AA6063 Micro Backward Extrusion. *Micromachines*, *13*(11), 2001. https://doi.org/10.3390/mi13112001

Funazuka, T., Nakamura, K., Shiratori, T., & Dohda, K. (2025). Effects of Punch and Die Surface Textures and CoCrMo Die Material on the Micro-Backward Extrudability of Pure Magnesium. *Journal of Bio-and Tribo-Corrosion*, *11*(1), 11. https://doi.org/10.1007/s40735-024-00936-z

Geiger, M., Kleiner, M., Eckstein, R., Tiesler, N., & Engel, U. (2001). Microforming. *CIRP Annals, 50*(2), 445-462. https://doi.org/10.1016/S0007-8506(07)62991-6

Groover, M. P. (2020). *Fundamentals of modern manufacturing: materials, processes, and systems*: John Wiley & Sons.

Gzyl, M. (2014a). *Improving mechanical properties of a magnesium alloy by severe plastic deformation* [Doctoral dissertation, University of Strathclyde]. Strathprints Institutional Repository. https://doi.org/10.48730/dvq5-6516

Gzyl, M., Rosochowski, A., Pesci, R., Olejnik, L., Yakushina, E., & Wood, P. (2014b). Mechanical properties and microstructure of AZ31B magnesium alloy processed by I-ECAP. *Metallurgical and Materials Transactions A*, *45*(3), 1609-1620. https://doi.org/10.1007/s11661-013-2094-z

Hansen, N. (2004). Hall–Petch relation and boundary strengthening. *Scripta materialia, 51*(8), 801-806. https://doi.org/10.1016/j.scriptamat.2004.06.002

Heckele, M., Bacher, W., & Müller, K. D. (1998). Hot embossing-the molding technique for plastic microstructures. *Microsystem technologies*, *4*(3), 122-124. https://doi.org/10.1007/s005420050112

Heinz, T. (2006). *Metal Forming Practise: Processes – Machines – Tools*. Springer. https://doi.org/10.1007/3-540-33217-0

Henry, S., McAllister, D. V., Allen, M. G., & Prausnitz, M. R. (1998). Microfabricated Microneedles: A Novel Approach to Transdermal Drug Delivery. *Journal of Pharmaceutical Sciences, 87*(8), 922-925. https://doi.org/10.1021/js980042+

Hirsch, J. (2011). Aluminium sheet fabrication and processing. In *fundamentals of aluminium metallurgy* (pp. 719-746). Woodhead Publishing. https://doi.org/10.1533/9780857090256.3.719

Horita, Z., Furukawa, M., Nemoto, M., & Langdon, T. G. (1999). Grain refinement of aluminum using equal-channel angular pressing. *MRS Online Proceedings Library (OPL), 601*. https://doi.org/10.1557/PROC-601-311

Horita, Z., Furukawa, M., Nemoto, M., Barnes, A. J., & Langdon, T. G. (2000a). Superplastic forming at high strain rates after severe plastic deformation. *Acta Materialia, 48*(14), 3633-3640. https://doi.org/10.1016/S1359-6454(00)00182-8

Horita, Z., Fujinami, T., Nemoto, M., & Langdon, T. G. (2000b). Equal-channel angular pressing of commercial aluminum alloys: grain refinement, thermal stability and tensile properties. *Metallurgical and Materials Transactions A*, *31*(3), 691-701. https://doi.org/10.1007/s11661-000-0011-8

Horita, Z., Fujinami, T., Nemoto, M., & Langdon, T. G. (2001). Improvement of mechanical properties for Al alloys using equal-channel angular pressing. *Journal of Materials Processing Technology, 117*(3), 288-292. https://doi.org/10.1016/S0924-0136(01)00783-X

Huang, J. Y., Zhu, Y. T., Jiang, H., & Lowe, T. C. (2001). Microstructures and dislocation configurations in nanostructured Cu processed by repetitive corrugation and straightening. *Acta Materialia, 49*(9), 1497-1505. https://doi.org/10.1016/S1359-6454(01)00069-6

Huang, J. Y., Zhu, Y. T., Alexander, D. J., Liao, X., Lowe, T. C., & Asaro, R. J. (2004). Development of repetitive corrugation and straightening. *Materials Science and Engineering: A, 371*(1), 35-39. https://doi.org/10.1016/S0921-5093(03)00114-X

Iwahashi, Y., Horita, Z., Nemoto, M., Wang, J., & Langdon, T. G. (1996). Principle of equal-channel angular pressing for the processing of ultra-fine grained materials. *Scripta materialia, 35*(2). https://doi.org/10.1016/1359-6462(96)00107-8

Javidikia, M., & Hashemi, R. (2017). Analysis and Simulation of Parallel Tubular Channel Angular Pressing of Al 5083 Tube. *Transactions of the Indian Institute of Metals, 70*(10), 2547-2553. https://doi.org/10.1007/s12666-017-1117-7

Johnson, W., & Mellor, P. B. (1962). *Plasticity for mechanical engineers*. Van Nostrand.

Kaibyshev, R., Musin, F., Avtokratova, E., & Motohashi, Y. (2005). Deformation behavior of a modified 5083 aluminum alloy. *Materials Science and Engineering: A, 392*(1), 373-379. https://doi.org/10.1016/j.msea.2004.10.002

Kalidindi, S. R., Abusafieh, A., & El-Danaf, E. (1997). Accurate characterization of machine compliance for simple compression testing. *Experimental mechanics, 37*(2), 210-215. https://doi.org/10.1007/BF02317861

Kawasaki, M., Horita, Z., & Langdon, T. G. (2009). Microstructural evolution in high purity aluminum processed by ECAP. *Materials Science and Engineering: A*, *524*(1-2), 143-150. https://doi.org/10.1016/j.msea.2009.06.032

Kawasaki, M., Alhajeri, S. N., Xu, C., & Langdon, T. G. (2011). The development of hardness homogeneity in pure aluminum and aluminum alloy disks processed by high-pressure torsion. *Materials Science and Engineering: A, 529*, 345-351. https://doi:10.1016/j.msea.2011.09.039

Langdon, T. G. (2009). Seventy-five years of superplasticity: historic developments and new opportunities. *Journal of Materials Science, 44*(22), 5998-6010. https://doi.org/10.1007/s10853-009-3780-5

Langdon, T. G. (2010). Seventy-five years of superplastic research: an overall perspective for the superplasticity conferences. *Key Engineering Materials*, *433*, 3-8. https://doi.org/10.4028/www.scientific.net/KEM.433.3

Langdon, T. G. (2013). Twenty-five years of ultrafine-grained materials: Achieving exceptional properties through grain refinement. *Acta Materialia*, *61*(19), 7035-7059. https://doi.org/10.1016/j.actamat.2013.08.018

Lasalmonie, A., & Strudel, J. L. (1986). Influence of grain size on the mechanical behaviour of some high strength materials. *Journal of Materials Science*, *21*(6), 1837-1852. https://doi.org/10.1007/BF00547918

Lavernia, E. J., & Srivatsan, T. S. (2010). The rapid solidification processing of materials: science, principles, technology, advances, and applications. *Journal of Materials Science, 45*(2), 287-325. https://doi.org/10.1007/s10853-009-3995-5

Lee, J. C., Seok, H. K., Han, J. H., & Chung, Y. H. (2001). Controlling the textures of the metal strips via the continuous confined strip shearing (C2S2) process. *Materials Research Bulletin*, *36*(5-6), 997-1004. https://doi.org/10.1016/S0025-5408(01)00557-8

Lee, J. C., Seok, H. K., & Suh, J. Y. (2002). Microstructural evolutions of the Al strip prepared by cold rolling and continuous equal channel angular pressing. *Acta Materialia*, *50*(16), 4005-4019. https://doi.org/10.1016/S1359-6454(02)00200-8

Lejček, P. (2010). *Grain boundary segregation in metals* (Vol. 136). Springer. https://doi.org/10.1007/978-3-642-12505-8

Masuzawa, T. (2000). State of the Art of Micromachining. *CIRP Annals, 49*(2), 473-488. https://doi.org/10.1016/S0007-8506(07)63451-9

Meyers, M. A., Mishra, A., & Benson, D. J. (2006). Mechanical properties of nanocrystalline materials. *Progress in Materials Science, 51*(4), 427-556. https://doi.org/10.1016/j.pmatsci.2005.08.003

Nieh, T. G., & Wadsworth, J. (1991). Hall-petch relation in nanocrystalline solids. *Scripta Metallurgica et Materialia, 25*(4), 955-958. https://doi.org/10.1016/0956-716X(91)90256-Z

Oh-Ishi, K., Horita, Z., Nemoto, M., Furukawa, M., & Langdon, T. G. (1998). Optimizing the rotation conditions for grain refinement in equal-channel angular pressing. *Metallurgical Materials Transactions A, 29*(7), 2011-2013.

Oh, S. J., & Kang, S. B. (2003). Analysis of the billet deformation during equal channel angular pressing. *Materials Science and Engineering: A, 343*(1-2), 107-115. https://doi.org/10.1016/S0921-5093(02)00324-6

Olejnik, L., Rosochowski, A., & Richert, M. W. (2008, August). Incremental ECAP of plates. In Materials Science Forum (Vol. 584, pp. 108-113). Trans Tech Publications Ltd. https://doi.org/10.4028/www.scientific.net/MSF.584-586.108

Orlov, D., Beygelzimer, Y., Synkov, S., Varyukhin, V., Tsuji, N., & Horita, Z. (2009). Microstructure Evolution in Pure Al Processed with Twist Extrusion. *Materials Transactions, 50*(1), 96-100. https://doi.org/10.2320/matertrans.MD200802

Otto, T., Schubert, A., Boehm, J., & Gessner, T. (2000, August). Fabrication of micro-optical components by high-precision embossing. In Micromachining Technology for Micro-Optics (Vol. 4179, pp. 96-106). SPIE. https://doi.org/10.1117/12.395679

Park, K. T., Hwang, D. Y., Chang, S. Y., & Shin, D. H. (2002). Low-temperature superplastic behavior of a submicrometer-grained 5083 Al alloy fabricated by severe plastic deformation. *Metallurgical and Materials Transactions A, 33*(9), 2859-2867. https://doi.org/10.1007/s11661-002-0271-6

Park, K. T., Lee, H. J., Lee, C. S., Ahn, B. D., Cho, H. S., & Shin, D. H. (2004). Effect of ECAP Strain on Deformation Behavior at Low Temperature Superplastic Regime of Ultrafine Grained 5083 Al Alloy Fabricated by ECAP. *MATERIALS TRANSACTIONS, 45*(3), 958-963. https://doi.org/10.2320/matertrans.45.958

Park, K. T., Park, J. H., Lee, Y. S., & Nam, W. J. (2005). Microstructures developed by compressive deformation of coarse grained and ultrafine grained 5083 Al alloys at 77K and 298K. *Materials Science and Engineering: A, 408*(1), 102-109. https://doi.org/10.1016/j.msea.2005.07.040

Pérez-Bergquist, S. J., Gray, G. T., Cerreta, E. K., Trujillo, C. P., & Pérez-Bergquist, A. (2011). The dynamic and quasi-static mechanical response of three aluminum armor alloys: 5059, 5083 and 7039. *Materials Science and Engineering: A, 528*(29), 8733-8741. https://doi.org/10.1016/j.msea.2011.08.046

Pickens, J. R. (1981). Aluminium powder metallurgy technology for high-strength applications. *Journal of Materials Science*, *16*, 1437-1457. https://doi.org/10.1007/BF02396863

Polyakov, A. V., Gunderov, D., & Raab, G. I. (2011, February). Evolution of microstructure and mechanical properties of titanium Grade 4 with the Increase of the ECAP-Conform passes. In *Materials Science Forum* (Vol. 667, pp. 1165-1170). Trans Tech Publications Ltd. https://doi.org/10.4028/www.scientific.net/MSF.667-669.1165

Prangnell, P. B., Bowen, J. R., & Apps, P. J. (2004). Ultra-fine grain structures in aluminium alloys by severe deformation processing. *Materials Science and Engineering: A, 375*, 178-185. https://doi.org/10.1016/j.msea.2003.10.170

Presz, W., & Rosochowski, A. (2006, April). The influence of grain size on surface quality of microformed components. In *The 9th International Conference on Material Forming: ESAFORM* (pp. 587-90).

Qarni, M. J., Sivaswamy, G., Rosochowski, A., & Boczkal, S. (2017). Effect of incremental equal channel angular pressing (I-ECAP) on the microstructural characteristics and mechanical behaviour of commercially pure titanium. *Materials & Design, 122*, 385-402. https://doi.org/10.1016/j.matdes.2017.03.015

Qiao, X. G., Gao, N., Moktadir, Z., Kraft, M., & Starink, M. J. (2010). Fabrication of MEMS components using ultrafine-grained aluminium alloys. *Journal of Micromechanics and Microengineering, 20*(4), 045029. https://doi.org/10.1088/0960-1317/20/4/045029

Raab, G. J., Valiev, R. Z., Lowe, T. C., & Zhu, Y. T. (2004). Continuous processing of ultrafine grained Al by ECAP–Conform. *Materials Science and Engineering: A, 382*(1), 30-34. https://doi.org/10.1016/j.msea.2004.04.021

Raja, C. P., & Ramesh, T. (2021). Influence of size effects and its key issues during microforming and its associated processes–A review. *Engineering Science and Technology, an International Journal*, *24*(2), 556-570. https://doi.org/10.1016/j.jestch.2020.08.007

Rastegaev, M. V. (1940). New method of uniform upsetting of specimens for determining the true deformation resistance and the coefficient of external friction. *Zavod Lab*, *6*(3), 354.

Razali, A. R., & Qin, Y. (2013). A Review on Micro-manufacturing, Micro-forming and their Key Issues. *Procedia Engineering, 53*, 665-672. https://doi.org/10.1016/j.proeng.2013.02.086

Richert, M., & Korbel, A. (1995). The effect of strain localization on mechanical properties of A199, 992 in the range of large deformations. *Journal of Materials Processing Technology*, *53*(1-2), 331-340. https://doi.org/10.1016/0924-0136(95)01990-V

Richert, M., Richert, J., Zasadziński, J., Hawryłkiewicz, S., & Długopolski, J. (2003). Effect of large deformations on the microstructure of aluminium alloys. *Materials chemistry and physics*, *81*(2-3), 528-530. https://doi.org/10.1016/S0254-0584(03)00066-X

Rosochowska, M., Rosochowski, A., & Olejnik, L. (2010). FE simulation of micro-extrusion of a conical pin. *International Journal of Material Forming, 3*(1), 423-426. https://doi.org/10.1007/s12289-010-0797-x

Rosochowski, A. (2004). Processing metals by severe plastic deformation. *Solid State Phenomena*, *101*, 13-22. https://doi.org/10.4028/www.scientific.net/SSP.101-102.13

Rosochowski, A., & Olejnik, L. (2007a). Finite element simulation of severe plastic deformation processes. *Proceedings of the Institution of Mechanical Engineers, Part L: Journal of Materials: Design and Applications*, *221*(4), 187-196. https://doi.org/10.1243/14644207JMDA166

Rosochowski, A., Presz, W., Olejnik, L., & Richert, M. (2007b). Micro-extrusion of ultra-fine grained aluminium. *The International Journal of Advanced Manufacturing Technology, 33*(1-2), 137-146. https://doi.org/10.1007/s00170-007-0955-6

Rosochowski, A., Olejnik, L., & Richert, M. W. (2008, August). Double-billet incremental ECAP. In *Materials Science Forum* (Vol. 584, pp. 139-144). Trans Tech Publications Ltd. https://doi.org/10.4028/www.scientific.net/MSF.584-586.139

Rosochowski, A., & Olejnik, L. (2011, March). Incremental equal channel angular pressing for grain refinement. In *Materials Science Forum* (Vol. 674, pp. 19-28). Trans Tech Publications Ltd. https://doi.org/10.4028/www.scientific.net/MSF.674.19

Roy, I., Chauhan, M., Mohamed, F. A., & Lavernia, E. J. (2006). Thermal stability in bulk cryomilled ultrafine-grained 5083 Al alloy. *Metallurgical and Materials Transactions A, 37*(3), 721-730. https://doi.org/10.1007/s11661-006-0044-8

Saito, Y., Tsuji, N., Utsunomiya, H., Sakai, T., & Hong, R. G. (1998). Ultra-Fine Grained Bulk Aluminum Produced by Accumulative Roll-Bonding (ARB) Process. *Scripta Mater., 39*(9), 1221-1227. https://doi.org/10.1016/S1359-6462(98)00302-9

Salamati, M. R., & Rosochowski, A. (2014). Using FEA in assessing backward extrusion of multiple micro-pins. *Key Engineering Materials*, *611*, 589-596. https://doi.org/10.4028/www.scientific.net/KEM.611-612.589

Salamati, M. R., Qarni, M. J., Tamimi, S., & Rosochowski, A. (2016, October). Effect of channel angle on the material flow, hardness distribution and process forces during incremental ECAP of Al-1050 billets. In *AIP Conference Proceedings* (Vol. 1769, No. 1, p. 090004). AIP Publishing LLC. https://doi.org/10.1063/1.4963494

Salamati, M. R. (2018). *Metal microneedles for transdermal drug delivery* [Doctoral dissertation, University of Strathclyde]. Strathprints Institutional Repository. https://doi.org/10.48730/jhap-bf43

Saotome, Y., & Iwazaki, H. (2001). Superplastic backward microextrusion of microparts for micro-electro-mechanical systems. *Journal of Materials Processing Technology, 119*(1-3), 307-311. https://doi.org/10.1016/S0924-0136(01)00957-8

Shanmugasundaram, T., Heilmaier, M., Murty, B. S., & Sarma, V. S. (2010). On the Hall–Petch relationship in a nanostructured Al–Cu alloy. *Materials Science and Engineering: A, 527*(29), 7821-7825. https://doi.org/10.1016/j.msea.2010.08.070

Sharma, S. K., Kodli, B. K., & Saxena, K. K. (2022). Micro forming and its applications: an overview. *Key engineering materials*, *924*, 73-91. https://doi.org/10.4028/p-3u80qc

Sherby, O. D., & Wadsworth, J. (1985). Superplasticity and superplastic forming processes. *Materials science and technology*, *1*(11), 925-936. https://doi.org/10.1179/mst.1985.1.11.925

Stolyarov, V. V., Zhu, Y. T., Alexandrov, I. V., Lowe, T. C., & Valiev, R. Z. (2001). Influence of ECAP routes on the microstructure and properties of pure Ti. *Materials Science and Engineering: A, 299*(1-2), 59-67. https://doi.org/10.1016/S0921-5093(00)01411-8

Suryanarayana, C. (2001). Mechanical alloying and milling. *Progress in materials science*, *46*(1-2), 1-184. https://doi.org/10.1016/S0079-6425(99)00010-9

Tang, F., Hagiwara, M., & Schoenung, J. M. (2005). Formation of coarse-grained inter-particle regions during hot isostatic pressing of nanocrystalline powder. *Scripta materialia, 53*(6), 619-624. https://doi.org/10.1016/j.scriptamat.2005.05.034

Tokarski, T., Wzorek, Ł., & Dybiec, H. (2012). Microstructure and plasticity of hot deformed 5083 aluminum alloy produced by rapid solidification and hot extrusion. *Archives of Metallurgy and Materials*, *57*(4), 1253-1259. https://doi:10.2478/v10172-012-0140-2

Upadhyaya, G. S. (1997). *Powder metallurgy technology*. Cambridge Int Science Publishing.

Uranga, P., & María Rodríguez-Ibabe, J. (2020). Thermomechanical processing of steels. *Metals*, *10*(5), 641. https://doi.org/10.3390/met10050641

Valiev, R. Z., Islamgaliev, R. K., & Alexandrov, I. V. (2000). Bulk nanostructured materials from severe plastic deformation. *Progress in materials science*, *45*(2), 103-189. https://doi.org/10.1016/s0079-6425(99)00007-9

Valiev, R. Z., & Langdon, T. G. (2006). Principles of equal-channel angular pressing as a processing tool for grain refinement. *Progress in materials science*, *51*(7), 881-981. https://doi.org/10.1016/j.pmatsci.2006.02.003

Valiev, R. Z., Straumal, B., & Langdon, T. G. (2022). Using severe plastic deformation to produce nanostructured materials with superior properties. *Annual Review of Materials Research*, *52*, 357-382. https://doi.org/10.1146/annurev-matsci-081720-123248

Vollertsen, F., Schulze Niehoff, H., & Hu, Z. (2006). State of the art in micro forming. *International Journal of Machine Tools and Manufacture, 46*(11), 1172-1179. https://doi.org/10.1016/j.ijmachtools.2006.01.033

Wei, Q., Jia, D., Ramesh, K. T., & Ma, E. (2002). Evolution and microstructure of shear bands in nanostructured Fe. *Applied physics letters, 81*(7), 1240-1242. https://doi.org/10.1063/1.1501158

Witkin, D., Han, B. Q., & Lavernia, E. J. (2005). Mechanical behavior of ultrafine-grained cryomilled Al 5083 at elevated temperature. *Journal of Materials Engineering and Performance, 14*(4), 519-527. https://doi.org/10.1361/105994905x56232

Worgull, M., & Heckele, M. (2004). New aspects of simulation in hot embossing. *Microsystem Technologies, 10*(5), 432-437. https://doi.org/10.1007/s00542-004-0418-z

Wu, B. B., Wang, Z. Q., Wang, X. L., Zhao, J. X., Shang, C. J., & Misra, R. D. K. (2019). Relationship between high angle grain boundaries and hardness after γ→ α transformation. *Materials Science and Technology*, *35*(15), 1803-1814. https://doi.org/10.1080/02670836.2019.1647936

Xu, J., Shi, L., Wang, C., Shan, D., & Guo, B. (2015). Micro hot embossing of micro-array channels in ultrafine-grained pure aluminum using a silicon die. *Journal of Materials Processing Technology, 225*, 375-384. https://doi.org/10.1016/j.jmatprotec.2015.06.025

Xu, J., Wang, X., Wang, C., Yuan, L., Chen, W., Bao, J., Su, Q., Xu, Z., Wang, C., Wang, Z., Shan, D., & Guo, B. (2021). A review on micro/nanoforming to fabricate 3D metallic structures. *Advanced Materials*, *33*(6), 2000893. https://doi.org/10.1002/adma.202000893

Yadav, T. P., Mukhopadhyay, N. K., Tiwari, R. S., & Srivastava, O. N. (2005). Studies on the formation and stability of nano-crystalline Al50Cu28Fe22 alloy synthesized through high-energy ball milling. *Materials Science and Engineering: A*, *393*(1-2), 366-373. https://doi.org/10.1016/j.msea.2004.11.002

Zhou, M., & Clode, M. P. (1998). Constitutive equations for modelling flow softening due to dynamic recovery and heat generation during plastic deformation. *Mechanics of Materials, 27*(2), 63-76. https://doi.org/10.1016/S0167-6636(97)00035-5

Zhu, C., Hao, M., Ding, C., Xu, J., Yu, H., Gao, Y., ... & Shan, D. (2025). Impact micro-forming technology: Current status, challenges and prospects. *Journal of Materials Research and Technology*. https://doi.org/10.1016/j.jmrt.2025.04.149